THÈSE présentée par :

Sujit Kumar Sahu

soutenue le: **06/02/2023**

pour obtenir le grade de: **Docteur de l'université de Strasbourg**

Discipline/ Spécialité: **Robotique**

Inductive sensors and shape reconstruction for intraluminal flexible and soft robots

THÈSE dirigée par:

Pierre Renaud	Professeur des Universités, Université de Strasbourg
Arianna Menciassi	Professeur des Universités, Scoula Superiore Sant'Anna
Benoit Rosa	Université de Strasbourg
Izadyar Tamadon	Scoula Superiore Sant'Anna
Selene Tognarelli	Scoula Superiore Sant'Anna

RAPPORTEURS:

Alicia Casals	Professeur des Universités, UPC Barcelona
Emmanuel Vander Poorten	Professeur des Universités, KU Leuven

AUTRES MEMBRES DU JURY:

Philippe Poignet	Professeur des Universités, University of Montpellier
Piero Castoldi	Professeur des Universités, Scoula Superiore Sant'Anna

Inductive sensors and shape reconstruction for intraluminal flexible and soft robots

By

Sujit Kumar Sahu

A dissertation submitted in partial fulfillment of the requirements for the degree of Doctor of Philosophy.

Supervisors

Prof. Dr. Arianna Menciassi

Prof. Dr. Pierre Renaud

Tutors

Dr. Selene Tognarelli

Dr. Benoit Rosa

Dr. Izadyar Tamadon

THE BIOROBOTICS INSTITUTE, SCUOLA SUPERIORE SANT'ANNA,

PISA, ITALY

ICUBE, UNIVERSITY OF STRASBOURG, STRASBOURG, FRANCE

November 2022

ACKNOWLEDGEMENT

SHORT SUMMARIES

Title: Capteurs inductifs et reconstruction de forme pour les robots medicaux souples et flexibles

Les robots souples et flexibles transforment les interventions médicales, grâce à leur flexibilité, leur miniaturisation et leurs capacités de mouvement multidirectionnel. Cependant, les méthodes de reconstruction de forme existantes n'ont pas suffisamment pris en compte les défis posés par les robots souples et flexibles dans les environnements non structurés et dynamiques. Dans cette thèse, un capteur extensible basé sur le principe inductif électrique est proposé comme solution à ce problème. Le capteur peut détecter de grandes déformations avec une grande précision et une grande précision et est intégré dans un robot souple et flexible pour un contrôle en boucle fermée. La thèse se concentre sur la reconstruction de la forme du robot dans des scénarios de chirurgie mini-invasive dans les espaces de travail 2D et 3D. Enfin, la thèse conclut en présentant le potentiel du capteur inductif pour la reconstruction de la forme de robots souples et flexibles et les travaux futurs pour surmonter les limitations.

Mots clés: Capteur de forme flexible, capteur inductif, détection en mode mini-invasif Chirurgie, reconstruction de forme

Title: Inductive sensors and shape reconstruction for intraluminal flexible and soft robots

Soft and flexible robots are transforming medical interventions, thanks to their flexibility, miniaturization, and multidirectional movement abilities. However, existing shape reconstruction methods have not adequately addressed the challenges posed by these robots in unstructured and dynamic environments. In this thesis, a stretchable sensor based on the electrical inductive principle is proposed as a solution to this problem. The thesis presents a simple voltage measurement method for strain estimation, which optimizes the measuring equipment and simplifies the measurement conditions. The sensor's feasibility and accuracy are demonstrated in an experimental

investigation that shows the sensor can detect large deformations with high precision and accuracy. The sensor is then integrated into a soft and flexible robot for closed-loop control, and the thesis focuses on reconstructing the robot's shape in minimally invasive surgery scenarios in both 2D and 3D workspaces. Finally, the thesis concludes with an overview of the inductive sensor's potential for shape reconstruction of soft and flexible robots and future work to address the limitations.

Keywords: Flexible shape sensor, Inductive sensor, Sensing in Minimally Invasive Surgery, Shape reconstruction

Abstract

Soft and flexible robots are transforming medical interventions, thanks to their flexibility, miniaturization, and multidirectional movement abilities. In recent days, to increase the performance of the controlling action during their movement in the unstructured and dynamic environment, shape reconstruction methods based on exteroceptive and proprioceptive sensors have been developed enormously. However, the reconstruction methods presented in the literature still lack to address the issue of soft and flexible robots. In this thesis, a method to reconstruct the shape of soft and flexible robots using a stretchable sensor is presented. This thesis is divided into two parts. In the first part, a stretchable sensor is selected by investigating different properties such as hysteresis, stretchability, and feasibility of integration. This investigation is started with resistive-based stretchable sensors which shows that dealing with high hysteresis and non-linearities needs a complicated and advanced fabrication process. Given the effort needed to reduce the hysteresis and non-linearities in the direction of resistive sensor design, a stretchable sensor based on the electrical inductive principle is considered. During the investigation of inductive sensors, three contributions are developed. First, a simple voltage measurement across a conventional spring acting as a variable inductor is presented for strain estimation. This simplifies the measuring equipment and also allows for the optimization of the measurement conditions. Second, an experimental investigation shows that a single calibration curve generated outside of the robot is enough to estimate the linear or bending strain of the robot, given the system type. Third, a full characterization is conducted that shows the sensor is capable of detecting large deformation while showing high precision and accuracy. To show the feasibility of the sensor integration process, the same sensor is integrated into a soft and a flexible robot. The closed-loop control is performed which demonstrates that the robots can be controlled accurately, thanks to the presented proprioceptive sensor. The second part of the thesis focuses on the shape reconstruction of soft and flexible robots employed in minimally invasive surgery using the inductive sensor. In this case, the length information from the inductive sensor is converted to the arc

parameters of robots using constant curvature modeling. These arc parameters are further used to reconstruct the shape. The shape reconstruction process is performed in 2D and 3D workspace, and the corresponding accuracy is estimated by comparing with ground truth values. Ultimately, the thesis is concluded by providing remarks on the use of the inductive sensor for the shape reconstruction of soft and flexible robots while highlighting the limitations and perspective of future work.

Keywords: Flexible shape sensor, Inductive sensor, Sensing in Minimally Invasive Surgery, Shape reconstruction.

TABLE OF CONTENTS

List of Figures

v

List of Tables

Chapter 1

Résumé en Français

1.1   Introduction

Les interventions chirurgicales assistées par la robotique se développent, en visant à améliorer la qualité des gestes réalisés avec des approches chirurgicales traditionnelles. L'idée de la chirurgie minimalement invasive est ainsi de réduire les traumatismes, d'améliorer le temps de récupération et d'accéder à des régions d'intérêt éloignées, difficiles à atteindre avec la chirurgie ouverte. Comme les trajets suivis par les outils chirurgicaux sont tortueux et complexes, la flexibilité des instruments paraît indispensable du point de vue de la sécurité pour permettre des déploiements dans des cavités profondes et difficiles à atteindre. Pour obtenir ces propriétés, on considère aujourd'hui des systèmes robotiques souples et flexibles. L'interaction avec les tissus peut alors modifier la forme et la position de ces robots. Estimer leur forme est alors une exigence pour les contrôler et évaluer leurs interactions avec le corps du patient.

Des méthodes de reconstruction de forme basées sur des capteurs extéroceptifs et proprioceptifs ont été proposées dans la littérature. Dans notre contexte, trois critères sont particulièrement importants. En premier lieu, il faut pouvoir gérer les déformations importantes des robots flexibles considérés. En outre, la méthode doit toujours viser à réduire l'utilisation de rayons ionisants, d'agents de contraste ou l'injection de produits chimiques. La précision est également un facteur important qui doit être pris en considération, y compris dans les conditions d'un bloc opératoire.

L'état de l'art des méthodes de reconstruction de forme a été exploré par une recherche approfondie de la littérature, en mettant en perspective les solutions compte

1

tenu des exigences susmentionnées. Actuellement, les capteurs souples, résistifs et inductifs, semblent particulièrement intéressants. Leur grande souplesse permet leur utilisation pour reconstruire la forme de robots très flexibles. S'agissant de mesures proprioceptives, elles sont disponibles tout au long de l'utilisation, sans risque de perte de signal. Cependant, les erreurs de reconstruction de forme restent aujourd'hui importantes. Aussi, cette thèse vise à élaborer une solution de mesure adéquate en termes de précision de reconstruction de forme, et la caractériser.

1.2 Développement de capteurs résistifs

Les capteurs résistifs ont d'abord été étudiés, en s'attachant à identifier un processus de fabrication permettant de limiter les non-linéarités de ces capteurs qui sont communément observées dans la littérature. Les capteurs résistifs sont généralement fabriqués en utilisant des matériaux élastomères comme substrat de base. Aussi l'étude initiale s'est concentrée sur la recherche d'un matériau de base approprié présentant le moins d'hystérésis et de non-linéarités possible. Trois différents types de silicone (Ecoflex-0010, Ecoflex-0030, et Ecoflex-0050) ont été considérés. Des échantillons de ces silicones ont été préparés. Des tests mécaniques ont été réalisés pour calculer l'hystérésis, le module de Young et les non-linéarités de tous ces matériaux. Ecoflex-0030 a été sélectionné car il présentait les meilleures propriétés.

Ensuite, plusieurs géométries et prototypes de capteurs ont été conçus et élaborés : capteur résistif cylindrique à l'aide d'une pâte conductrice utilisant de la poudre de graphite et un tube de silicone ; capteur de même géométrie mais fabriqué par mélange direct de poudre de graphite et Ecoflex-030 et finalement capteur exploitant un caoutchouc conducteur commercial (adafruit, USA). Malgré ce travail expérimental ayant permis d'observer une progression du comportement des prototypes, aucune solution n'est apparue satisfaisante et prometteuse pour maitriser l'hystérésis et les non-linéarités dans la mesure. Par conséquent, étant donné l'effort nécessaire pour aller plus loin dans la conception de capteurs résistifs, une solution alternative a été considérée.

1.3 Développement d'un capteur inductif

1.3.1 Dévéloppement initial et optimisation des conditions de mesure

Les techniques de mesure inductive sont apparues d'intérêt lors de l'analyse de l'état de l'art. Les capteurs inductifs peuvent présenter une hystérésis très faible, une précision millimétrique, et une extensibilité jusqu'à 100 %. Aussi, la décision d'utiliser le capteur inductif dans la méthode de reconstruction de forme a été prise. En explorant la littérature, il a été observé qu'une instrumentation spécifique est généralement nécessaire. Cela représente une contrainte d'intégration pour un dispositif médical, et une contrainte de coût potentiellement. Aussi, une méthode est proposée pour mesurer la déformation en utilisant une simple mesure de tension au lieu d'effectuer une mesure directe de l'inductance. De plus, la méthode est proposée avec une démarche d'adaptation des conditions de mesure afin d'optimiser les performances du capteur en termes de gain et sensibilité. Cette capacité a été évaluée et confirmée expérimentalement.

1.3.2 Impact du mode de deformation

Par un modèle analytique simple, nous avons pu établir la dépendance du gain et de la sensibilité du capteur mis en place en fonction de la variation de longueur du ressort. Cette variation peut être due à un allongement linéaire pur avec des boucles de bobines restant parallèles, ou à une flexion, ou à une combinaison de ces modes de déformation lorsque le capteur est placé dans un manipulateur flexible. Étalonner le capteur pour chaque type de déformation serait consommateur de temps, et une dépendance au mode de déformation source d'imprécision. Une étude expérimentale a donc été menée pour vérifier si l'étalonnage peut être effectué une seule fois, pour accomplir les mesures de la longueur curviligne du ressort. Il apparaît qu'une même relation entre gain et déformation peut être utilisée pour toute une gamme courbure correspondant aux situations envisagées durant des gestes médicaux avec un robot flexible. Il est donc possible pour un ressort donné de conduire un étalonnage unique avant intégration et exploitation pour l'estimation de

déformation.

1.3.3 Caractérisation du capteur

Un processus de caractérisation détaillé a ensuite été mené pour estimer les performances atteignables avec ce type de capteur. Dans un premier temps, le capteur a été soumis à une charge répétitive. L'hystérésis moyenne est de 0,1% avec un écart type de 0,023%. Pour l'évaluation de la précision, un allongement connu a été appliqué au capteur en utilisant une platine de déplacement linéaire. L'écart maximal observé pour un ensemble de neuf longueurs différentes est égal à 0,14%. La précision moyenne est de 0,73 mm, ce qui représente 0,9% de la déformation appliquée, un résultat satisfaisant pour l'exploitation envisagée.

1.3.4 Exploitation initiale – preuves de concept

Deux preuves de concept ont été développées pour vérifier l'intérêt et l'apport de la solution de mesure inductive mise en place.

Comme première preuve de concept, le capteur a été intégré à un prototype d'actionneur souple qui peut s'étendre jusqu'à une déformation de 80 %. Il est observé expérimentalement une erreur de contrôle de la longueur de 1,16 ± 0,75 mm lorsque la longueur du capteur a été comparée à la vérité terrain.

Comme deuxième preuve de concept, le capteur a été intégré dans un prototype de manipulateur flexible actionné par câbles. Deux câbles ont été insérés à l'intérieur des ressorts servant pour la mesure, qui ont été connectés au moteur, en utilisant une poulie pour l'actionnement. Un contrôleur PID a été conçu pour contrôler le rayon de courbure du manipulateur flexible. Un ensemble de valeurs de rayons a été utilisé comme référence pour le contrôleur. À titre de comparaison, un contrôle en boucle ouverte a été effectué en utilisant la longueur du câble. L'erreur moyenne en régime permanent dans le cas de la commande en boucle ouverte était de 5 mm, soit 3,6 % de la longueur du manipulateur. En revanche, pour la commande en boucle fermée, cette erreur était de 2 mm, soit 1,4 % de la longueur du manipulateur. Il est donc possible de réduire l'erreur de contrôle de 2,5 via l'emploi de la solution proposée.

1.3.5   Reconstruction de forme

L'utilisation du capteur dans deux preuves de concept a montré que le capteur est utile dans la commande de systèmes robotiques dont les caractéristiques sont celles de robots flexibles. La capacité d'évaluer la forme de dispositifs souples et flexibles a été étudiée ensuite en deux étapes, avec une complexité croissante. Tout d'abord, le manipulateur précédent a été utilisé pour des mouvements 2D et l'estimation de la forme planaire correspondante a été vérifiée. Ensuite, le cas général de la forme 3D a été étudié en utilisant les informations de plusieurs capteurs.

Pour le cas 2D, la forme du manipulateur a été reconstruite en utilisant l'angle et le rayon de courbure calculés à partir de la mesure. Pour déterminer l'erreur dans le processus d'estimation de la forme, les formes reconstruites ont été comparées à une estimation de forme basée sur la vision. L'erreur de reconstruction la plus élevée a été estimée à 6,67 mm, tandis que l'erreur minimale était de 3,35 mm. La reconstruction moyenne de la forme a été calculée à 4,8 mm, ce qui représente 3,43 % de la longueur totale du manipulateur.

Pour le cas 3D, la modification de forme du manipulateur dans un espace de travail tridimensionnel a été réalisée en intégrant quatre capteurs au manipulateur flexible dans une configuration quadrangulaire. Différents paramètres d'arc du manipulateur, tels que la courbure, la longueur de l'arc, l'angle contenant l'arc ont été estimés en supposant un modèle à courbure constante issue de la littérature. Le robot a été actionné en différents points et les formes ont été reconstruites. Pour estimer la précision, les coordonnées de l'extrémité reconstruite du manipulateur ont été comparées à l'extrémité suivie par un capteur électromagnétique placé à l'extrémité. L'erreur moyenne RMS pour cinq formes a été estimée à 15,5 mm. Si la valeur excède le besoin médical à ce stade, elle tend à montrer la faisabilité de l'utilisation, et l'intérêt d'un travail complémentaire notamment sur la modélisation exploitée pour l'estimation de forme.

1.3.6   Conclusion et travaux futurs

Dans cette thèse, un capteur pour reconstruire la forme d'un manipulateur flexible a été présenté. Sur la base de critères concernant la gamme de déformation mesurable, de sécurité et de précision, l'étude a commencé par des capteurs de déformation résistifs. En raison de valeurs d'hystérésis restant élevées et de nonlinéarités, les capteurs résistifs fabriqués ne peuvent pas remplir tous les critères. Pour résoudre ces problèmes, une approche alternative de mesure inductive exploitant des ressorts hélicoïdaux conventionnels a été considérée. La mesure de déformation est alors basée sur un simple principe d'inductance variable. L'étude a montré qu'il présente une hystérésis inférieure à 0,1% pour une déformation de 80%, une précision de l'ordre de 0,14% et une exactitude de 0,9%. Après le processus de caractérisation, le capteur a été implémenté avec succès dans un PAM et un manipulateur flexible pour construire un retour de position et de courbure pour la commande. Comme il a produit une faible hystérésis ainsi qu'une précision élevée, le capteur a finalement été utilisé pour la reconstruction de la forme. La forme du manipulateur flexible a été reconstruite dans des espaces de travail 2D et 3D. Une erreur moyenne de 4,8 mm a été observée pour le cas 2D tandis qu'une erreur RMS de 15,5 mm a été estimée pour le suivi de la pointe en 3D.

Dans l'ensemble, le capteur inductif développé a été capable de reconstruire la forme du manipulateur dans des espaces de travail 2D et 3D. Deux perspectives principales sont identifiées. Premièrement, poursuivre les efforts de caractérisation 3D et affiner le choix du modèle pour la reconstruction 3D. Deuxièmement, aller vers la commande d'un manipulateur flexible pour atteindre une cible spécifique en se rapprochant des conditions d'utilisation cliniques, par exemple dans un modèle de fantôme de colon pour reproduire le déploiement du robot, pour démontrer l'apport de la reconstruction de forme sur base de mesure inductive proposée.

Chapter 2

Motivation

2.1 General Overview

Over the past decade, Minimally Invasive Surgery (MIS) [1] has gained much attention to improve open surgical approaches. It has revolutionized the ways clinicians perform complex surgeries and diagnoses. Since open surgery is quite often associated with excruciating pain, surgical site infection, high hemorrhage, and protracted postoperative hospital stay, MIS emerged as a substitute. Small incisions are made in the case of MIS to achieve intra-body access rather than the single big incision used in open surgery; this results in less blood loss and shorter postoperative hospital stays for patients. At the outset, the era of MIS started with the development of rod-lens endoscopes back in the 1960s. This so-called laparoscopic surgery was then steadily preferred by patients and surgeons over open surgery. The laparoscopic method encounters ergonomic difficulties such as the counter-intuitive mirroring of tool movement produced by the fulcrum effect and reduced dexterity brought on by a lack of wrist mobility when using traditional rigid instruments. Surgical robotic systems have been introduced in MIS to overcome the limitations of traditional laparoscopic surgeries by exploiting the synergistic integration of robot precision and control. Da Vinci master-slave surgical system is an example of this kind that is widely accepted. The precise motion control is accomplished by motion scaling and tremor removal. The issue related to wrist articulation is solved by adding flexibility at the slave level. Despite many advantages, the rigid shaft of the surgical instrument is a major drawback of the platform which limits port placement and workable area. Additionally, as the paths followed during

1

MIS are tortuous and complex, the flexibility of instruments is indispensable from a practical point of view. Since then, MIS is under constant evolution to make flexible systems to enhance ergonomics, precision, and dexterity in MIS. The road map of this evolution is shown in Figure 2.1.
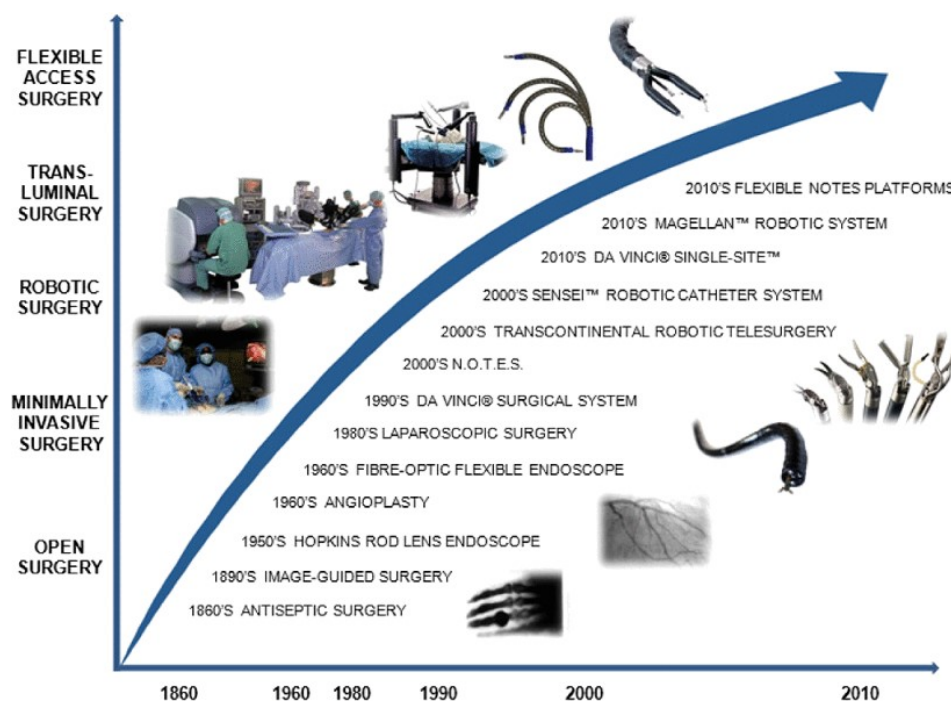
Figure 2.1: The evolution of MIS (adapted from [2])

Researchers are actively considering soft and flexible continuum robotic systems using compliant structures, instead of rigid links. These soft and flexible robots are gaining popularity in recent years due to their abilities to navigate complex anatomy pathways while maintaining adequate dexterity and precision. The body of soft robots is made using silicone or other soft materials while the flexible robots are fabricated using a flexible backbone with some rigid parts. The fluidic actuation robot fabricated in [3] is an example of a soft robot while a tendon-driven robot fabricated in [4] is a flexible robot. Different technologies have been considered to build these robotics systems, such as cable-driven robots [5, 6, 4, 7], fluid-operated robots [8, 9, 10, 3], and shape memory alloy operated robots [11, 12, 13]. Some examples of these robotic systems are shown in Figure 2.2. The review of their control and autonomous capabilities in MIS is presented in [14], [15], respectively. These robots can take any shape in space by performing bending, extension, contraction, and torsion of their structural components. These features help

them to reach the target in a dexterous way when in confined environments, by following a complicated path through the body lumen. Their flexibility and adaptability enhance the capabilities of surgeons to carry out different surgical or diagnostic procedures.
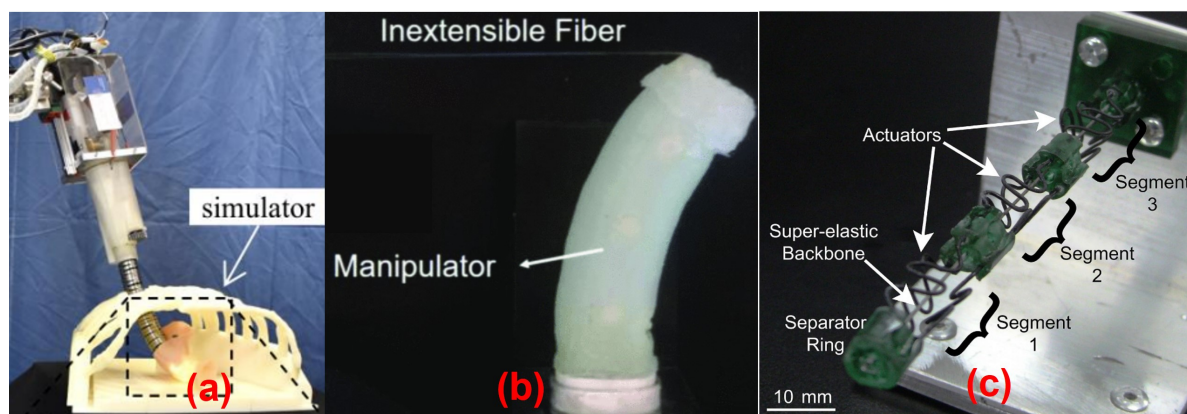
Figure 2.2: (a) Motor actuated robot (adapted from [4]); (b) Fluidic actuated robot (adapted from [9]); (c) SMA actuated robot (adapted from [11])

Although soft and flexible robots provide substantial advantages while improving their actuation strategies significantly in recent days, they have certain limitations too. Though they can adapt to numerous shapes with various curvatures, difficulties are encountered for active shape control due to their soft and flexible body [16]. The interaction with tissue may change the shape and position which should be detected in real-time to avoid injuries. Moreover, the presence of external forces also affects the shape of the robot, thereby making it difficult in controlling the backbone information. Even though the soft and flexible nature helps to maintain low interaction force, there is a still chance of tissue damage and patient discomfort. For instance, the endoscopes used in the case of gastroenterological interventions are known to cause tissue damage and discomfort for the patient [17]. Thus, the pose and shape information is needed in real-time not only to reduce the damage to tissue but also to tackle the external forces. It will also help to perform accurate maneuvering by providing feedback to the controller.

Modeling approaches for the shape estimation of continuum robots based on their kinematics have evolved tremendously [18, 19, 20, 21, 22, 23]. The accuracy of shape estimation depends on the validity of kinematic assumptions such as piecewise constant curvature [24]. However, they may become invalid when the robots are affected by

external loads. More comprehensive approaches have been proposed based on Cosserat Rod Theory combined with static model [21, 25, 26], and elliptical integral considering a known payload [19] to achieve more accurate shape estimation of the robot. Another approach, such as the model-based Rayleigh-Ritz formulation [18] is also developed to accurately estimate the shape of medical instruments. Regardless of the improvement of kinematic model-based shape sensing to increase their robustness, it is very challenging to implement in real-time applications under unknown payloads, as it modifies the assumed deformation mode.

On the other hand, exteroceptive and proprioceptive sensors-based shape reconstruction methods can allow for measuring the real-time shape of the robots in free space as well as in an unknown environment. The exteroceptive sensor-based methods typically use imaging techniques, while the proprioceptive sensor-based methods use embedded sensors for shape estimation. Both techniques seem relevant for soft and flexible robots used in MIS.

This thesis focuses on the development and analysis of a suitable shape reconstruction method for soft and flexible robots. Our approach starts with specifying the list of requirements that a reconstruction method needs to fulfill. Based on the requirements, different existing shape reconstruction methods are studied comprehensively. Eventually, a method is selected that satisfies all the required criteria and is used to reconstruct the shape of soft and flexible robots.

2.2 Requirement criteria to be fulfilled by a shape reconstruction method

Highly flexible robotic systems have been developed to deal with the complex and tortuous path inside the anatomy. For instance, the manipulator developed by Murphy et al. [27] has the ability to bend up to a large bending angle (197^0) with a radius of 5.9 mm in left and right direction (Figure 2.3 (Left)). In some cases, the robots are capable of extending and bending their segments simultaneously. For example, the robot developed by Nguyen et al. [28] consists of a telescoping backbone with tendon-driven actuation (Figure 2.3

(Right)). The telescoping backbone controls the length of the segments of the robot in addition to the bending via actuation of the tendons. Thus, these robotic systems need a shape reconstruction method that can handle the large deformation produced during their operation.
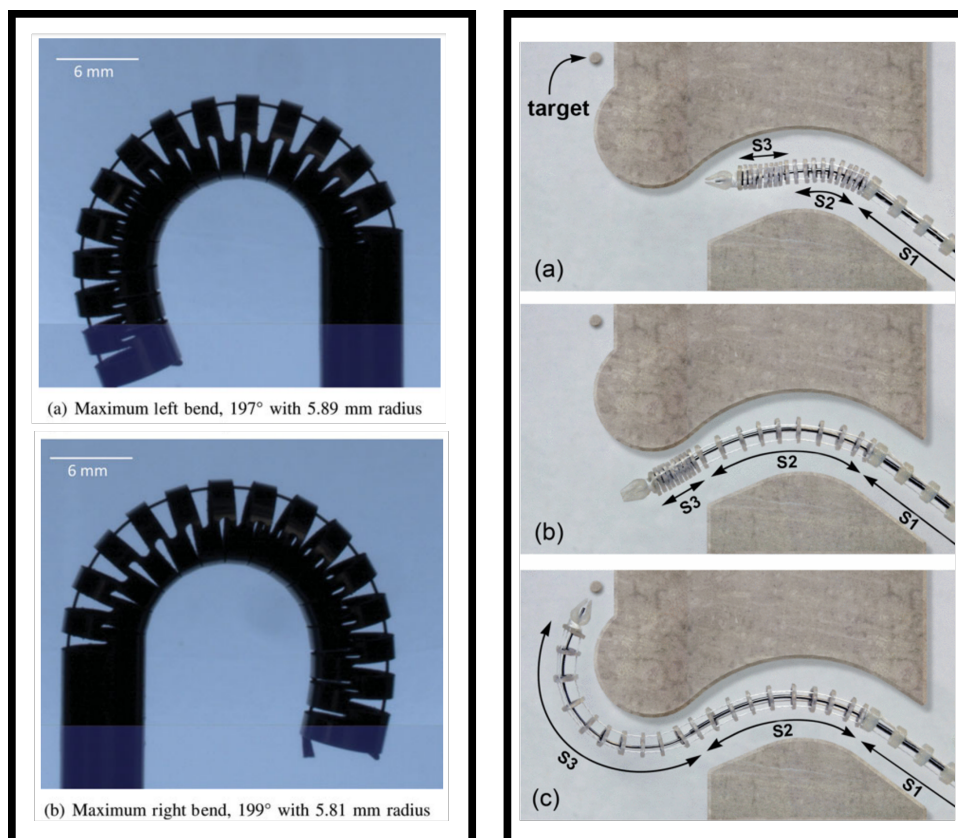
Figure 2.3: A robot performing large bending in both directions (left) [27]; A robot actuating itself to reach the target by extending and bending the segments (Right) [28]

As the safety of patients is a matter of concern in MIS, thus the shape reconstruction method should always aim to reconstruct the shape while reducing the use of ionizing dosage, contrast agent, and injection of chemicals. From the instances given in [29, 30], it can be observed that the ultrasound image of the robotic needle is hardly visible due to the low signal-to-noise ratio (Figure 2.4). It should also be made sure that the selected reconstruction method should be robust to in-vivo conditions whenever imaging is introduced.

Accuracy is also an important factor that needs to be taken into consideration while selecting the shape reconstruction method. Since different procedures in MIS such as aortic valve replacement [31], removal of polyp in colonoscopy [32], and endoluminal
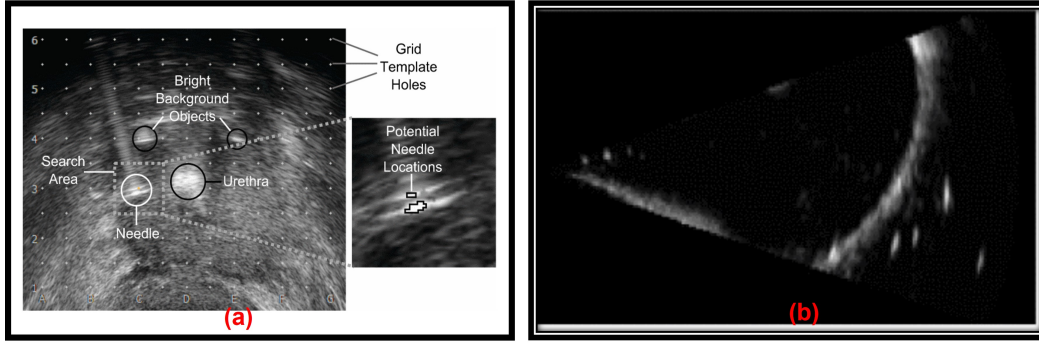
Figure 2.4: Ultrasound image of (a) needle insertion (adapted from [29]); (b) curved robots adapted from ([30])

surgery [33] need the precise movement of robots to reach the target. The error in the shape reconstruction method shall not make such procedures unsafe. Hence, the focus should be on attaining the least possible error during the shape reconstruction. This value can be varied based on the medical scenarios which has to be maintained even in the presence of environmental noise such as electromagnetic interference likely encountered in the operating room. The criteria are summarized in Table 1.1.

Criteria No.	Value
1	Stretchability to deal with the soft and flexible body
2	Safe (Free from radiation dosage and contrast agent)
3	Accuracy should be as maximum as possible
4	Robust to invivo conditions

Table 2.1: Summary of the fulfillment of required criteria by sensing solution

2.3 Thesis Outline

The thesis is presented in six chapters, starting with a state-of-the-art analysis to reach the assessment of a newly developed sensing strategy for the shape reconstruction process considering the criteria outlined in Table 1.1.

Chapter 2 explores the state of the art of shape reconstruction methods through an extensive search of the literature, putting them in perspective with the aforementioned requirements. In the beginning, shape reconstruction methods using intraoperative

imaging techniques, such as fluoroscopy, ultrasound, and endoscopy are investigated. Next, the emerging shape reconstruction solutions using various sensors are investigated. In the end, two solutions, i.e., resistive and inductive-based shape reconstruction methods are identified.

The interest in the resistive sensor-based shape reconstruction method is dependent on the capacity to keep the hysteresis low. Thus, we investigate material selection in Chapter 3 including the choice of the right base substrate to examine different fabrication procedures, aiming to reduce the hysteresis level encountered in the literature.

The alternative possible shape reconstruction solution based on inductive sensing is considered next. As it is less developed in the literature, we conduct a detailed analysis in Chapter 4. In this case, the method is proposed by considering a conventional spring as a variable inductor. At first, an optimization method to adjust the measurement conditions is provided. Next, a full characterization process is conducted to discuss in detail the performance of the sensor. Finally, two robots are presented for testing purposes in which the same inductive sensor is integrated into different application scenarios showing the easiness of sensor integration as well as the capability of precise control.

The developed sensor shows less hysteresis, high repeatability, high stretchability, and acceptable accuracy compared to resistive sensors. Additionally, the inductive sensor is compact and easy to integrate. Hence, it is identified as a suitable candidate for the shape reconstruction process that fulfills the required criteria. Thus, as a next step, the sensor is used for reconstructing the shape of a tendon-driven flexible manipulator which is presented in Chapter 5. The shape of the manipulator is investigated in two steps, with increasing complexity. First, the shape of the manipulator in the 2D workspace is investigated by using a single sensor. After verification of the 2D shape reconstruction process, a more general 3D reconstruction process is performed using multiple inductive sensors. The use of inductive sensors for reconstructing the shape of other soft and flexible robots used in MIS is also outlined in this chapter.

Finally, this research study is summarised and concluded in Chapter 6 by providing future directions to use this sensor in the field of shape reconstruction.

Chapter 3

State of the Art:
Shape Reconstruction Methods

3.1 Introduction

As shown in Chapter 1, a shape reconstruction method is needed that can fulfill the requirement of safety and accuracy while being compatible with the large deformation encountered during the operation of soft and flexible robots. Considering these aspects, the state of the art is explored to identify suitable candidates. An extensive survey of all relevant articles related to shape reconstruction methods used for soft and flexible robots is achieved with a classification based on the sensing principle.

The field of shape reconstruction methods is broad and multidisciplinary. Therefore, a methodology is followed to collect various articles related to this field. A manual search process is performed using the database of Google Scholar and Scopus to select articles published before the year 2020. Since the shape reconstruction process in interventional applications is a growing field, the search is limited to the literature published in the recent 30 years. The list of keywords given in Figure 3.1 is selected based on their use in interventional applications and then combined with logical operators to find the most relevant articles. In addition to existing keywords used in Chapter 1, other synonyms are also used during the search process. For example, a keyword can be "shape" which is used several times in Chapter 1. Seeking papers that contain shape may avoid papers with other synonyms used in the shape reconstruction process, such as pose, curvature, and gesture. Thus, other synonyms are also included in the search process.
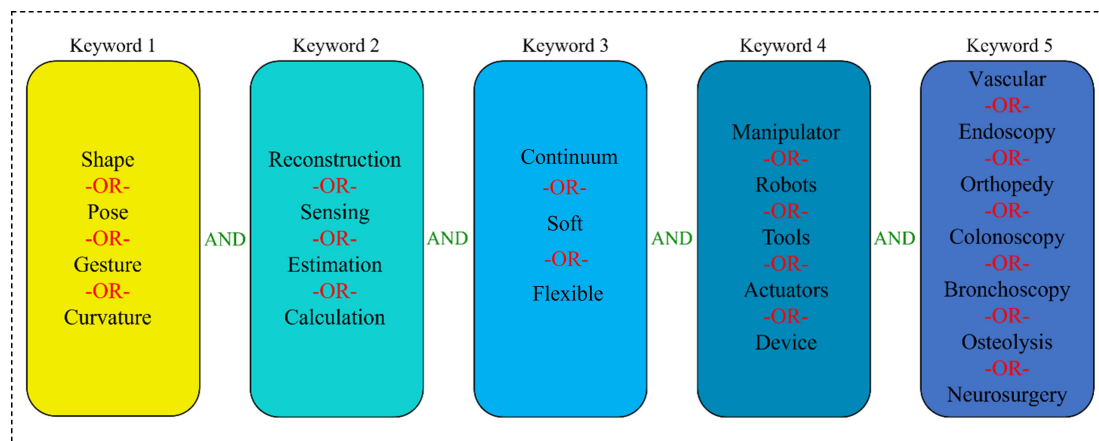
Figure 3.1: Methodology of literature research

The use of keywords in Google Scholar and Scopus databases yields 284 articles, out of which the duplicate findings are removed. The remaining articles are scanned by reviewing the abstracts to discard the unrelated papers. The remaining 130 articles are reviewed and presented in this chapter.

3.2 Imaging-based shape reconstruction methods

The first category of shape reconstruction methods is imaging-based. This can be divided into three parts: fluoroscopy imaging-based, ultrasound imaging-based, and endoscopy imaging-based. These methods have the capability to estimate the shape of robots without consuming extra space and requiring typically no major hardware modifications [34]. In MIS, imaging-based methods remain the gold standard to track and visualize surgical manipulators as they are the most straightforward visualization medium. This section focuses on intraoperative imaging techniques used for the shape reconstruction of continuum and soft robots.

3.2.1 Fluoroscopy-based shape reconstruction methods

Fluoroscopy imaging is a medical imaging technique that uses ionizing radiation to produce two-dimensional images of an object. Typically, it consists of C-arms comprising an X-ray source and photographic film/numeric detector faced opposite to each other. When an object is placed in between the source and the detector, the X-ray beam from the source is passed through the object and is captured by the detector,

thereby producing images of the interior parts of the object. In this case, X-ray is absorbed more in denser materials such as bone or metallic instruments from which one may infer the anatomic structures or detect the shape of the instruments. Two kinds of fluoroscopy imaging processes exist that are biplane and monoplane, which are described in this section along with their use in shape reconstruction procedures.

Biplane fluoroscopy

In biplane fluoroscopy, two C-arms (Figure 3.2) are placed independently around the object, and images are acquired simultaneously. This system synchronously provides two views of the object at different positions using both the C-arms. The first step towards fluoroscopy shape reconstruction is to acquire images from biplane fluoroscopy. The fluoroscopy images are then processed using various segmentation algorithms [35, 36, 37] to find out the device centerline. Finally, a 3D reconstruction method using epipolar geometry is implemented to find the 3D shape of the device.
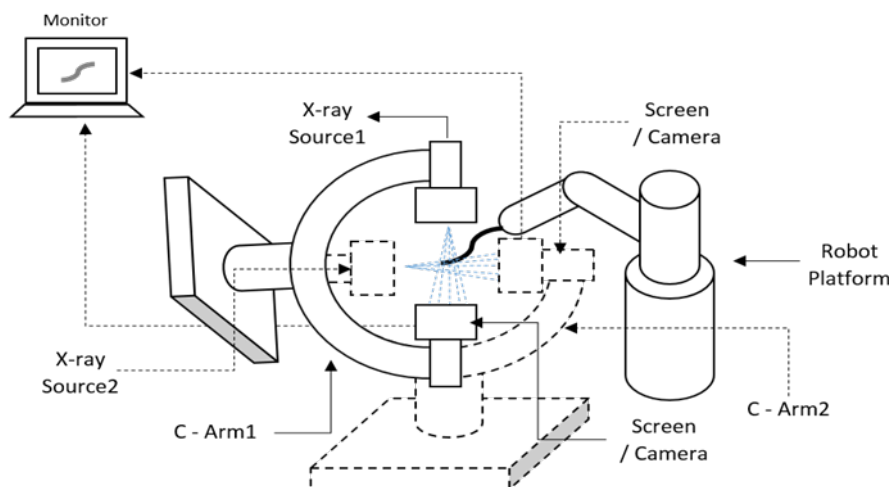
Figure 3.2: Working principle of biplane fluoroscopy system

Baert et al. used biplane fluoroscopy with epipolar geometry to reconstruct the 3D shape of a guidewire in the 3D vasculature [36]. A 2D tracking procedure was implemented based on energy minimization of spline parametrization, where the guidewire was tracked and presented as a third-order B-spline line using acquired biplane images. Finally, the epipolar geometry was used to reconstruct the 3D shape of the guidewire from the biplane images using calibrated C-arm. Schenderlein et al. [37] proposed a method that

implements the B-snake [38] algorithm with biplane fluoroscopy images to reconstruct the 3D shape of a catheter. A line-enhancing feature image was calculated and utilized to generate a 3D image from the 2D projections obtained from the biplane image system. To reconstruct the 3D pose of the catheter, missing image information caused by the asynchronous image acquisition was approximated by linear force interpolation using two consecutive images recorded by one of the C-arms. The evaluation of this algorithm was implemented on 33 virtual image datasets, and the mean catheter pose error was found as 1.26 mm. Hoffmann et al. proposed a method for reconstructing the 3D shape of a catheter using biplane fluoroscopy and epipolar geometry [35]. This approach performed three processes in which the catheter was first identified based on image pre-processing and then transformed into a graph to find an analytical representation model using the Dijkstra algorithm. In the last process, a final estimation of the 2D spline catheter was done using a search method. The catheter was then reconstructed into a 3D shape from the two 2D splines generated during the biplane fluoroscopy. The method was evaluated using 33 biplane images of a catheter. Since there are no 3D data available, the 3D reconstruction was forward projected into planes. The mean error was calculated as 0.4 mm $\pm$ 0.6 mm for the catheter. The error in 3D was calculated by acquiring 13 biplane images at different angulations [39]. The shape error was estimated as 1.2 mm $\pm$ 1.2 mm for the circumferential mapping catheter and 1.3 mm $\pm$ 1.0 mm for the ablation catheter. This method was further extended in [40] by implementing a learning-based framework to adapt the arbitrary line-shaped catheter used in electrophysiology procedure (Figure 3.5(a)). This approach can be adapted to catheters that undergo larger deformations, such as coronary sinus catheters. The improved reconstruction error was estimated as 1.8 mm $\pm$1.1 mm and 2.2 mm $\pm$2.2 mm on phantom and clinical data, respectively.

Monoplane fluoroscopy

Biplane fluoroscopy can be quite precise and consistent because it gives simultaneous views at various positions of the instruments to find out their shape. However, its applications are limited due to the high radiation exposure [41], cost, and bulkiness of the instruments. To address these challenges, monoplane fluoroscopy has also been

proposed. The monoplane systems comprise only one C-arm (Figure 3.3), thus reducing ionizing radiation dose in the shape estimation process. In this case, images are acquired from monoplane fluoroscopy and processed further with a segmentation algorithm to find the robot centerline. Finally, the shape of the robot is reconstructed using existing kinematic models [42].
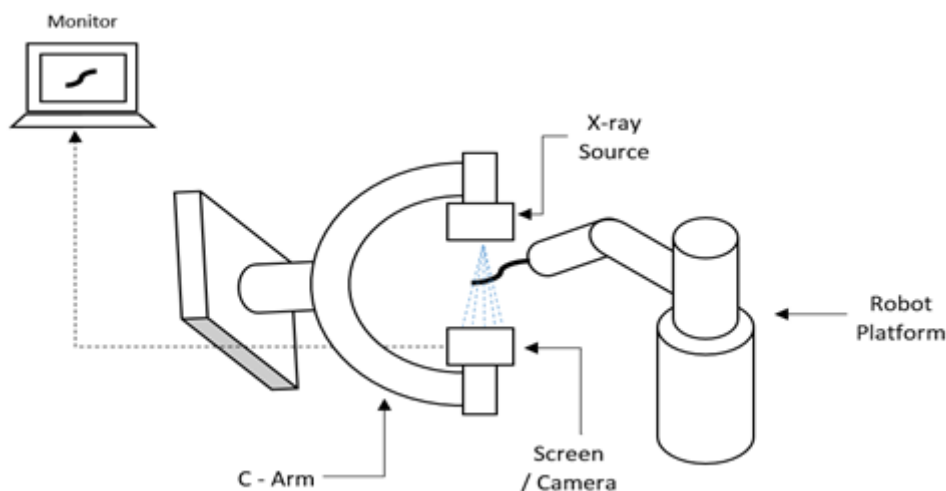
Figure 3.3: Working principle of monoplane fluoroscopy system

Otaka et al. proposed a monoplane fluoroscopy-based shape reconstruction to estimate the 3D shape of snake-like manipulators used in hip osteolysis [43]. This approach used a piecewise intensity-based 2D/3D registration from an X-ray projection with prior knowledge of the shape and kinematic properties (e.g., each rigid structure connected by a pin joint parameterized by a low degree polynomial basis) for pose estimation. The feasibility of this method was tested using simulated projection images of the phantom of the cadaveric system and femoral hip implants simulating a scenario of treating osteolytic regions during hip revision surgery. The joint angle error was estimated as less than $0.07°$. Papalazarou et al. presented a non-rigid structure from motion (NRSfM) method with a kinematic model to reconstruct the shape of a catheter [42]. This method used monoplane X-ray projection made with a small view separation for reconstructing the 3D shape of the catheter. The combination of NRSfM and the model provided a low dimensional parametrization of the catheter, which was then used with an X-ray imaging system to retrieve the 3D shape of the catheter. The suitability of

this model was tested by moving the catheter in free space as well as inside a heart phantom model. Vandini et al. proposed an algorithm that fuses information acquired from monoplane X-ray images with a kinematic model using 2D/3D non-rigid registration to reconstruct the real-time shape of a continuum robot [44]. The algorithm does not require repositioning of the C-arm, thus making it suitable for use in a constrained space. The method estimated 0.88 mm as a shape reconstruction error. The same group also presented another method to reconstruct the 3D shape of concentric tube robots using a unified framework based on Markov random fields which combined the information from monoplane X-ray images with the kinematic model [41]. The reconstructed shape was compared with the ground truth shape producing an error of 2.21 mm ± 1.1 mm. The methods described above are highly accurate and robust. However, these methods mainly rely on continuous exposure to ionizing radiation, which produces 2% of cancers due to the excessive use of these imaging techniques [45]. To address this problem, Lobaton et al. proposed a new idea that used a small number of X-ray projection images to reconstruct the 3D shape of a robot [46]. This approach first estimated the shape of the robot using a kinematic model and then refined the shape using data acquired from the monoplane X-ray projected images. To acquire the images, a method for optimal placement of the C-arm was derived that extracted images at discrete time points. Although the method acquired discrete images at a certain point, it was capable of finding acceptable real-time shapes over the total procedure by integrating the previously extracted images with kinematics modeling. The method was implemented in a simulated bronchoscopy environment which produced a tip tracking error of 0.8 mm. Trivisonne et al. [47] proposed an approach that combined a physical-based model with a non-linear Bayesian filter for reconstructing the shape of a catheter in a 3D workspace. Initially, the model predicted the shape of the catheter, and then it was corrected by Unscented Kalman Filter using 2D single-view fluoroscopy images. The reconstructed shape was compared with the known ground truth producing a 3D Hausdorff Distance of 0.81 mm ± 0.53 mm for the synthetic data set and 1.77 mm ± 0.77 mm for the real data set.

As fluoroscopy shape reconstruction methods are fast, highly accurate, and free from environmental noise, they are widely accepted by clinicians for visualizing different medical instruments. However, the major concern about these methods is safety, given the overuse of radiation dosage and contrast agents. Even with these issues, fluoroscopic methods can't be completely obliterated. The methods presented by Lobaton et al. [46] and Trivisonne et al. [47] are useful due to the intermittent use of fluoroscopic images during the shape reconstruction procedures. Thus, two options are available: i) Methods given by Lobaton et al. [46] or Trivisonne et al. [47] can be adapted since the required criteria are almost fulfilled and research can be directed towards further advancement of these methods to reduce the overuse of ionization dosage. ii) Exploration of an alternative method without the involvement of radiation dosage, contrast agent, and injected chemicals. As the literature presents a wide range of shape reconstruction methods, it seems that finding an alternative method would be easier and time-saving.

3.2.2   Ultrasound-based shape reconstruction methods

Ultrasound is a low-cost and safe imaging modality that can be used to see through the tissue and obstacles. Although the images produced in ultrasound lack good visibility [48], this process could be used to reconstruct the shape consistently. In addition to this, ultrasound imaging is safe, fast, portable, and economical. This method has been implemented to detect the position of medical instruments [49, 50] to determine the position and orientation of thin surgical tools [51], to estimate needle deflection or track the tip of steerable needles [52, 53], and to detect continuum curved robots [34] in different medical scenarios.

Greer et al. [54] presented a real-time segmentation method to reconstruct the 3D shape of curved needles using combined B-mode and power Doppler images from a tracked 2D ultrasound transducer (Figure 3.5(b)). The approach consisted of image analysis and curve fitting steps. In the first step, 2D points along the needle were generated using the image analysis on the pairs of power doppler and B-mode images. Subsequently,

the 2D points were transformed into 3D world coordinates, which were further used for the 3D shape reconstruction process. When this method was compared with manual segmentation of the needle (identifying the needle in each image manually and fitting a 3D polynomial to the identified points), it produced an error of 0.38 mm $\pm$ 0.27 mm in the shape reconstruction process. Carriere et al. proposed a real-time method to estimate the shape of a flexible needle by combining a non-holonomic kinematic model with axial Transrectal Ultrasound (TRUS) image segmentation [55]. In this method, the location of the cross-section of the needle was segmented out of each of the image slices captured normally to the insertion direction of the needle using ultrasound imaging technology. A particle filter incorporated the tracked cross-section and the distance between successive image slices to update the parameters of the kinematic model for each image slice. The parameters of the model were updated up to a pre-defined insertion depth and then the model predicted the shape of the needle for complete insertion. The method was tested in ex-vivo beef phantom tissue and in-vivo clinical images which produced an average tip prediction error of 0.497 mm $\pm$ 0.38 mm (pre-defined depth 60 mm) and 0.44 mm $\pm$ 0.15 mm (pre-defined depth 35 mm), respectively. Waine et al. also employed 2D transverse ultrasound images to visualize the 3D shape of a needle used in the brachytherapy process [56]. They applied an intensity thresholding approach to find out the potential locations of the needle within each 2D transverse ultrasound image. A Random Sample Consensus (RANSAC) algorithm was then implemented to filter out the outliers, and then the remaining points were fitted in a polynomial model to reconstruct the 3D shape of the needle. The method was validated using 21 sets of ultrasound images of the brachytherapy needle embedded within a tissue phantom. The estimated shape of the needle differed by 0.5 mm with respect to the shape measured using a camera. Three images from an insertion depth of 50 mm or greater predicted the entire shape.

Shape sensing using 3D ultrasound imaging has also received much attention in MIS. Neshat et al. proposed a novel method to detect a needle in real-time using 3D ultrasound images [57]. They presented an algorithm based on parameterization of the shape of the instrument (needle) using Bezier polynomials and the generalized

Radon/Hough transform for real-time detection of the needle. This algorithm was implemented on a graphics processing unit using Compute Unified Device Architecture programming. The effectiveness of the method was tested in an experimental testbed for robot-assisted image-guided minimally invasive lung brachytherapy in which the mean axis error remained near 1 mm when compared with EM trackers. Ren and Dupont [58, 34] introduced a new method to detect a curved robot using a 3D ultrasound imaging technique. This method fused geodesic active contours and a speed function based on the enhancement of the tubularity of the robot for detection. The proposed method was tested in ex vivo intracardiac experiments. Although shape sensing using 3D ultrasound imaging is fast and accurate, the cost of 3D ultrasound systems as compared to 2D ultrasound devices is higher which limits the successful implementation of this 3D ultrasound method [56].

It can be witnessed that ultrasound imaging methods have been widely accepted for the shape reconstruction of medical robots in various scenarios. It is popularly used for tracking medical needles in MIS interventions. But it is not limited to only needles, the shape of other continuum robots is also estimated. Since the technology uses ultrasonic sound waves, it can be a safe alternative to fluoroscopy. It is also observed from the literature that ultrasound imaging-based shape reconstruction techniques can achieve sub-millimeter accuracy, thus making them suitable methods for the shape estimation process while satisfying some of the required criteria. However, in some instances, visualization of robots becomes very difficult due to low-resolution ultrasound images and low signal-to-noise ratio based on medical scenarios. To illustrate this, a scenario is given in Figure 3.4 where visualizing the robot seems very difficult. Thus, this method requires heavy computation to estimate the shape during compensating the low-resolution images.

Additionally, a variety of imaging artifacts are generated due to metallic parts of continuum robots and instruments. Dealing with heavy computation and imaging artifacts is challenging and requires further investigation in these methods.
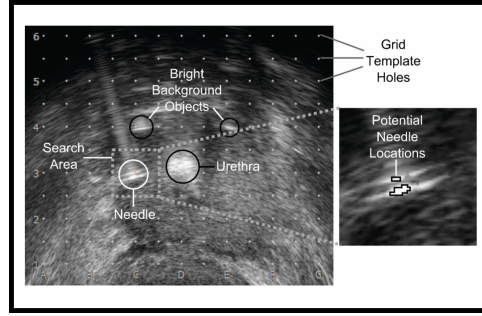
Figure 3.4: Ultrasound images of needles in a scenario of MIS (adapted from [29])

3.2.3 Endoscopic camera-based shape reconstruction methods

Unlike fluoroscopy imaging and ultrasound, endoscopic camera-based shape reconstruction uses the images of the instrument from an endoscopic camera to reconstruct its shape. The shape reconstruction procedure using endoscopes typically follows two approaches. The first approach is called marker-less, in which different feature points are extracted from the images of the instrument taken by the endoscopic camera. These feature points are then used further to find the shape of the instrument. The second approach is marker-based, in which the shape of the instrument is reconstructed by tracking the markers present on it. These approaches are further divided into different categories based on the type of model used, i.e. kinematic model-based and model-free approaches, and the type of instruments used, such as traditional or robot-assisted instruments.

Sestini et al. [59] proposed a marker-less self-supervised image technique based on the kinematic model to estimate the pose of the surgical instruments of a robotic endoscope. In this case, a regressor model was trained to determine the joint values of the instrument using the camera images, and then these values were fused with the forward kinematic model to reconstruct its 3D shape. The validation of the presented method was done in three different data sets consisting of real-time acquisition (phantom and in-vivo) and a semi-synthetic. For the semi-synthetic data set, when the reconstructed shapes were compared with the known ground truth, the mean absolute translation and bending error were estimated as 1.75 mm and 0.47 mm for the left instrument, and 1.17 mm and 0.30 mm for the right instrument, respectively. For

phantom and in-vivo datasets, the reprojection error was calculated with respect to manually annotated ground truth via insertion over union which showed 0.64 (phantom), and 0.55 (in-vivo) for the left instrument, and 0.725 (phantom) and 0.554 (in-vivo) for the right instrument. Reilink et al. also proposed a marker-less approach to reconstruct the 3D pose of an instrument of an advanced flexible endoscope [60] using a kinematic model. The images from the endoscopic camera were processed to find the feature points on the instruments. These features were compared with the calculated position of these points acquired from the kinematic model. Depending on the deviation between the model and observations, the constructed state of the model was updated repeatedly so as to match the model with the observations. The same group extended the study and presented marker-based approaches by placing four markers on the instrument (Figure 3.5(c)) [61]. In this approach, instead of feature points, the position information from the four markers was used to update the kinematic model of the instrument. The approaches were tested inside a colon model. The marker-based approach [60] produced RMS errors of tip tracking as 2.3 mm, 2.2 mm, and 1.7 mm, while the marker-less approach produced an RMS error of 1.7 mm, 1.2 mm, and 3.6 mm along the X (horizontal), Y (vertical) and Z (away from the camera) directions, respectively. Both methods require precise geometry and kinematic models of the robot. However, obtaining such precise geometry may not be practical, and sometimes they do not produce satisfactory accuracy due to uncertainty in the model parameters [62]. Cabras et al. presented an improved marker-based approach using supervised learning with prior knowledge of the kinematic model of the instrument of an advanced endoscope for shape reconstruction [62]. This method reduced the uncertainties produced by previous approaches. With the support of colored markers fixed to the instruments, this method used an image segmentation stage followed by a stage for position estimation. In the beginning, the markers were segmented using an Adaptive Boosting algorithm trained by manually determining foreground and background samples from in-vivo images taken during operations. Thereafter, the centroid of the markers was calculated and used as input to the data pose estimation stage.

With disposable chip-on-tip cameras becoming available, endoscopic camera-based shape reconstruction processes could be implemented in MIS to avoid bulky and costly instruments. This technique uses robot cameras to estimate the shape, thus eliminating the use of any external instrument and high radiation dosage. As this technique is successfully used for highly deformable continuum robots, it can be implemented in MIS targets to estimate the shape of the robot accurately. This can also reduce the space of the workplace by eliminating larger size instruments which could be a great advantage in MIS where the main aim is to optimize the reachable workspace. From the requirement point of view, it addresses the need of a safe shape reconstruction method to deal with large deformation encountered during the operation of highly flexible robots while providing an accuracy of less than 2 mm. However, a direct line-of-sight is required in this process to estimate the shape of the robot. Obstructions or occlusions are common in MIS which will create problems in shape estimation.
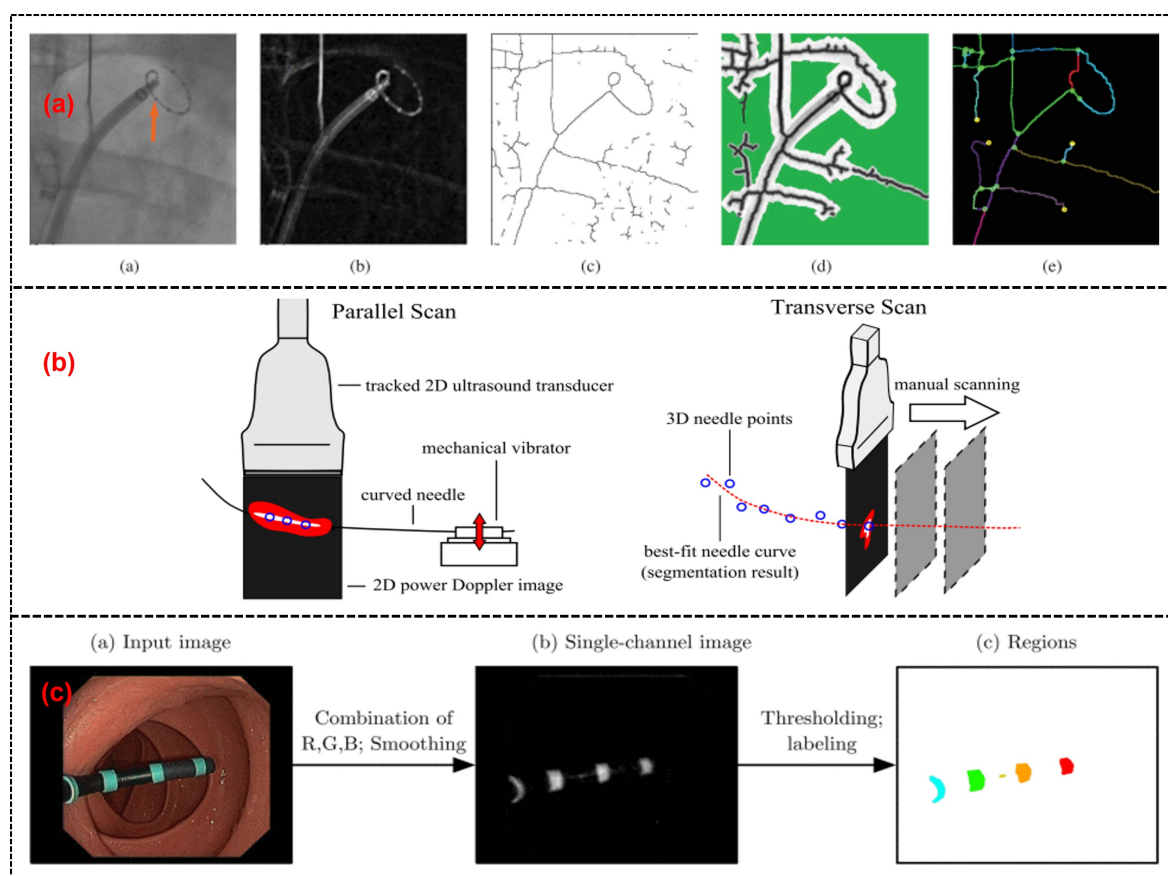
Figure 3.5: (a) Shape estimation using biplane fluoroscopy images (adapted from [40]); (b) 3D shape reconstruction of a curved needle using ultrasound images adapted from ([54]); (c) marker-based shape sensing using endoscopic camera images [61]

In summary, medical imaging methods remain standard procedures for visualizing the shape of continuum manipulators in MIS till date despite the advancement of other shape reconstruction processes. Most clinical personnel rely on these methods as they involve direct visualization without the requirement of calculation of strain and other complex processes. These methods meet some of the requirements for reconstructing the shape of highly soft and flexible robots. The requirement of a shape reconstruction method that deals with highly deformable robots is fulfilled, as they estimate the shape only handling the acquired images rather than measuring the strain on the robots using sensors. From the literature, it is also noticed that there is no involvement of environmental noise such as electromagnetic interference, thus they can be adopted in different medical environments. Imaging methods are also capable of achieving less than 2 mm errors in the shape estimation process, making them a suitable candidate. However, the major issues related to these methods are over usage of radiation dosage in the case of fluoroscopy, the low signal-to-noise ratio in the case of ultrasound, and unable to produce quality shape information in the presence of occlusion and blood in the case of endoscope camera-based techniques which still remain unresolved.

3.3 Sensor based shape reconstruction methods

Sensor-based reconstruction methods are getting attention recently since they address some of the existing issues of imaging-based methods. In this case, the shape reconstruction process is performed by acquiring the strain or positional information from these sensors. The most frequently employed sensors are optical sensors, position sensors, and passive stretchable sensors. In this section, we discuss the sensor-based shape reconstruction method by using the above-mentioned requirements.

3.3.1 Fiber optic-based shape reconstruction processes

The first sensor-based shape reconstruction method is fiber optic sensors-based. These sensors consist of a light source, a carrying medium that is sensitive to environmental measurands, and a receiver [63] which detects the modulation of the emitted light in

terms of intensity, wavelength, phase, or polarization [64]. Thanks to their miniature size, immunity to electromagnetic interference, and flexibility, they are used in many contexts to develop various types of sensors from strain to chemical measurement [65].

This section focuses on sensing methods that have the potential to reconstruct the shape of the continuum robots through strain information from fiber optic sensors. After a brief discussion of intensity-modulated, phase-modulated, and scattering-based methods, Fiber Bragg Grating (FBG), an extensively studied technique of wavelength-modulated method, is presented.

In intensity-modulated methods, an optical fiber is equipped with a light source and a photodetector. When a measurand causes deformation in the sensor, the intensity of the detected light modulates [66] due to reflection, transmission loss, and micro/macrobending [67]. Zhao et al. demonstrated curvature sensing for orthotic systems [68] which consisted of U-shaped fibers for sensing. One side of each U-shaped fiber was etched to reduce internal reflection, resulting in loss of light while traveling. As one side is etched, the amount of light dissipation was affected during bending, which was measured via a photodetector and then correlated to the curvature.

Similarly, Searle et al. showed the curvature sensing of a flexible manipulator [69], which consisted of fiber optic cables and reflective surfaces. The distance between the reflective surfaces and fiber ends varied with the bending of the manipulator, which caused a change in reflected light and allowed correlation with the bending measurement. Sareh et al. presented pose sensing of a soft actuator [70] in which three stretch sensors were used. The stretch sensors are optical fibers with a loopback design sewn into the braided sleeve layer of the actuator. The loopback design allows the sensor to bend, elongate, and contract with the application of the deformation. Figure 3.6 shows the implementation of the sensors into the actuator. When the actuator bends, the measurable light varies due to macrobend loss allowing to detect the bending angle. To et al. presented a soft sensor that can measure the curvature by coating the stretchable waveguide with a non-stretchable and reflective metal layer [71]. When the sensor undergoes a deformation, micro-cracks within the reflective layer cause the loss in intensity of the light.
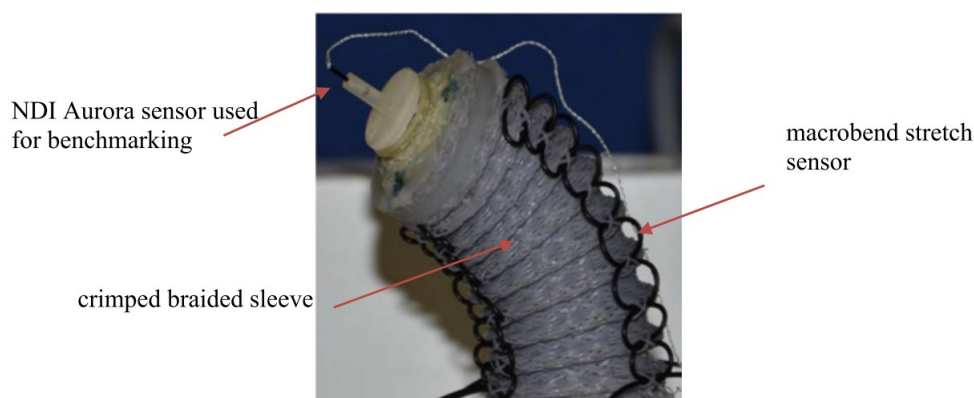
Figure 3.6: Stretch sensor using optical fiber implemented to a soft actuator [70]

Phase-modulated fiber optic sensors work on detecting the phase change of the light. Typically, a modulation in phase because of a measurand is detected interferometrically by comparing an isolated reference phase [64] using Fabry-Perot, Mach-Zehnder, Michelson, or Sagnac method [72]. Compared to intensity-modulated, it shows higher sensitivity and accuracy but requires more complex interrogation and data processing techniques [73]. Zhou et al. presented a curvature sensor [74] that included a dual-core photonic crystal fiber (PCF) spliced between two single-mode fibers. When the PCF is bent, phases of the propagating light at the PCF cores differ because of the inherent reflective index variations and changes in the optical path. The phase difference was used for curvature detection using Mach-Zehnder interferometry.

Scattering-based fiber optic sensors catch the scattering of propagating light through an optical fiber and the intensity of the scattered light is mapped using a reflectometer [75] by using Rayleigh, Brillouin, or Raman mechanism. Rayleigh scattering occurs when propagating light collides with inhomogeneities in the fiber optic core (i.e., structural variations, impurities [76]). The inhomogeneities act as a scattering center, reflecting light in nearly all directions with negligible energy loss. Moreover, this elastic scattering does not change the frequency [76]. Unlike Rayleigh, Brillouin and Raman scattering mechanisms are inelastic, and there is a change of energy, resulting in frequency change [64]. Galloway et al. presented 3D shape sensing of a soft actuator [77] in which a multicore fiber with one central and three outer cores that helix around the center core was placed into it. Under deformation, the outer cores were subjected to

tension/compression while the center core remained neutral, changing backscattered signals. Then, the scattering was detected using optical frequency domain reflectometry. Since the input light was split between a reference path and a measurement path which was combined with backscattered signals, the shape of the actuator was reconstructed by comparing the reference and measurement signals.

The intensity and phase-modulated methods mainly focus on single bend curvature sensing. Therefore, they can be adapted to medical robots with single bend curvature. However, in continuum robots, multi-bending with accompanying torsion is common. By using the scattering-based method, curvature and torsion sensing were demonstrated [77].

On the other hand, wavelength-modulated methods detect wavelength shift, which is independent of the light source intensity [64]. The following section summarizes the FBG methods used for 2D/3D shape reconstruction of continuum manipulators with single and multi- bending modes.

FBG is a type of intrinsic sensor [78] which is deployed by changing the refractive index of the core of the optical fiber. Chronologically, the fabrication techniques of the FBGs are photosensitivity [79], holography [80], phase masking [81], and femtosecond laser [82]. When an incident spectrum of light propagates through FBG, a narrow wavelength of light is reflected while the rest is transmitted. The reflected wavelength is called Bragg wavelength which has cross-sensitivity to strain and temperature. Thus, when an FBG is subjected to them, the reflected Bragg wavelength shifts proportionally. The FBG response is characterized by measuring the shift using an interrogation system. Moreover, the Bragg wavelength can be adjusted in the design stage through changing effective refractive index [83], cladding/core indexes [84], and grating period [85]. This adjustment is useful for multiplexing which allows for inscribing many independent FBGs along the same fiber while avoiding the overlapped Bragg wavelengths. It allows for monitoring different variables [86, 87] or distributed/quasi-distributed measurement of a single variable [88, 89] using one fiber with FBGs. The working principle is shown in Figure 3.7.

Miniature size, work over a long distance, immunity to the electromagnetic fields,
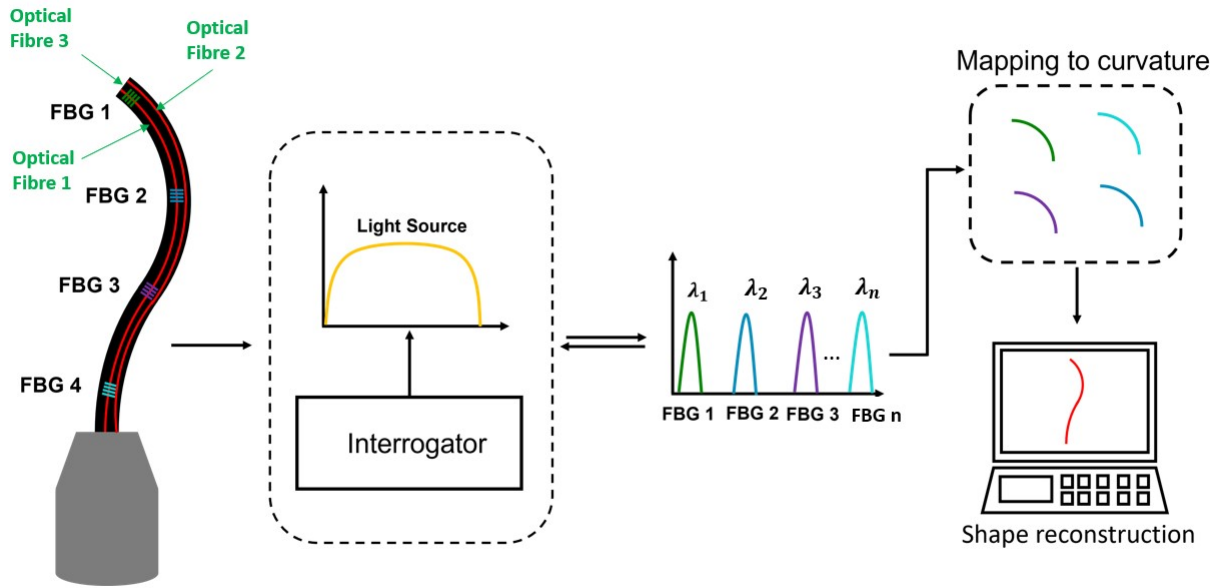
Figure 3.7: Working principle of FBG based shape reconstruction methods

chemical inertness, high sensitivity and repeatability, and fast response features [90] make the FBG technology a prominent candidate to be used for shape reconstruction of continuum robots in the medical field.

The shape of continuum robots changes through curvature, torsion, extension/contraction, and their combinations along their body [91]. When the shape of a continuum body changes, the induced strain at the FBG causes the wavelength to shift, then the shape is reconstructed by characterizing this shift using the following steps typically: i) strain on each fiber is calculated through the wavelength shift; ii) using the strain, curvature and torsion are computed; iii) missing curvature and torsion are obtained through interpolation; iv) shape is reconstructed using obtained data [92]. FBG-based shape reconstruction is applied to various continuum structures, such as tendon-driven manipulators [93, 94, 95, 96, 97], pre-curved robots [98], soft actuators [99, 100, 101, 102, 103], catheters [104, 105], and needles [106, 107]. Moreover, it was proposed as an external sensor [108] to be inserted into different continuum instruments.

Regarding tendon-driven manipulators, Liu et al. presented FBG-based shape reconstruction of a large curvature manipulator [95]. The maximum curvature of the manipulator was much higher than the maximum bending strain of the fiber; thus, each

fiber with three FBGs was coupled with Nitinol wires as a supporting substrate in a triangular configuration, aiming to reduce the bending strain on the fibers. Experimental tests were conducted in-plane under constant curvature assumption, and an average curvature error of 3.14% was reported for the 35 mm long manipulator. Then, the study was extended for non-constant curvature detection in [96]. Experiments were evaluated in free bending and bending with an obstacle case which produced maximum distal tip tracking error of 0.4 mm and 0.93 mm, respectively. It allows detecting large deflection. However, this deals with a complex fabrication method [109]. Sefati et al. presented a method for fabricating a large deflection FBG sensor by embedding one FBG array and two NiTi wires inside a polycarbonate tube [110]. This sensor was used for shape reconstruction and controlling a continuum manipulator [111]. In [97], the shape of the similar manipulator was reconstructed by using model-dependent and data-driven approaches. It was reported that the data-driven approach uses all FBGs' data simultaneously and does not rely on geometrical assumptions as in the model-dependent approach, resulting in reducing reconstruction error, especially in large deflection. The maximum absolute error of 3.63 mm and 0.62 mm were reported for model-dependent and data-driven approaches, respectively for the 35 mm long manipulator. The same group proposed another data-driven learning model for shape reconstruction of a similar manipulator [112]. This method incorporated three supervised machine learning algorithms, which were trained on the collected data to map measurements from FBG to the distal-end position. This measurement was further used in a data-driven optimization-based shape reconstruction process to reconstruct the manipulator shape. When the data-driven approach was compared with the model-dependent approach, it produced a maximum distal end position error of 1.22 mm for data-driven and 3.19 mm for model-based which showed a good performance of the data-driven process. Roesthuis et al. proposed a 3D shape sensing of a tendon-driven manipulator (Figure 3.8(a)) for closed-loop control [94]. In this case, a Nitinol wire of 1 mm in diameter and 160 mm in length with an integrated array of FBGs serves as the sensor for shape reconstruction. The Nitinol wire comprised

three optical fibers and each fiber consisted of four FBG nodes. Then, the wire with fibers was inserted into the backbone of the manipulator to estimate its curvature by measuring axial strain on FBG sensors. After that, the shape was reconstructed using the curvature information which was further used to steer the manipulator tip. It was demonstrated that tip tracking error was significantly reduced thanks to reconstruction feedback from FBGs. This study was also extended [113] to find interaction force while performing shape sensing simultaneously using rigid-link modeling. The 3D shape generated from this process was used as feedback for control. Experimental results showed a maximum trajectory error of 1.37 mm when the manipulator was steered along a straight path. In addition to the straight fiber configurations in [113, 96, 97], Wei et al. proposed a helical configuration of a single fiber with eight FBGs for a tendon-driven flexible robot [93]. The fiber was supported with Nitinol wire. The dual-helical (i.e., clockwise and counterclockwise) configuration of the fiber had the potential for torsion and curvature measurements as well as temperature compensation. The FBGs along the fiber was placed with axisymmetry according to the neutral axis of the robot. This placement aimed to produce the same wavelength shift but in the opposite strain sign at the two axisymmetric FBGs, which can also be used for temperature compensation. The torsion and curvature tests were conducted separately. For the torsion test, a fiber that has 4 FBGs with Nitinol wire was bounded around a 20 mm diameter and 400 mm long silicone rubber shaft. Results showed that wavelength shifts linearly when one end of the shaft was rotated 360° while the other end was fixed. To demonstrate constant curvature in-plane bending, a fiber that has 8 FBGs with Nitinol wire was placed onto a 25 mm diameter and 110 mm long 3D printed flexible robot. The curvature experiments were compared with camera images which resulted smaller than 0.1 mm in-plane bending error.

Regarding pre-curved robots, Xu et al. demonstrated shape and force sensing of a pre-curved Nitinol tube [98]. Three fibers with one FBG each were helically wrapped around a tube (Figure 3.8b). A nonlinear force-curvature-strain model was developed to measure curvature, torsion, and force simultaneously based on strain changes of the

FBGs. In addition to shape and force sensing, the effect of FBG length was investigated. Two FBG sensors (i.e., 1 and 5 mm) were tested in terms of bending capacity and noise. It was reported that while FBG with 1 mm in length allows larger bending than 5 mm one, the latter shows a better resolution. To obtain larger bending, FBGs with 1 mm in length were used during shape and force sensing of pre-curved tube experiments. After calibration, a series of weights (up to 150 g) were added to the distal end of the tube. Under maximum loading, the error for curvature measurement was reported as 2-4% of the total range measured.

With the increasing application of soft robots, FBG-based shape reconstruction processes are applied to soft structures [100, 101, 114]. He et al. presented the shape sensing of a pneumatic soft bending actuator (Figure 3.8(c)) [100]. A fiber with two FBGs was placed on the bottom surface of the 180 mm length actuator. In this case, the sensor was capable of estimating the shapes up to curvature of 30 m^{-1} [101]. In another approach, Hou et al. proposed a new FBG-based pose reconstruction method using an improved piecewise constant curvature model for a soft manipulator of length 154 mm [114]. In this case, a helical design of FBG considering the axial elongation/compression of the manipulator was proposed, which has the potential to measure large deformations. The experimental results showed an interesting accuracy with a maximum error of the end effector coordinates 0.76 mm when compared with the ground truth coordinates given by vision. However, there is no availability of torsion information.

These processes for catheters were also widely investigated [105, 115, 116, 117]. Khan et al. presented the 3D reconstruction of a catheter (Figure 3.8(d))using four multicore fibers (each fiber with four cores and each core with six FBGs) into a 118 mm long catheter [104]. Although one multicore fiber with three or more cores is enough for 3D shape reconstruction, they used a redundant multicore fiber to increase reliability against sensor failure. Experiments were conducted in various curvature and torsion conditions, reporting a maximum reconstruction error of 1.05 mm. Moreover, Shi et al. proposed the reconstruction of a 1000 mm long catheter with three optical fibers with eight FBGs
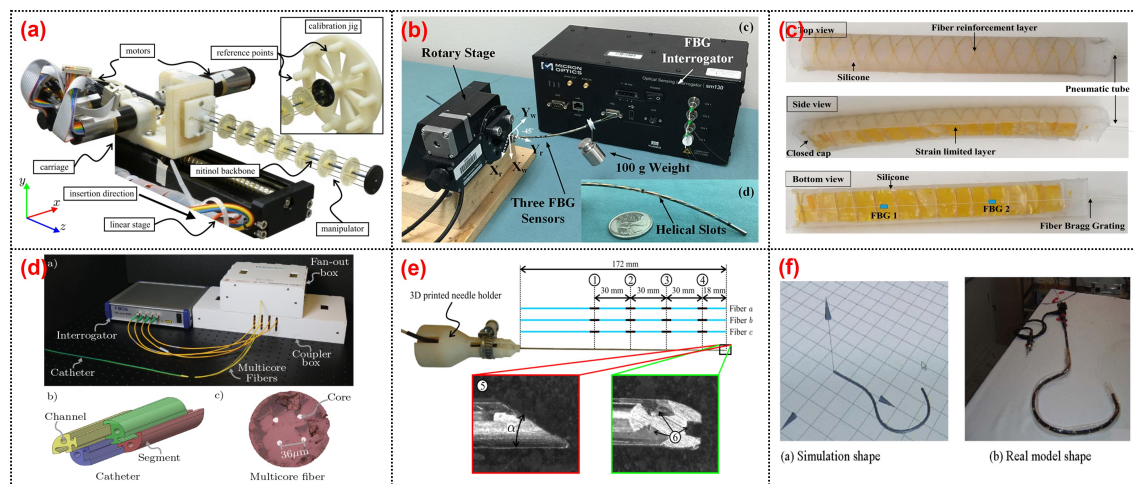
Figure 3.8: Shape sensing using FBG (a) Tendon driven manipulator (Adapted from [94]); (b) pre-curved nitinol tube (Adapted from [98]); (c) soft manipulator (Adapted from [100]); (d) catheter (Adapted from [104]); (e) needle (Adapted from [107]); (f) colonoscope (Adapted from [108]).

each [105] assembled in a triangular configuration. Although the result of a single bend mode was presented, the accuracy of the sensor was not reported. Recently, Fei Qi also presented a reconstruction process for a catheter using the curvature information from the FBG sensor in a discrete interpolation fitting method [116]. The information was used in a control strategy to improve the bending accuracy of the robot. Results showed that the curvature error and direction angle errors are 1.42 % and 10.3 %, respectively.

In the case of needles, Park et al. presented a shape reconstruction of a 150 mm long MRI-compatible biopsy needle [106]. Three fibers with two FBGs each were placed into the needle shaft in a triangular configuration. It was calibrated by applying in-plane loads and changing temperature without strain which was used for shape reconstruction. The maximum RMS error of the tip deflection was reported as 0.38 mm in the range of ±15 mm while the temperature was compensated. On the other hand, Roesthuis et al. presented the 2D and 3D shape sensing of a 172 mm long Nitinol needle [107] by placing three fibers with four FBGs in a triangular configuration (Figure 3.8(e)). The shape was reconstructed from curvature and torsion through a beam theory-based model. The experiments were conducted in free space and gelatin phantom in which the maximum reconstruction errors in free space (gelatin phantom) were presented as 0.2 (0.57) mm for in-plane with a single bend, 0.51 (0.53) mm for in-plane with a double bend, and 1.66

(0.74) mm for out-of-plane. Kim et al. proposed another method based on elastic rod theory and Lie-group-theory approach to reconstruct the shape of a needle used in MIS [118]. This approach used the information from 3 embedded FBG sensors to reconstruct the shape. Two tests were performed where the needle was inserted into a single layer and a double layer homogeneous phantoms and the reconstructed shape was compared with the shape produced from image analysis. The mean tip deflection error was estimated as 0.2 mm ± 0.12 mm for the single layer and 0.47 mm ± 0.17 mm for the double layer phantom, respectively. Later, this study was extended to test the shape sensing capability of the needle [119] when inserted into an inhomogeneous phantom consisting of soft gel and meat, which produced a maximum error in the tip deflection as 0.38 mm ± 0.27 mm.

Alternatively, the FBGs are also used to develop external tools to be inserted into channels of flexible instruments. This approach separates the sensors from the robot body while using minimum usage of structure lumen and providing the potential of inexpensive fabrication and maintenance [120]. In this case, a tube containing FBG nodes is fabricated outside the body of the robot and can be inserted through the channels of the robot for shape sensing. After the 3D shape sensing concept of a colonoscope was suggested in [121], Yi et al. presented the details in [108] as follows. A shape memory alloy of 0.76 mm in diameter was equipped with four fibers with five FBGs each. The sensor was used to reconstruct the shape of the colonoscope inserted into its biopsy channel. The shape of the colonoscope was reconstructed based on differential geometry, considering curvature and torsion in the ambient temperature. After a calibration matrix was obtained considering sensor packing error, the shape of the sensor was reconstructed for in-plane bending and spatial conditions (Figure 3.8(c)), reporting the minimum error of 4.1 mm. As a different application, Ryu and Dupont developed a sensing tube that includes three surface-mounted fibers in a triangular configuration [120]. A 1.4 mm in outer diameter tube tends to use the minimum amount of lumen, not to affect the curvature of the robot which is inserted into. Moreover, it allows integration into various tools as demonstrated with micro forceps. The sensing tube allows large curvature and strain reduction between fiber and compliant material. However, it reduces the strain transfer from compliant

polymer to stiff fiber. To address that, a mechanics-based strain transfer model was derived and validated through simulation and experiments. A low-cost prototype with one fiber with a single FBG and two fibers without FBG was tested in-plane bending. A robot of constant curvature and 80 mm in length was assumed according to the intracardiac scenario. While the tip position error was reported as 0.84 mm, the tip orientation error was given as 1.21°. On the other hand, Jäckle et al. used a multicore fiber for shape sensing of flexible instruments for endovascular navigation purposes [92]. A 380 mm in length multicore fiber has one central core and equally distributed six outer cores, each containing 38 FBGs. For 380 mm sensor length, experiments in free space resulted in an average error of 0.35-1.15 mm and a maximal error of 0.75-7.53 mm. In the scenario with endovascular reconstruction, they obtained an average error of 1.13 mm and a maximal error of 2.11 mm.

All in all, the FBG-based strategy is a promising candidate for the 2D/3D shape reconstruction of continuum flexible and soft robots. The small diameter of fibers allows shape reconstruction of structures in 1 mm or even smaller diameters. The average shape estimation error reported in the literature varied from 0.38 mm to 7.53 mm depending on the applied instrument and tested configuration. In the case of shape reconstruction of needles, this method has the capability to estimate the shape achieving submillimeter accuracy, i.e., an error less than 0.5% of the length [80]. While for catheter and flexible instruments, the reconstruction approach is able to achieve errors less than 0.9 % for simple C-curve [92, 104], and it can reach up to 2% for more complex configurations like S-curve [92]. Though this method produces many advantages such as accuracy, miniaturization, and high sensitivity, it has some limitations such as cross-sensitivity and limited stretchability. Since FBGs have sensitivity to temperature, various approaches are suggested to eliminate the temperature effect to increase the shape reconstruction accuracy. To mention the stretchability challenge, especially for detecting large curvature which is one of the requirements to be addressed, a reinforcement element to be attached to fibers such as Nitinol wire [95] is used to decrease the amount of induced strain on the fibers. Approaches for reconstructing the shape of highly flexible soft robots have

also been addressed in [100] by using different approaches. However, these methods require complicated and tedious processes along with extraneous calibration procedures for system parameter identification. They also require many FBGs which increases the cost of the overall system. In addition to this, FBG-based methods may not be suitable for soft robots with a pure extension despite the improvement of the stretchability issue. Even though FBG-based methods show limitations when it comes to highly soft and flexible continuum robots, there are some procedures that can be implemented in this context [95, 100]. However, these methods still need improvement to deal with high deformation. Recently, position-based shape reconstruction methods are also proposed in the literature that address the issue of stretchability while avoiding the high cost and complicated calibration processes. Thus, these methods are explored in the next step.

3.3.2 Position-based sensor shape reconstruction processes

Position sensors (POS) typically can measure the relative position and orientation from a fixed or reference point. Examples are electromagnetic (EM) and permanent magnet trackers, inertial measurement units (IMU), etc. These sensors are very widely used [122] in MIS to track the position of the tool or robots involved due to real-time tracking capability, freedom from the line of sight, and accuracy. Recently, they are also gaining attention for reconstructing the shape of robots due to these advantages. Since EM and permanent magnetic trackers have been widely accepted for the shape reconstruction process, they are discussed in this section. The working principle of EM trackers is based on mutual induction in which an EM field generator generates a known electromagnetic field to determine the pose information of the sensors within its workspace. On the other hand, the permanent magnets are tracked by measuring the magnetic field change due to its movement using a sensor system. Position-based shape reconstruction produces certain advantages over FBG shape reconstruction, such as freedom from line-of-sight and allowing for reconstructing the shape of a highly flexible robot. The overall working principle of position-based shape reconstruction is shown in Figure 3.9.
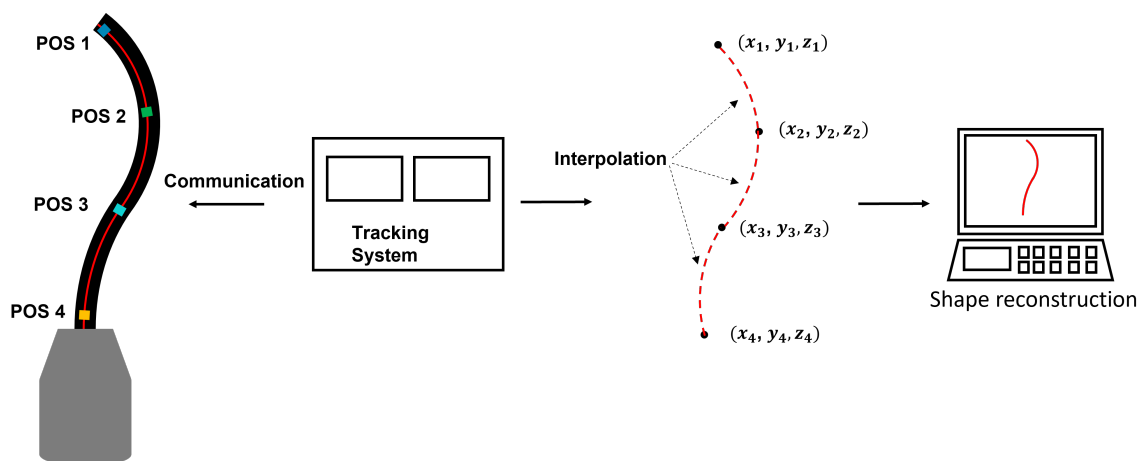
Figure 3.9: Working principle of position-based shape reconstruction method

Electromagnetic tracking-based shape reconstruction methods

Electromagnetic tracking is widely used in different medical applications. It starts from image-guided interventional surgery [123, 124], more recently, to medical device navigation [125, 126], thanks to their miniaturization, precision, easy to set up installation, and freedom from the line-of-sight. Consequently, electromagnetic tracking is a promising method for tracking and localizing the devices in clinical applications such as bronchoscopy [127], endoscopy [128], and knee arthroplasty [129]. In addition to these applications, EM sensors are also used for the shape reconstruction of medical devices by placing multiple EM sensors along the length of the device.

The EM shape reconstruction process depends upon the location and orientation of the sensors attached to the device without requiring curvature information. Various strategies have been proposed for shape reconstruction by fusing EM tracking data and the kinematic model of the manipulators. For example, Tully et al. proposed a filtering method that estimated the shape of a 300 mm long highly articulated snake robot [130, 131]. The non-stochastic filtering algorithm used a custom extended Kalman filter, which combined the pose data from an EM sensor present at the tip with the kinematic model of the robot to reconstruct the shape. Initially, a benchtop experiment was performed, in which the estimated shapes were compared with the true shapes of the robot generated from post-processing data producing a maximum error of 10.53 mm for a 300 mm long manipulator. In the second experiment, the shape of the robot was

estimated by navigating the robot along the epicardial surface of a porcine heart. Though the method showed promising results for benchtop experiments, it was unable to provide qualitative data due to the unavailability of ground truth in animal experiments.

In another approach, Dore et al. [132] presented catheter navigation and shape reconstruction approach by combining in-situ real-time EM tracking data with physical-based catheter modeling and simulation on real-time insertion length measures (Figure 3.10(a)). The catheter was comprised of seven sensors (one 6 DoF sensor at the tip and six 5 DoF EM sensors are installed at 125 mm) across its length. A probabilistic framework using Kalman Filter was employed to fuse the information from the catheter motion algorithm and the electromagnetic tracking data for estimating the shape of the catheter. The approach was validated in in-vitro experiments by inserting the catheter inside a 2D silicone phantom of the aorta. The average shape error was estimated as 2.1 mm compared to the ground truth resulted from the camera. Ryu et al. proposed a method to reconstruct the shape and evaluate the contact force of a colonoscope [133]. The positional and rotational information from two EM sensors connected to the distal and proximal end of the colonoscope with its mass and insertional length were used in a model to reconstruct the shape. Apart from the shape reconstruction process, the contact force was also estimated by employing the Cosserat-rod theory. The position error for specific node points was calculated by comparing to the simulated shape which remained in between 2-3 mm even if the sensing length changed from 300 mm to 700 mm.

The accuracy of the methods presented depends upon the model, and they may not work in an unknown payload if the models do not include the loading condition. Some models also use constant curvature assumption which is very difficult to avail practically. Song et al. presented a shape reconstruction method for flexible robots based on Bezier curves using the length of each section along with positional and directional information of the distal end of each section of the robot [134, 135]. This method shows high accuracy in shape reconstruction with marginal modification to the robot, wherein no kinematic

model for reconstruction is needed. This method was first applied in a single section robot of 135 mm in length by mounting a 5 DoF EM sensor on the tip and then extended to the robot with two bending sections by placing three 6 DoF along its length. The method works well with an unknown payload applied at the tip of the robot. The veracity thereof was duly simulated and experimented where the mean reconstruction error was found as 1.7 mm. The proposed reconstruction approach provided acceptable results for shape estimation no matter how the robot bends in the same plane. However, as it used quadratic and cubic Bezier curves, the efficiency decreases if a section bends more than a specific angle (i.e., 90° for quadratic and 180° for cubic) or in a different plane. The same group also proposed a method to reconstruct the shape of a continuum tubular robot developed for nasopharyngeal biopsy [136]. The robot was comprised of three EM sensors whose positional information was used in a third-order Bezier to reconstruct the shape in the 3D workspace. The reconstructed shape was compared with shapes drawn on the graph paper producing a mean error of 1 mm along the length.

Ma et al. presented a novel real-time shape reconstruction process for 176 mm long and 15 mm in diameter flexible manipulator [137]. In this case, the shape and twist information can be estimated simultaneously using three 6 DoF EM sensors. The proposed method reconstructed the shape using EM sensor information in a cubic Bezier curve, while twist information was calculated using EM sensor information with a polynomial fitting. This method can estimate the deformation of the manipulator with large bending along with twisting. A vision-based offline method was also developed to validate the EM sensing method showing a mean reconstruction error of 1.9 mm.

The above strategies are widely used in shape sensing and show many benefits with respect to other sensing modalities. However, they provide discrete pose information along the manipulator and require the adoption of an interpolation scheme for shape reconstruction. In addition to this, these methods produce limited robustness as they rely on magnetic field measurement, which is affected by the presence of ferromagnetic material. Some approaches using EM tracking information with other sensing modalities

and predictive models [130, 132, 138] are also proposed to address these issues. Tran et al. introduced a probabilistic framework that merged EM measurements with dense 2D information extracted from fluoroscopic images to deliver a reliable estimation of the 3D shape of the catheter [139, 140]. A physical-based simulation environment that gives ground truth catheter shape was developed to verify the performance of the approach, which produced a median RMS error of 3.7 mm.

Permanent magnet-based shape reconstruction methods

Shape reconstruction processes based on EM sensors show numerous advantages such as high sensitivity and accuracy, miniaturization, and absence of line-of-sight. However, they need external tracking systems which add cost to the system [141, 142]. Furthermore, these sensors require multiple leads for connection which affects the adaptive capacity of the robot [143]. To address the above drawbacks, alternative methods have been investigated to reconstruct the shape of the robot based on the detection of permanent magnets connected to it. Guo et al. proposed a sensory scheme by integrating small cylindrical permanent magnets and three-axis magnetic sensors into a 195 mm long continuum robot made from disks and NiTi core (Figure 3.10(b)) [142]. The single section of the robot included two sets of the detection system in which each comprised of a permanent magnet and a three-axis magnetic sensor. When the robot moved, the change in the magnetic field due to the movement of the permanent magnet was measured by the magnetic sensor, which provided positional information. Then a quadratic Bezier curve was implemented using the positional information from the detection system to reconstruct the shape of the robot in the 2D plane. The maximum terminal position error was reported as 9.4 mm.

Alternatively, Zhang et al. proposed a method that illustrated the navigation of a wire-driven continuum surgical robot based on permanent magnetic tracking [143]. The distal end of the robot consisted of a small permanent magnet that can provide 3D position and 2D orientation of the tip of the robot when interacting with a magnetic sensor array. Finally, using the positional information of magnets in a third-order Bezier curve, the shape of the robot was estimated. The proposed tip-tracking and

shape sensing method was verified using an experimental platform consisting of the robot and some obstacles made from Lego. Three targeted positions were tested using tip feedback control, and the mean position error for the tracking-based method was estimated as 1.1 mm ± 0.5 mm. Wang et al. [141] also presented a general joint position tracking and shape reconstruction of a continuum tubular robot based on multi-magnet tracking. Two small permanent magnets were mounted at the distal end of each tube of the robot. These magnets provide 3D position and 2D orientation information by communicating with the magnetic sensor array. The shape of the robot was reconstructed based on a third-order Bezier curve using the information from the sensory system. The method was verified by performing different experiments and comparing them to the actual values generated from the placement of the robot on a graph which produced a mean error of 1.38 mm.

Even though permanent based reconstruction methods show many advantages compared to EM based, such as removal of expensive tracking system and free from multiple sensing leads, the accuracy still compromises with the presence of surrounding magnetic field and ferromagnetic materials.
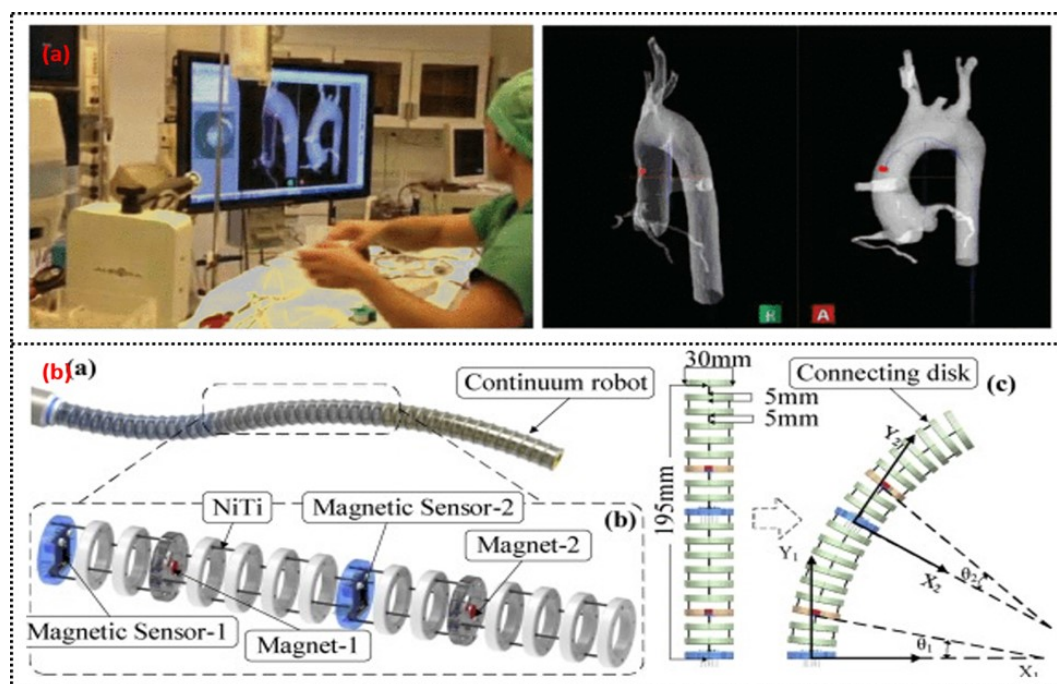
Figure 3.10: (a) Catheter navigation using EM sensors (adapted from [132]); (b) Continuum robot shape estimation using permanent magnet (adapted from [142]).

Position-based shape reconstruction methods have many benefits like freedom from the line of sight, miniaturization, high sensitivity, and accuracy. Due to these advantages, they have been widely used in the shape reconstruction process of catheters, tubular, and articulated robots. Due to the miniature size, they have the ability to be implemented in small-size continuum manipulators of radius approximately near 2.4 mm [132]. As sensors are placed at discrete points, they do not show the issue of stretchability and can be implemented in highly flexible manipulators. Despite many advantages, the methods are unable to provide uniform accuracy throughout the tracking area, as the accuracy depends upon the tracking volume. The issue is addressed by Reichl et al.[144] by proposing an EM servoing method in which the EM field generator was connected to a robot arm. In this case, the EM tracking detected the sensors in a subspecific volume with acceptable accuracy, and then the robot was positioned to keep the sensors near to the center of the tracking volume during movement. Even though position-based sensors are prone to environmental noise, the method presented by Reichl et al.[144] can be adapted to estimate the shape while increasing the accuracy. However, the use of this method in clinical scenarios still remains challenging, as the environments deal with ferromagnetic materials. Thus, the method [144] can be implemented for the shape reconstruction method and further investigation can be carried out to reduce the effect of environmental noise or an alternative method is required to identify from the literature to address the issue.

3.3.3   Stretchable sensor-based reconstruction methods

Currently, stretchable sensor-based shape reconstruction methods such as resistive and capacitive sensors are gaining popularity due to many advantages compared to other shape reconstruction methods. These sensors are defined as passive as they measure different properties by changing some passive electrical quantities such as resistance and capacitance. They generally show high stretchability as they are fabricated from elastomeric or other flexible materials. They are mainly adapted to soft actuators, where integrating FBG becomes difficult and time-consuming. Stretchable sensors are

furthermore a cost-effective solution. In this section, the different shape reconstruction processes using stretchable sensors are thus briefly described.

So et al. [145] proposed a method for reconstructing the shape of a soft manipulator used in MIS by implementing skin-type stretchable sensors made from multi-walled carbon nanotube and silicone. The sensor works on the principle of variable resistance, and the strain data from the sensor was utilized in the Frenet-Serret formula to reconstruct the shape (Figure 3.11(a)). When the reconstructed shape was compared with the camera data, it showed a tip position error of 8.9 mm which corresponds to 4.45% of the total length. In another work, Cianchetti et al. [146] presented a method that used stretch sensors to reconstruct the spatial configuration of an octopus-inspired robotic arm (Figure 3.11(b)). The stretch sensors work on the fundamental principle of resistance change and detect the local strain induced when deformations act on the arm. Data from the sensors were integrated into a dedicated model presented by Renda et al. [147] and used to determine the arms' curvature and shape. An error in the curvature evaluation was estimated, which varies between 3%-6% corresponding to 9-19 mm. In another novel approach, Wurdemann et al. [148] proposed a shape reconstruction process of a soft manipulator using shape sensors based on electro-conductive yarn (Figure 3.11(c)). Three sensors were embedded inside the soft silicon manipulator equipped with three pneumatic actuation chambers. The sensors worked on the principle of resistance change and were used to estimate the length of three chambers. The length information of these three chambers was utilized in dedicated equations to estimate the arc parameters of the manipulator. Abbas et al. [149] also presented another method that used a twisted and coiled sensor to estimate the shape of a soft robot. This sensor was made as a twisted and coiled shape configuration using silver-coated nylon sewing threads. The principle of operation of this sensor is based on the change of resistance of the twisted and coiled sensor. Initially, a physical-based model was presented to estimate both the force and displacement of the sensor using resistance values. Afterward, the sensor was embedded into a soft silicone robot to estimate the curvature. A resistive sensor based on low melting point alloy (LMPA) was

also used for reconstructing the shape of a variable stiffness manipulator intended to be used in MIS [150]. In this case, the LMPA was encapsulated into the microchannel of a silicone tube which was implemented with the manipulator. The change in resistance of the LMPA due to the change in its cross-section area helped to measure the length of the silicone tube which was further used to find the bending information of the manipulator. Recently, the use of capacitive sensors for shape sensing has also been proposed in the literature. Bilodeau et al. [151] presented a sensor-controlled antagonistic pneumatic actuator that employed a capacitance sensor fabricated using conductive fabric to reconstruct its curvature. When the actuator was controlled using the curvature information from the sensor, it produced an average error of 2.8 m^{-1}.
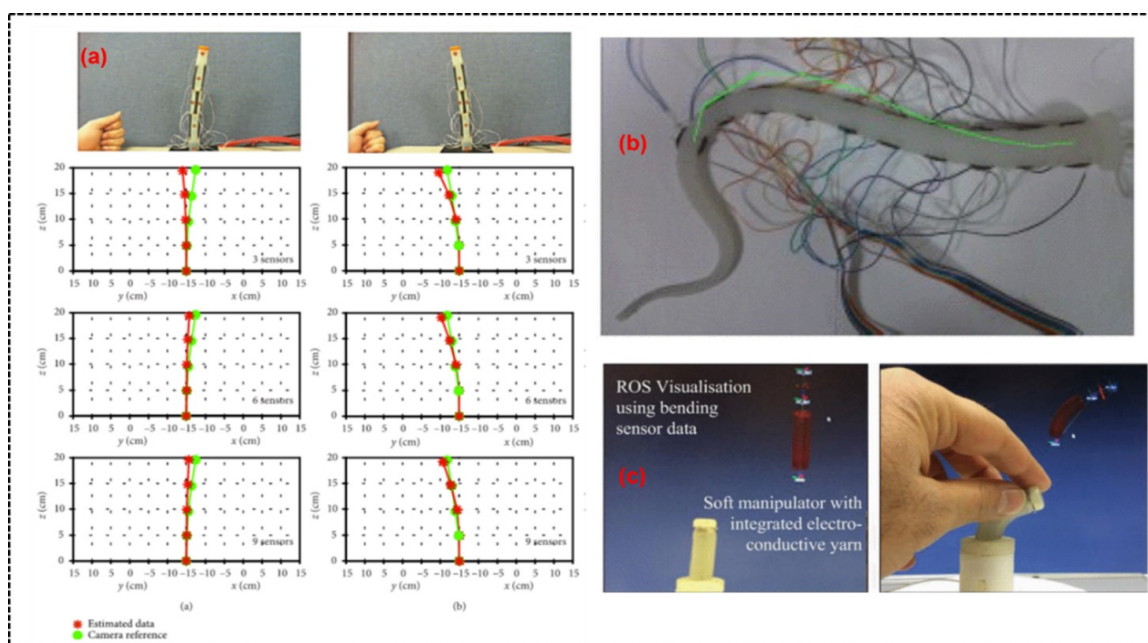
Figure 3.11: Shape reconstruction of soft manipulators using (a) skin stretchable resistive sensor (adapted from [145]); (b) conductive fabric (adapted from[146]); (c) using electro conductive yarn (adapted from [148]).

In addition to resistive and capacitive sensing, the use of inductive sensor in shape reconstruction process has been investigated by Jeon et al. [152] recently. In this regard, voice coil shape sensors were developed for reconstructing the shape of medical catheters. The sensors comprised excitation and sensor coils which were placed along the catheter's length. When an excitation signal was applied to the excitation coil, a voltage was induced in the sensor coil due to mutual inductance. This induced voltage was measured

to find the radius curvature of the catheter. The curvature information was used in a shape reconstruction algorithm based on a constant curvature assumption to estimate the shape of the catheter.

Altogether, stretchable sensor-based shape reconstruction methods show many benefits such as low cost, high stretchability, free from high radiation dosage and EM interference, and simple measuring equipment. Due to recent progress on skin type resistive sensors, they can be adopted into soft actuators used in MIS, avoiding complex sensor embedding processes. As they are intended to be made stretchable, they are already considered for reconstructing the shape of highly deformable soft actuators. From the literature, it is observed that shape reconstruction using resistive sensors is more suitable for soft robots and can be implemented on robots of different sizes [145, 146]. The current state of the arts [146, 145] show that the shape reconstruction error produced during these methods remains between 8 and 19 mm. Though they are featured by many advantages, the stretchable sensor-based methods show high shape reconstruction error when considering our required criteria.

No.	Criteria	Fluroscopy	Ultrasound	Endoscopy	FBG	Position	Stretchable
1	Stretchability to deal with the soft and flexible body	Yes	Yes	Yes	No	Yes	Yes
2	Safe in terms of less reduction of radiation and contrast agent	No	Yes	Yes	Yes	Yes	Yes
3	Accuracy should be as maximum as possible	Yes	Yes	Yes	Yes	Yes	No
4	Robust to invivo conditions	No	No	No	Yes	Yes	Yes

Table 3.1: Overview of requirement criteria

3.4   Synthesis

The state of the art conclusively shows that the shape reconstruction methods using intraoperative imaging such as fluoroscopy, ultrasound, and endoscopy are able to estimate the shape of flexible manipulators accurately and precisely without consuming extra space and with no hardware modification. Though these methods show many advantages, they have to deal with overuse of radiation dosage and low signal-to-noise ratio, or are unable to provide qualitative shape information in presence of occlusion and blood. As an alternative, sensor-based methods using FBG can be employed to address the issues produced by imaging methods while satisfying some of the required criteria. However, the issue of limited stretchability and high cost remains a concern. Due to the discrete placement of sensors in the case of position sensor-based reconstruction methods, the issue of stretchability can be resolved. Despite the satisfaction of many requirement criteria, it is still difficult to implement position-based methods in medical scenarios due to the issue of electromagnetic interference. On the other hand, stretchable sensor-based methods have the ability to fulfill all the required criteria, as they are free from radiation dosage, less susceptible to EM interference, highly stretchable, and low cost. The current shape reconstruction method like FBG shows difficulties if the robots experience twist while reconstructing the shape. This issue might also be addressed using stretchable shape reconstruction methods since they are stretchable. Table 3.1 shows all the sensing methods and their fulfillment according to required criteria. Based on Table 3.1, stretchable sensor methods show a lot of advantages and fulfill almost all the criteria required by the soft and flexible robot. However, these methods are still associated with high shape reconstruction errors. Thus, an investigation to find out and reduce the source of error is highly needed. This aspect is thus first explored in the case of resistive sensors which is one possible choice for stretchable sensors.

Chapter 4

Elastomer based Resistive Sensor

4.1 Introduction

The investigation to reduce shape-sensing errors started with the study of resistive sensors. The presence of hysteresis and non-linearities are identified as the primary sources of high reconstruction errors. Since these resistive sensors use elastomeric materials as a base substrate, thus there is a high possibility that non-linear and hysteresis behaviour arises from them [153, 154, 155]. Hence, the approach adopted here is to improve the performance of the resistive sensor while reducing the hysteresis and non-linearity. To achieve this, an attempt to fabricate a resistive sensor with low hysteresis and non-linearity is made by implementing two manual and industrial fabrication processes. A conclusion is then drawn from the assessment of prototypes.

4.2 Principle of operation of resistive sensor

Resistive sensors are generally fabricated using a base substrate and a conductive material. When the conductive material is used as a filler material, the base material becomes conductive and can be considered as a sensor. The sensor can take many forms, for instance, a conductive paste inside a cavity of the base material or mixing the base material with the conductive filler. For this kind of sensor, the geometrical properties have a correlation with the resistance. For example, the relationship between the electrical resistance and geometrical properties of a cylindrical-shaped resistive sensor is given as follows:

$$R = \rho \frac{L}{A} \tag{4.1}$$

Where R is the resistance of the sensor, ρ is the resistivity of the sensor material, L is the length, and A is the area of the cross-section of the sensors.
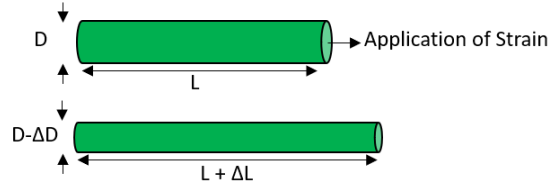
Figure 4.1: Application of the linear strain to a cylindrical resistive strain sensor

Figure 4.1 shows a cylindrical resistive strain sensor. When a linear strain is applied at the end of the sensor, the diameter D decreases to D-ΔD and length L increases to L+ΔL. These changes in properties increase the resistance of the sensor which can be calculated as follows:

$$\Delta R = R_{final} - R_{initial} = \rho \frac{L + \Delta L}{\frac{\Pi}{4}(D - \Delta D)^2} - \rho \frac{L}{\frac{\Pi}{4}(D^2)} \tag{4.2}$$

This change in resistance can be measured with a multimeter to get the applied strain.

4.3   Selection of the conductive material

Graphite powder is used as a conductive/filler material in literature [156, 157, 158] due to its high conductivity, excellent temperature resistance, chemical stability, and good thermal conductivity. Since the particles will be mixed with the base or other substrates for the fabrication of resistive sensors, it is better to select graphite particles with the least possible diameter for easy mixing. However, there are safety issues while handling smaller-diameter graphite particles. Considering this aspect, 20-micron diameter particles are selected.

4.4 Characterisation and selection of a base material

Elastomeric substrates have become the materials of choice due to their soft and lightweight characteristics, making them appealing when fabricating many stretchable sensors. They are the most suitable candidates for base substrates due to their large strain handling capability, good strength, and ease of fabrication. To fabricate precise and accurate strain sensors, critical issues related to hysteresis and non-linear behavior should be reduced as much as possible. In this chapter, three varieties of silicone rubber are chosen for this investigation. The data sheets of these commercial materials provide some of the mechanical properties, such as shore hardness, density, viscosity, etc., but lack any information about hysteresis and non-linearity properties. Hence, in this chapter, a base material is selected by estimating and comparing the hysteresis and non-linearity of the considered elastomeric materials.

Ecoflex rubbers (Smooth-On, USA) are a category of commercial silicone polymers with various shore hardness, and used in various applications [159, 160, 161]. Three kinds of Ecoflex are based on their shore hardness and represented as Ecoflex-0010, Ecoflex-0030, and Ecoflex-0050. These polymers have two components and can be cured at room temperature. The advantages of these materials are small shrinkage and short curing time. In this study, these three polymers are picked due to their easiness in fabrication, low cost, and ready availability for investigating various mechanical properties. All the details of these materials are given in Table 4.1.

Material (Ecoflex)	Viscosity (Pa·s)	Density (Kg/m^3)	Cure Time (hours)	Tensile Strength (MPa)	Elongation at Break (%)	Specific Volume (m^3/kg)	Shore Hardness
00-10	14	1040	4	0.83	800	0.00096	00-10
00-30	3	1070	4	1.38	900	0.00094	00-30
00-50	8	1070	3	2.17	980	0.00093	00-50

Table 4.1: Silicone rubber properties

4.4.1 Sample preparation of the based substrates

Ecoflex is a platinum-cured silicone rubber that is very easy to use in the fabrication process by simply mixing different parts at room temperature. The low viscosity allows easy and smooth mixing of different elements. To prepare the samples for investigation, a mold of 100 mm long and 10 mm wide is manufactured by using a 3D printer. In the beginning, two components of Ecoflex namely component A and component B are mixed together uniformly with a ratio of 1:1 at room temperature. After the mixing process, the prepared mixture is dispensed into the mold which is then kept inside a degasifier for 15 minutes to remove bubbles. Though the curing time remains between 3 to 4 hours for these materials based on manufacturer guidelines, the samples are kept for 24 hours in the horizontal position for proper curing. After the curing process, the sample is removed from the mold using a tool picker. The method for preparing the samples is shown in Figure 4.2.
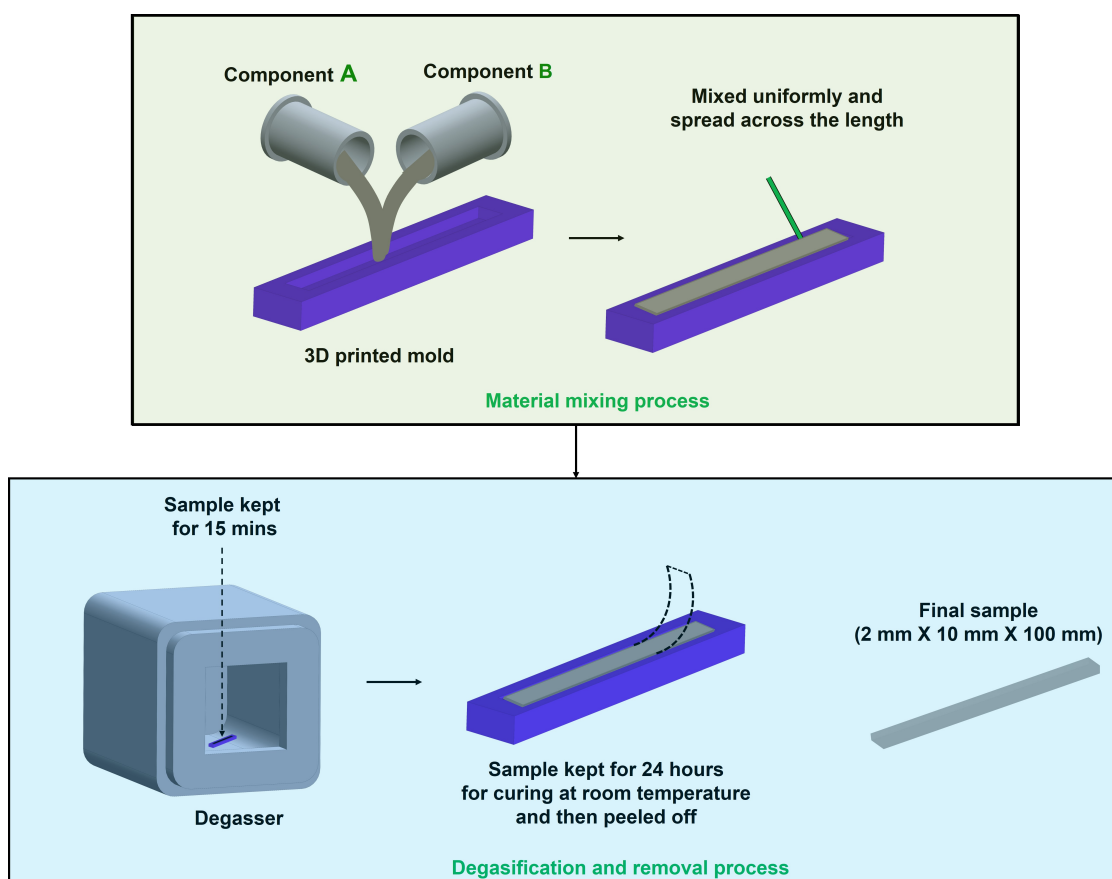
Figure 4.2: The process of sample preparation from Ecoflex polymers.

Three samples are prepared from Ecoflex-0010, 0030, and 0050 using the above process. The rectangular shape can be easily fabricated compared to cylindrical samples where molding and removal processes remain difficult. Hence, the shape of the sample is selected as rectangular with thickness, width, and length as 2 mm, 10 mm, and 100 mm, respectively. The samples are stored inside air and dustproof zip bags to avoid contamination.

4.4.2 Experimental setup and tests

The experimental investigation on the material hysteresis is performed using a testing setup comprising a robot arm and a fixture. The end effector of the robot arm is equipped with a load cell (Nano 17, ATI Industrial Automation, USA) which is capable of measuring force upto 17 N. The effector has a fixing mechanism that enables easy fixing of the sample into it. In addition to this, the robot is capable of moving vertically at different speeds with negligible misalignment and can be set according to speed requirements. However, there might be a small misalignment that is neglected during the test. To record data, a user interface developed in LabVIEW (National Instrument, USA) is used that allows to acquire both deformation and force data synchronously. The overall experimental setup for hysteresis evaluation is depicted in Figure 4.3.
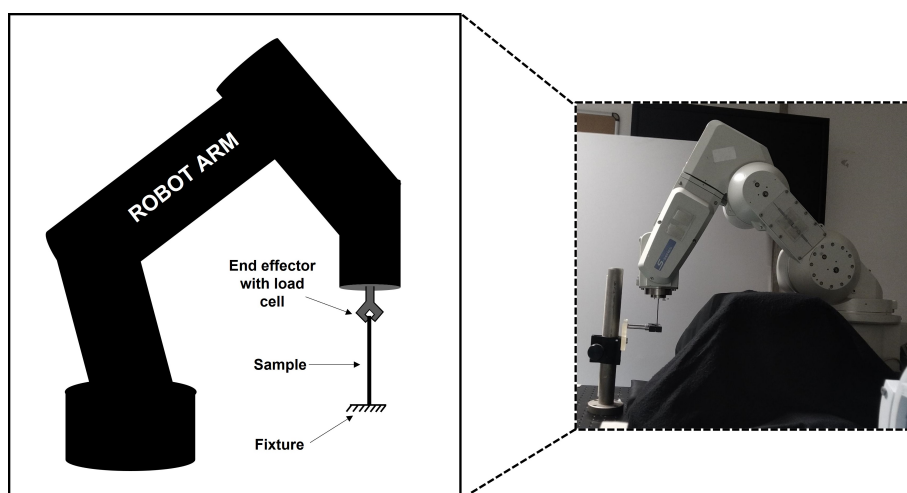
Figure 4.3: The robot arm applying the deformation to the sample connected between the arm and fixture

To characterize the material, the prepared sample is connected to the end effector

using the said mechanism at one end and the other end is connected to the fixture. Using this setup, a uniaxial tensile test is carried out that performs the loading and unloading of the sample. In this case, a strain of 10 % is applied with a strain rate of 0.1 mm/s to the sample using the robot arm. This experiment is repeated for a single cycle and multicycles (3 cycles) for each sample. Finally, the relationship between stress and strain is plotted. Figure 4.4a, 4.4b, and 4.4c show the hysteresis behaviour of Ecoflex-0010, 0030, and 0050 respectively.

The area enclosed by loading and unloading curves represents the energy loss during the cyclic operation and is defined as the hysteresis of the material. The amount of hysteresis can be estimated as follows:

$$Hysteresis = \frac{A_{Forward} - A_{Backward}}{A_{Forward}} \times 100 \tag{4.3}$$

where A is the area under the curve in the stress-strain characteristic, and the forward and backward indices are the loading and unloading phases, respectively. When the hysteresis for each sample is calculated using equation 4.3, it produced 11.2 %, 5.5 %, and 7.7 % for Ecoflex-0010, 0030, and 0050, respectively. Ecoflex-0030 shows less hysteresis in comparison with the other two samples. The decrease in hysteresis is not monotonous which might be due to the non-monotonous viscosity behaviour of these materials. When Young's moduli are compared, it is observed that Ecoflex-0010 and Ecoflex-0030 have almost the same Young modulus of 36 kPa while Ecoflex-0050 produces 71 kPa. Since the sensors will be embedded inside robots, thus materials with a small Young modulus are generally preferred as they require less force during stretching.

Next, the non-linear behaviour of these materials is estimated by fitting a linear curve to the data and then calculating the maximum deviation between the actual curve and the fitted linear curve. The estimated non-linearity values of Ecoflex-0010, 0030, and 0050 are 11.06%, 10.17%, and 12.65%, respectively. Compared to Ecoflex-0010 and 0050, the Ecoflex-0030 shows less non-linearity. In conclusion, Ecoflex-0030 is selected as the base material for the sensor development due to its least hysteresis, non-linearities, and Young's modulus.
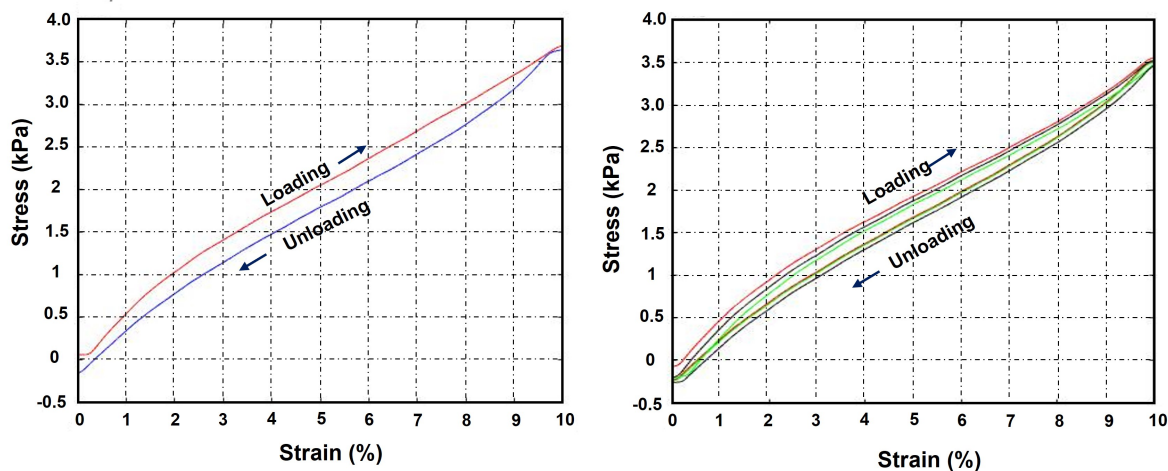
(a) Hysteresis curve of Ecoflex-0010 for a cycle (Left) and multiple cycles (Right).
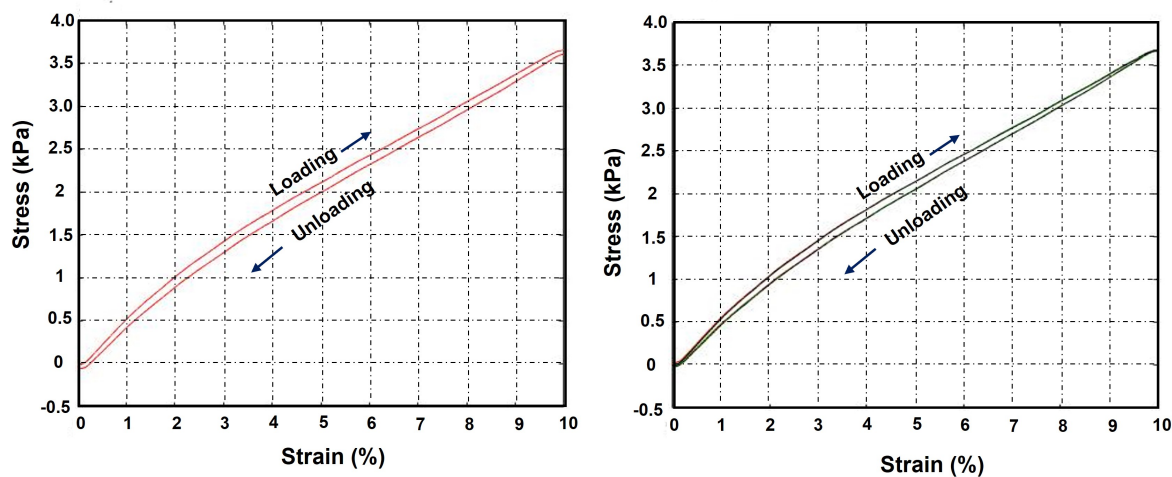
(b) Hysteresis curve of Ecoflex-0030 for a cycle (Left) and multiple cycles (Right).
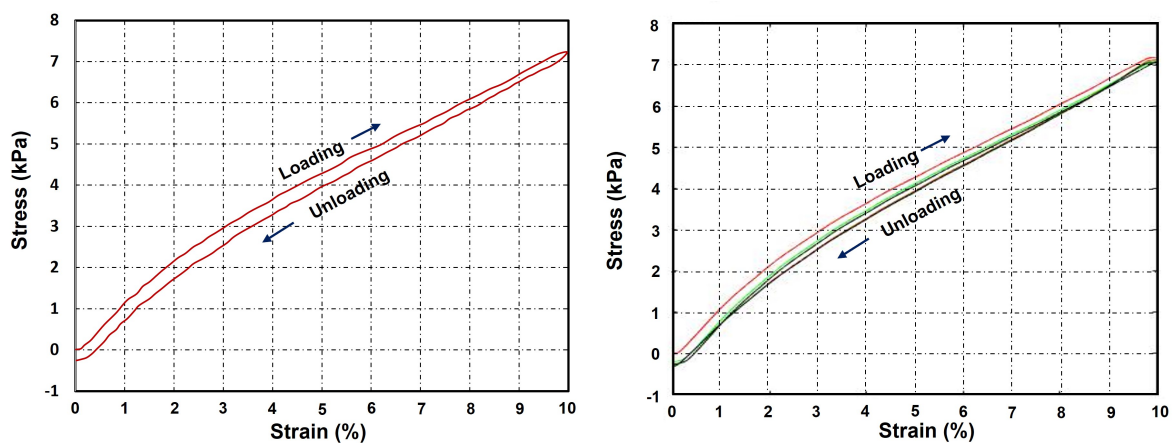
(c) Hysteresis curve of Ecoflex-0050 for a cycle (Left) and multiple cycles (Right).

Figure 4.4: Characterisation of base materials

4.5 Sensor fabrication using Ecoflex and graphite

4.5.1 Strain sensor using conductive paste inside a tube

As an initial attempt, a cylindrical resistive strain sensor is fabricated using a conductive paste and a silicone tube prepared using Ecoflex-0030. This process is easy to implement as compared to the direct mixing of graphite with Ecoflex which requires many steps. Thus, this method is implemented by making a 3D-printed mold of a hollow cylinder shape. The same procedure is followed as given in Figure 4.2 where the prepared Ecoflex mixture is poured into the mold to fabricate the silicone tube. Only carbon powder can be used as the filler material inside the hollow space of the tube to conduct electricity. However, this process may cause high fluctuations in measurements since the carbon particles are free inside the tube. Thus, to tackle this problem, a water-based conductive paste is prepared by mixing graphite powder, sodium chloride, and water together in a ratio of 75%:5%:20%. Sodium chloride is added to increase the impurity of the water, thereby increasing the conductivity. Then, the paste is slowly injected inside the silicone tube and both ends are sealed using silicone glue (Silpoxy, Smooth-on, USA). The design and fabrication are shown in Figure 4.5.

The resistance of the sensor is measured using an electronic multimeter and the measured resistance fluctuates between 131 kΩ to 152 kΩ at rest. The cause of the variation might be due to the bonding issue between the conductive particles of the paste inside the tube or a loose connection between the electrical leads with the conductive paste. Since the connection is between a solid lead and viscous liquid paste, the issue of loose connection cannot be solved easily.

The fabricated sensor shows ease of fabrication, simplicity, and low cost. However, the significant variation in the resistance creates a challenge in the data acquisition process which needs a possible modification such as mixing graphite powder with the silicone material directly to fabricate a stable strain sensor. A direct mixing technique may address the bonding issue of the previously developed sensor. Moreover, the issue of loose connection may be solved with the direct mixing procedure, as the lead will tightly hold the sensor due to the curing process.
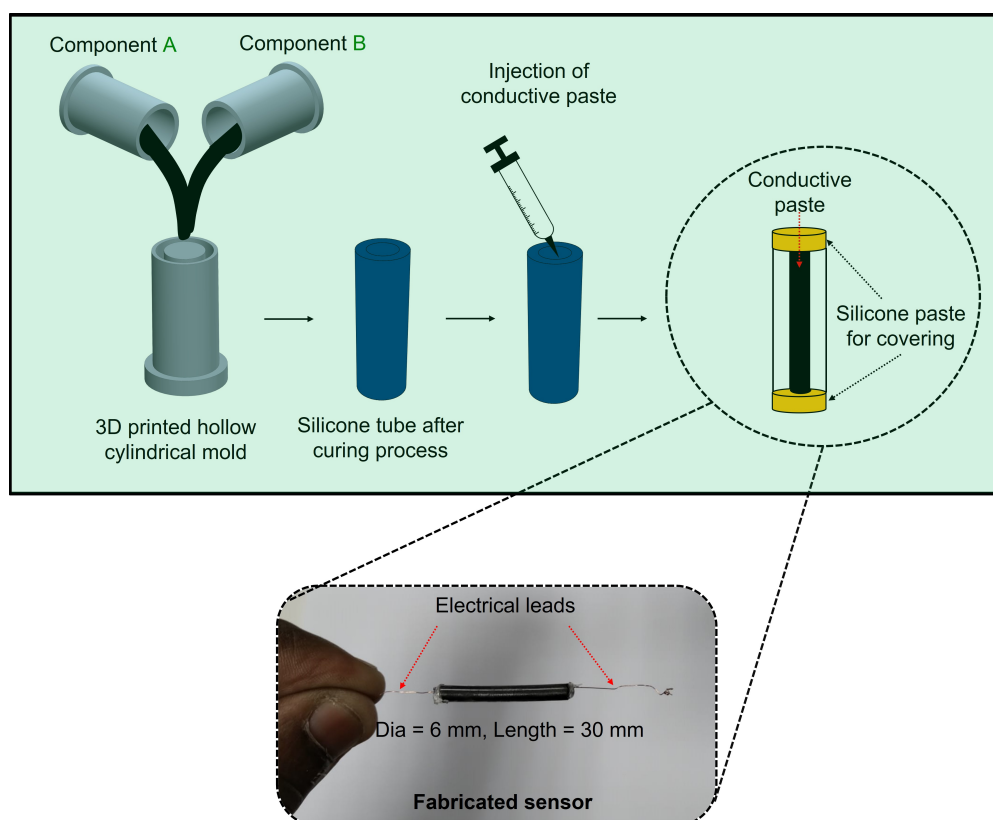
Figure 4.5: Strain sensor fabrication process using conductive paste inside the silicone tube

4.5.2 Strain sensor based on direct mixing

In the next step, a strain sensor based on the direct mixing of graphite powder and Ecoflex-0030 is proposed. The direct mixing process helps the Ecoflex and graphite particles to form bonds between them which might reduce the problem of instability in the measurements. To prepare the sample, the procedure given in Figure 4.2 is followed where initially both components of Ecoflex-0030 are mixed followed by a graphite powder mixing process with a weight ratio of 49:49:2. As the stiffness of the sensor increases with the carbon content, the primary focus in this process is to produce a sensor with the minimum amount of carbon content. Here, the amount of graphite powder is continuously injected into the Ecoflex mixture and stirred until the total mixture becomes conductive. The conductivity is continuously checked with the multimeter. When the graphite powder amount is increased, the quantity of Ecoflex mixture is adjusted accordingly to maintain weight balance. It is observed that the mixture becomes conductive when the weight percentage of graphite reaches 33%. Then, the prepared mixture is poured into a 3D-

printed mold and left for 1 day at room temperature for curing. Two electrical copper wires are introduced into the mixture which serve as electrical connections. The resistance of the final cured sensor at 33% of carbon is 210 kΩ and can be measured using an electronic multimeter.
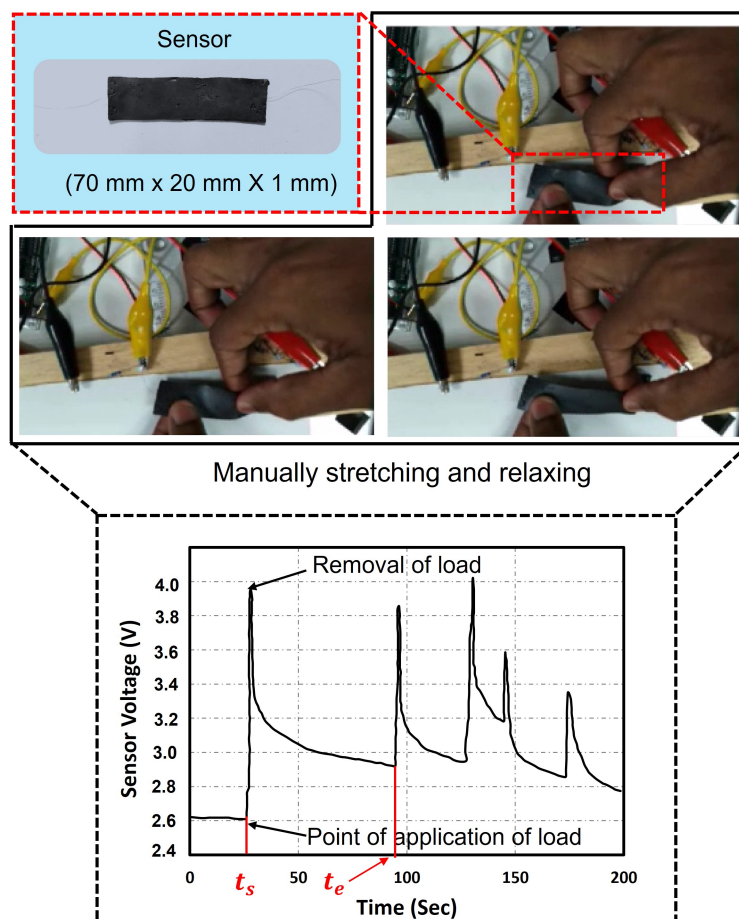
Figure 4.6: Application of the manual strain to the sensor (Top); the response of the sensor to the manual strain (Bottom)

The voltage across the sensor is measured with an experimental setup prepared from an Arduino microcontroller, a voltage divider circuit, and a PC. This setup is able to measure and acquire the information from the sensor with respect to time and is suitable for measuring the resistance change up to 0.5 Ω. In this setup, the sensor is connected to the microcontroller and a known resistor (220 kΩ), thereby creating a voltage divider circuit. The microcontroller is then connected to the PC. A hardware and software interface is made using MATLAB which is further used for the voltage measurement process. The response is checked while a linear deformation is applied manually by hand

by stretching and relaxing the sensor. The voltage change of the sensor is recorded in MATLAB which shows a relationship between the voltage across the sensor and time.

It can be observed from a specific period in Figure 4.6 (t_s to t_e) that the sensor responds to the load in about 0.5 sec. However, the sensor is unable to reach a steady state even after waiting for a minute. In addition to this, the sensor relaxation process is very slow. These issues might be due to the viscous behaviour introduced while mixing the Ecoflex and graphite powder or due to improper mixing that might create an improper conducting path. The improper conducting path might be due to the use of a catalyst during the curing process that creates the issue. Thus, the process needs to be changed to make a uniform mixture that may create the shortest conducting path and also may reduce the viscous effect produced due to manual mixing.

4.5.3 Commercial conductive rubber

The investigation of the above-fabricated sensors shows that they are not able to achieve the required performance. Since these sensors are fabricated using manual processes, it is still early to make a final decision that resistive sensors are not useful for an accurate shape reconstruction process. As a final step of the investigation, a commercial conductive rubber is considered. The commercial conductive rubber is purchased from ADAFRUIT (Product ID: 519, USA). As this material is developed using an industrial uniform mixing procedure, it may address some issues of previously developed resistive sensors that use a manual fabrication process. The conductive rubber behaves as a resistive sensor that is 2 mm in diameter, cylindrical in shape, and made of carbon-black impregnated in rubber. The resistance of the sensor in the relaxed state is 140-160 Ohm/cm and it shows good conductivity, high elasticity (Young's Modulus E = 0.011GPa), and low cost (9.95 Eur/meter). However, the technical data about mechanical and electrical behaviors which are very important in sensor applications are not provided.

Mechanical hysteresis investigation

In order to estimate the mechanical hysteresis, a prototype of 30 mm in length is used. The commercial rubber is connected to a universal testing machine (Instron, Model-4464,

Italy) using two fixtures. The sample is subjected to a 20% strain for one cycle as well as three cycles to simulate multiple loading and unloading conditions. Since the conductive rubber will be considered to be used in flexible robots operating at different strain rates, mechanical hysteresis behaviour for different rates is estimated by applying 10 mm/min, 30 mm/min, 50 mm/min, 100 mm/min, and 200 mm/min strain rates respectively. Next, the force and strain data acquired from the measurement setup are used to estimate the hysteresis. The mechanical hysteresis curve for the sensor is given in Figure 4.7. In three-cycle experiments (Figure 4.7) at different strain rates, mean hysteresis is found as 21%. The mechanical hysteresis remains high for this material, however, they are repetitive in nature for multiple cycles as well as for different strain rates.
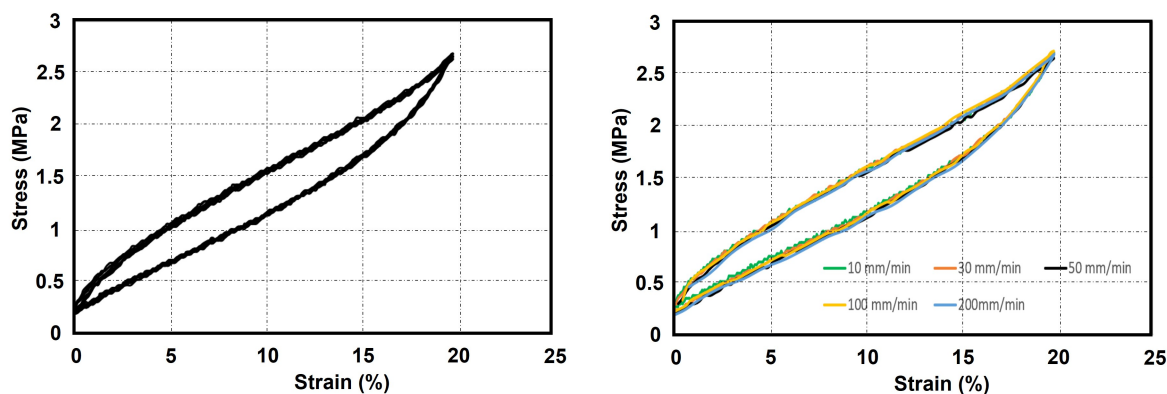
Figure 4.7: Mechanical hysteresis loop of the sensor for 3 cycles (Left) and mechanical hysteresis at various strains (Right)

Electrical hysteresis investigation

A custom testbed is used for electrical characterization consisting of a linear stage and a measurement setup. The measurement setup comprised a DAQ system (NI USB-6259) and an electronic circuit that has the sensor, a 150 Ω resistor, and a DC voltage source. 20% tensile strain, for one cycle and ten cycles, is applied to the sensor using the linear stage. The voltage across the sensor is measured using the DAQ system while the sensor is connected to the DC voltage source and 150 Ω resistor in series, thereby creating a voltage divider circuit. The voltage and strain data acquired are used for determining electrical hysteresis. The electrical hysteresis measurement setup and the hysteresis plots are given in Figure 4.8.
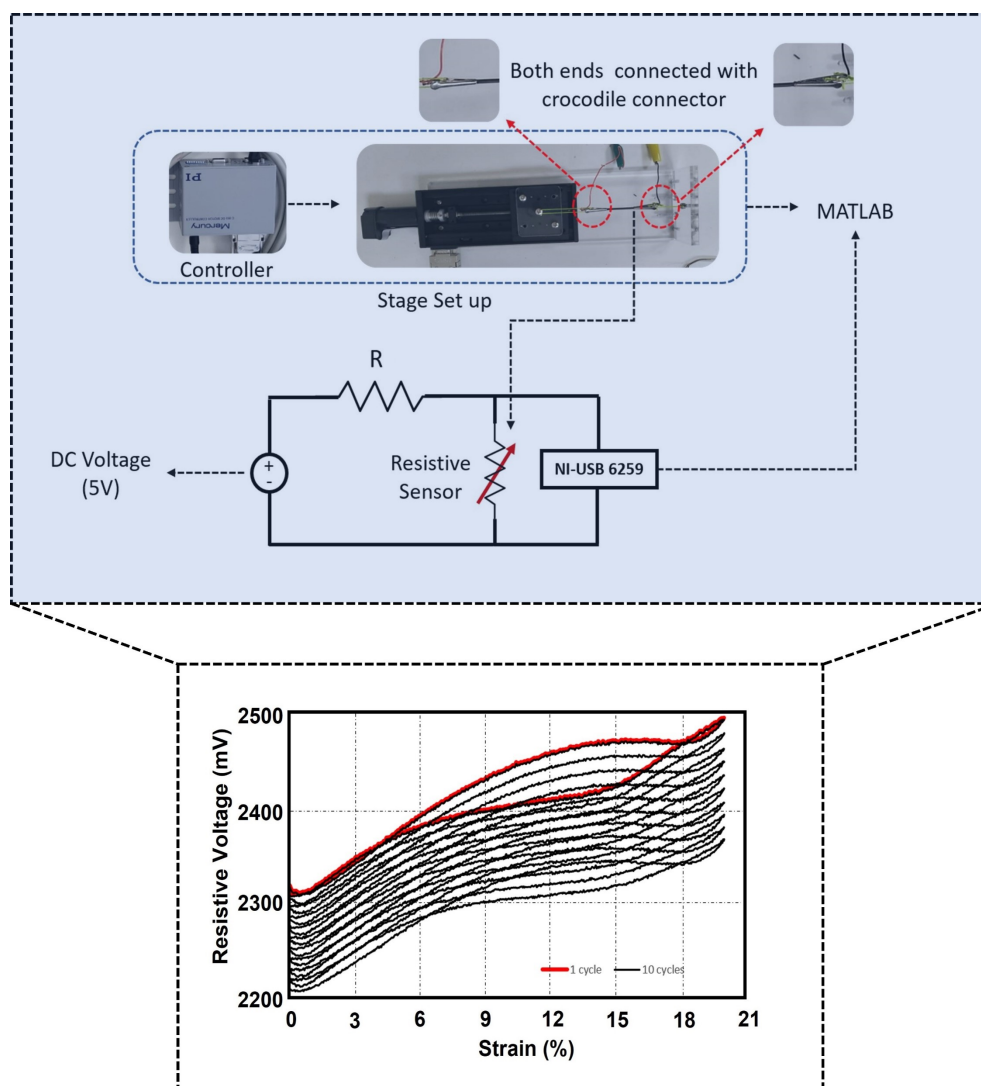
Figure 4.8: Electrical hysteresis measurement set up (Top) and electrical hysteresis for 10 cycles (Bottom)

The electrical hysteresis behavior of the sensor for single and multiple cycles can be seen in Figure 4.8 (Bottom). The sensor produces 7.8% of voltage change for 20% deformation of its length. It can be observed, in successive loading cycles, the resistive voltage across the sensor reduces due to the presence of electrical hysteresis and delay in restoration of the original material behavior of the sensor after each cycle. The sensor takes almost 10 sec to come to the initial position.

4.5.4   Discussion

The state of the art shows that resistive strain sensors are capable of estimating the shape while satisfying the large deformation requirement, ease of fabrication, and low

cost. However, as discussed the hysteresis issue remains a major concern that increases the shape reconstruction error. In this case, an attempt has been made to fabricate a stretchable strain sensor based on the variable resistive principle with an aim to reduce hysteresis and non-linearity. This started with investigating the base elastomeric material and finally selecting the materials showing less amount of hysteresis and non-linearity. The selected base material along with conductive powder is used to fabricate the sensor. Two different prototypes are prepared using two various manual fabrication processes. They are able to successfully conduct electricity and are capable of providing data to the system. However, these samples are unable to pass the first stage of testing in which they show instability and time delay in the measurement process. This issue is probably due to the manual fabrication process that produces a nonuniform mixture. To address the issue of the manual fabrication process, a commercial conductive rubber is considered to be used as a strain sensor as an alternative. As these rubbers are prepared using industrial procedures, they might solve the previous issue. The characterization of the commercial conductive rubber shows that the hysteresis issue still couldn't be resolved. All in all, both manual and commercial fabricated resistive sensors are investigated. Both of them are compared based on their repeatability, hysteresis, and relaxation time. In terms of hysteresis, the commercial sensor shows large hysteresis. But, its relaxation time is better than manually fabricated sensors. Despite the better relaxation time shown by the commercial one, its hysteresis still creates problems for accurate strain estimation. According to the state-of-the-art [162, 163], the filler materials such as carbon nanotube and silver nanoparticles have the capability to drastically reduce the hysteresis amount. However, these particles show issues of safety and bio-compatibility. They might be addressed using advanced techniques during the fabrication of the sensors. In the literature, two other methods based on inductive and capacitive sensors have also been identified which are capable of reconstructing the shape of soft and flexible robots. Hence, it is preferred here to explore their use in the following chapter.

Chapter 5

Development of an Inductive Flexible Sensor

5.1   Introduction

Owing to its good accuracy, inductive sensing has been used in the shape reconstruction process which is already discussed in Chapter 2. Since most inductive sensors don't involve any conductive particles and elastomeric materials, they address the issue of high hysteresis of resistive sensors. In addition to this, inductive sensors also possess good stretchability, excellent signal repeatability, and ease of fabrication. In this chapter, the use of an inductive sensing principle is therefore investigated for shape sensing in soft and flexible robots.

Planar coil and skin-mounted inductive sensors [164, 165, 166] are proposed in the literature to detect different properties, such as bending angle, proximity, and force. Hamaguchi et al. [164] presented an inductive tactile sensor with just two liquid-metal reservoirs (contact and reservoir) coupled by an extended flow channel and coil in a silicone-rubber body. The sensor estimated the applied normal force by monitoring the movement of the liquid metal in the detection reservoir. Increasing the volume of liquid metal over the coil in the proposed sensor lowers the coil inductance by increasing the eddy current in the liquid metal. Monitoring the change in coil inductance was therefore used to quantify the applied force. As a demonstration of this sensor, it was attached to the skin of a pneumatic artificial muscle and inductance change during bending and touch was demonstrated (Figure 5.1(a)).

In [165], Raj et al. proposed a flexible inductive coil-based sensor by embedding steel wires in a silicone material (Figure 5.1(b)). The sensor was made up of two planar coil inductors that were stacked one on top of the other in a transformer-like configuration. The mutual inductance between the two coils was the system's basic functioning mechanism for strain estimation. The coupling between the two coils, which varied as the dual-coil system bends, determined the voltage output. The coils were arranged in an anti-phase pattern such that as they bend, the coupling increases and the voltage output rises. The sensor was successfully implemented to measure the bending of a hand.

Fassler et al. [166] introduced a soft inductance sensor that was produced by embedding silicone elastomer with microchannels of galinstan, a metal alloy that is liquid at room temperature. The applied strain caused an inductance change due to an increase in the length and decrease in the diameter of the microchannel which was measured using an LCR meter.

Since the group of inductive sensors presented above are capable of providing high stretchability (100%) [166] while producing minimal hysteresis [165], they are implemented in flexible and soft devices by attaching them onto the skin. These sensors are useful for proximity and tactile information. They are also used for measuring bending as well as linear strain due to their stretchability. However, for the class of medical robots or systems such as catheters, endoscopes, and continuum robots, the compactness of the sensor needs to be considered during integration. Additionally, attaching the sensors to the outer surface will increase the overall diameter. Thus, planar coils or skin-mounted inductive sensors might not be effective in such a scenario. As a result, solenoid-type inductance strain sensors are considered several times in the literature.

Felt et al. [167] presented a smart pneumatic actuator. The smart actuator was fabricated by enclosing a pneumatic chamber with a Braided sheath (Figure 5.1(c)). In this case, the non-conductive fibers of the sheath were replaced with conductive wires. These wires form a solenoid-like circuit with an inductance that more than doubles over

the actuator contraction. The contraction was calculated using an LCR meter to measure the smart actuator's inductance. The average inaccuracy in the smart actuator's position was estimated as 1 mm.

The lateral displacement of a bellows-driven continuum joint in soft robots (Figure 5.1(d)) was estimated by the same group [168]. Coils of wire wrapped around the minor diameters of each bellow on the joint served as the sensing system. The distance between the wire coils increases as the bellows lengthen, reducing their mutual inductance. Measuring this change in mutual inductance allowed for measuring the motion of the joint. Both of the methods presented by this group can sense bending and elongation without requiring any additional sensing elements, as the wires used for the actuation can be utilized as the sensor.

The use of hollow coils in conjunction with an LCR meter unit to measure the bending angle of a soft actuator was shown in [169]. The actuator was powered by three air chambers, each of which was encircled by a spring-like sensor that may restrict the radial expansion of the actuator (Figure 5.1(e)). When the chamber was pressurized by air or hydrostatic pressure to increase the length, the inductance of these sensors increased. The bending angle was estimated by measuring the inductance with the LCR meter.

Azami et al. [170] proposed a soft actuator using a silicone tube and a metal coil spring reinforcing the outer periphery (Figure 5.1(f)). The metal spring in the proposed actuator worked as a displacement sensor by measuring the inductance of the spring, while it restricted the movement of the actuator to the linear motion like a conventional fiber-reinforced actuator. A Pierce Oscillation Circuit was implemented to observe the inductance of spring by the means of oscillation frequency. This proposed method showed ease in the sensor integration process while producing 0.5 mm inaccuracy in the strain measurement process.

In the case of a rehabilitation application, a soft solenoidal inductive (Figure 5.1(g)) sensor was incorporated into wearable devices by measuring the induced electromagnetic field [171]. In a different approach, Choi et al. [172] proposed a soft inductive sensor for measuring the linear displacement of a robotic arm using shape memory alloy springs.

Due to antagonistic placement, they produced a differential analog voltage between the springs during movement which was measured using a custom circuit to estimate the displacement (Figure 5.1(h)).
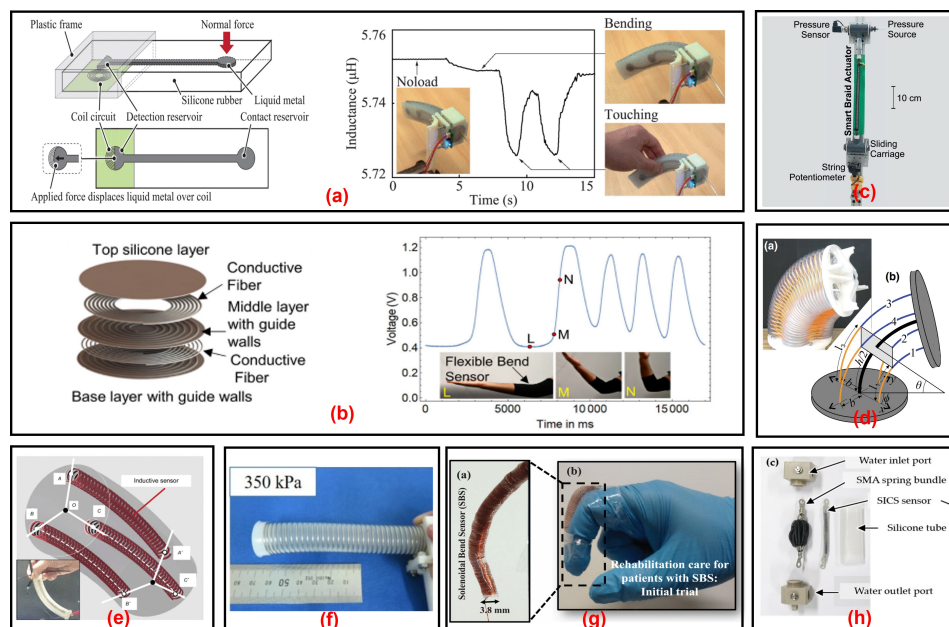
Figure 5.1: (a) Structure and working principle of the tactile sensor and its integration into a soft robot [164]; (b) flexible fiber inductive coil sensor [165]; (c) an inductance sensor estimating the contraction of a smart braid actuator [167]; (d) lateral displacement measurement of a bellows-driven continuum joint [168]; (e) a prototype of a soft manipulator and the three fiber reinforcements as three inductance sensors [169]; (f) a prototype of a soft manipulator with spring as an inductance sensor in soft robots [170]; (g) a soft solenoidal bend sensor with flexible coil embedded in polymer [171]; (h) a soft inductive coil spring sensor-integrated in shape memory alloy spring bundle actuator [172]

From the literature, it is concluded that the solenoid-based inductive sensors are thus showing high potential in the strain measurement process. Since they are capable of producing ultra-low hysteresis [169], inaccuracy less than 2 mm [170, 167], and stretchability up to 100 % [169], solenoid-based inductance sensors can be a solution for the shape reconstruction process. Three things, i.e, simple measuring equipment, versatility, and in-depth characterization, are important to investigate during the use of an inductive sensor. During the exploration of the state of the art, we observe that specific instrumentation is generally needed. For instance, in some cases, an expensive [167] and highly precise LCR meter (0.001 μ H resolution [169]) is required for measuring the inductance change. These types of measuring equipment are device and

sensor-specific which might create constraints in terms of instrumentation. Additionally, the versatility of inductive sensing when different modes of deformation are encountered by a sensor is not discussed. Typically, an actuator in bending or extension alone is considered for a given sensor. Therefore, it is critical to determine whether the same sensor can be integrated into both bending and linear deforming robots without increasing the overall complexity and calibration process. In the literature, different authors investigate specific properties of the sensor based on the requirements. However, in-depth characterization of the coil-based sensor is needed considering its implementation into various soft and flexible robots. As a result, we propose in this chapter: (i) a method to measure the strain using a simple voltage measurement instead of performing a direct measurement of inductance. This voltage measurement technique helps to optimize the measurement conditions that certainly increases the performance of the sensor. The versatility of the sensor for its implementation for the bending and elongation strain estimation process has been experimentally verified. (ii) Additionally, a full characterization process for the sensor is conducted to elaborate on its hysteresis, stretchability, repeatability, strain rate response, precision, and accuracy. (iii) Ultimately, the feasibility of the sensor integration process is verified by implementing the sensor and testing the added value of proprioception into soft and flexible robots.

5.2   Analysis and optimization of the inductive sensor

5.2.1   Modeling and optimization of the strain sensing principle

The strain sensing we consider is based on the principle of variable electrical inductance. The sensing element is a conductive coil spring of length l, diameter D built from n turns of a wire. It can be modeled (Figure 5.2) as an inductor (L) with a parasitic capacitance C. We consider an arrangement where the coil spring is connected to a resistor R in series with an AC voltage source of amplitude V_i and frequency ω. In this case, a direct measurement of voltage is performed instead of inductance. Neglecting the internal resistance of the spring, the voltage across the inductor (V_o) can be derived in a simple way:
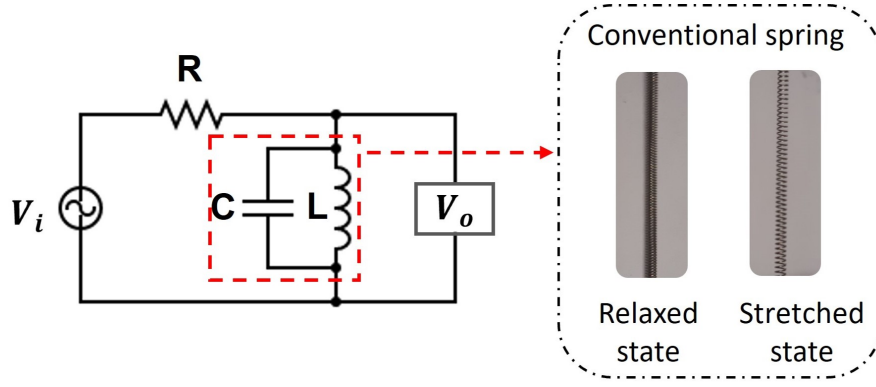
Figure 5.2: Modelling of the electrical circuit

$$V_o = \frac{Z_{LC}}{Z_{LC} + R} \times V_i \tag{5.1}$$

where Z_{LC} is the total impedance of the inductor that can be derived as follows:

$$Z_{LC} = \frac{X_L * X_C}{X_C + X_L} = \frac{j\omega L * \frac{1}{j\omega C}}{j\omega L + \frac{1}{j\omega C}} = \frac{j\omega L}{1 - \omega^2 LC} \tag{5.2}$$

Substituting in equation 4.1 and simplifying results:

$$V_o = \frac{j\omega L}{R(1 - \omega^2 LC) + j\omega L} \times V_i \tag{5.3}$$

The inductance of the spring is linked to the area (A), length, and permeability of free space (μ_o) which is given as follows:

$$L = \frac{\mu_o n^2 A}{l} \tag{5.4}$$

The gain (G) of the circuit can be given as:

$$G = \frac{u}{\sqrt{(l - m)^2 + (u)^2}} \tag{5.5}$$

Where

$$G = |V_o/V_i| \tag{5.6}$$

$$m = \omega^2 \mu_o n^2 AC \tag{5.7}$$

$$u = \omega \mu_o n^2 A/R \tag{5.8}$$

Both m and u depend on the physical properties of the sensor such as μ_o, A, and C, which are considered to be constant, and that of the electric circuit ω and R, which are

also constant during measurements. Once the values of m and u are determined, it is then possible to estimate the spring length from the gain. That means it is feasible to use simple voltage measurements to get the strain information.

The parasitic capacitance C is typically very small, with an order of magnitude of $10^{-12}F$ [173, 174]. We therefore consider that m is several orders of magnitude smaller than l which means *(l-m)* is always positive. As such, G is monotonically decreasing when the spring length increases.

Two criteria are of particular importance when characterising the sensing performance. The first one is obviously the derived gain value G. The second one is the sensitivity S, which can be computed as the derivative of the gain G with respect to the sensor length:

$$S = \frac{\partial G}{\partial l} = \frac{\partial}{\partial l}\left(\frac{u}{\sqrt{(l-m)^2 + (u)^2}}\right) = -\frac{u(l-m)}{((l-m)^2 + u^2)^{1.5}} \tag{5.9}$$

Achieving a direct measurement of the voltage instead of the inductance makes it possible to adjust the measuring conditions to optimize the sensing performance. The value of the resistance R and the frequency of the AC input ω constitute two adjustable parameters for satisfying gain and sensitivity values simultaneously. In addition to simplicity in measurement, we have the capacity to adapt measurement conditions to improve sensor performance.

Equation (4.5) shows that the gain approaches 1 when u tends to infinity. This is only possible when ω becomes as big as possible and R is as small as possible. However, from equation (4.9), it can be observed that the sensitivity of the circuit approaches 0 when ω tends to infinite. Thus, setting the right measurement is not straightforward. The contradictory influence on gain and sensitivity makes it necessary a method for the optimization of measurement conditions. In this case, a numerical approach is followed to find the optimal frequency for maximum sensitivity. To validate the numerical approach, an experimental-based method is also followed to measure the optimal frequency. For the numerical approach, We propose a 2-step procedure.

In the first step, the resistance value is selected. Reducing the resistance to a small value will indeed increase the gain but it may increase the amount of current drawn and

induce unwanted heating effects. Setting a high value for the resistance will decrease the gain, thereby limiting the effectiveness of the strain measurement process. Therefore, we suggest setting the resistance to a "middle point" value (chosen qualitatively) by considering the above aspects. This will be illustrated in the next section. The selected value needs to be verified afterward, at the end of the second step.

In the second step, the selection of frequency is formulated as an optimization problem. The optimal frequency f^* is defined by:

$$\omega^* = 2\pi f^* = \arg\max_{\omega \in R} S(w) \tag{5.10}$$

Where ω is the angular frequency. Once f^* is computed, the gain value is checked based on suitability for the measurement, and steps 1 and 2 will be repeated if needed.

Table 5.1: Spring specifications (Approx. Values)

Properties	Spring 1	Spring 2
Length of the spring (l) [mm]	100	100
Diameter of the spring (D) [mm]	1.15	0.85
Wire diameter of spring (d) [mm]	0.1	0.1
Number of turns (n)	650	680
Parasitic capacitance (C) [pF]	1.38	1.14
Theoretical optimum frequency [MHz]	4.5	7.2
Spring constant (mN/mm)	6.5	6.1

5.2.2 Application of the optimization method

As an illustration, we consider two springs whose properties are given in Table 5.1. The method is initially implemented in spring 1. Using the considerations presented above, the resistance value is set to 220 Ω. Then, the optimal frequency is computed using the properties listed in Table 1 and equation 4.10. As a result, the optimal frequency reaches 4.5 MHz when the frequency is swept from 1 kHz to 25 MHz.

For verifying and illustrating the influence of the measurement conditions, all the parameters are also substituted in Equation (4.9) to get the relationship between the sensitivity, frequency, and length of the sensor. Next, the sensitivity is observed by varying the frequency from 1 kHz to 25 MHz and the length from 0.1 m to 0.2 m. Figure 5.3 shows the relationship between the sensitivity, frequency, and length of the sensor.

In this figure, the X-axis and Y-axis show the circuit frequency and length of the sensor respectively, while the Z-axis shows the sensitivity of the sensor. It can be observed that the sensitivity follows a saddle trend, i.e., the sensitivity increases up to a certain frequency and then decreases afterward. The point where the sensitivity of the sensor becomes maximum can be found as 4.5 MHz.
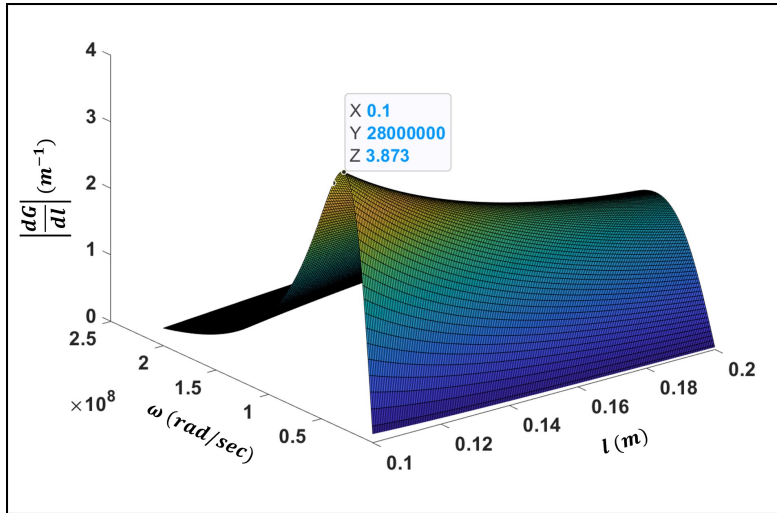
Figure 5.3: Theoretical relationship between sensitivity w.r.t. input frequency and length

In order to visualize the coupled impact of the frequency and resistance, the same procedure is followed and the evolution of gain and sensitivity is computed by varying the circuit resistance from 20 Ω to 1000 Ω. The gain and maximum sensitivity of the sensor are plotted as functions of the resistance in Figure 5.4. The sensitivity varies only slightly, with a 14% evolution. The resistance value is then not critical, and the selected value is seen as suitable. However, setting the circuit resistance to a higher value will reduce the gain, making the strain measurement process less effective. From the plot between the frequency at which maximum sensitivity occurs with respect to resistance (Figure 5.5), it should be noted that the optimal frequency f^* increases by increasing the resistance. For instance, the frequency reaches 21 MHz when the resistance value is 1 KΩ. In terms of instrumentation, this adds constraint to having an adequate sampling rate and measurement accuracy at high frequencies. This may also require a high-end input supply for generating high frequency signal. Moreover, the gain also reduces drastically at higher resistance.
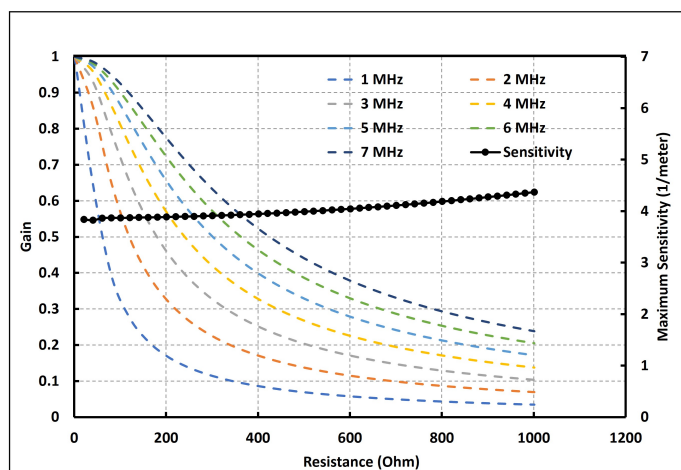
Figure 5.4: Relationship between the circuit gain G and maximum sensitivity of sensor w.r.t circuit resistance R
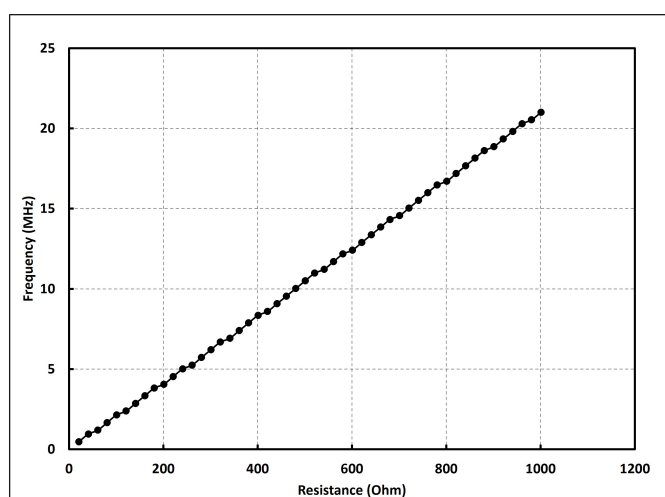
Figure 5.5: Relationship between input frequency f^* for maximum sensitivity w.r.t circuit resistance R

As a complementary step, beyond the proposed method for set-up selection (Figure 5.6), we investigate the frequency for maximum sensitivity experimentally. Spring 1 is connected to a 220 Ω resistor and a 5 V peak-to-peak (P-P) signal is applied using an AC sinusoidal voltage source, i.e, a function generator (33220A, Agilent Technologies, USA). The voltage in the inductor is measured using an oscilloscope (MSO7034B, Agilent Technologies, USA). A linear motorized stage setup (PI, USA) is used to apply linear strain to the spring. All the acquisitions are synchronized using LabVIEW (NI, USA). Spring 1 is connected to the setup as shown in Figure 5.6. In this case, the length of the spring is chosen as 130 mm, out of which 100 mm acts as the active or principal

sensing length and the leftover length is divided into two parts i.e., left and right end. As throughout the experiments, the left end will be considered to remain stationary, thus, 10 mm of the leftover length of the coil-shaped spring is converted to straight configuration to make it as left end electrical lead and the rest of 20 mm is used to prepare the right end electrical lead. To calculate the relationship between sensitivity and frequency experimentally, the spring is connected to the stage setup where the left end of the spring is firmly fixed to the stationary part and the right end is fixed to the movable carriage of the setup using plexiglass plates and nuts. Next, the spring is elongated up to 40 % strain with a rate of 1 mm/s, and the relation between the gain (G) of the sensor and strain data is determined using the data acquired from the experimental setup. Then, this step is repeated by varying the input frequency from 0.5 MHz to 16 MHz. Finally, the sensitivity of the sensor is estimated by calculating the slope of each curve and plotted against varying frequencies. Figure 5.7 shows the comparison between the experimental and theoretical evolution of the sensitivity-frequency relationship for spring 1. Results are consistent in terms of sensitivity variation, even if the maximum sensitivity value is experimentally higher than the computed. It should be noted that the computed and measured frequencies for maximum sensitivity are in good accordance.
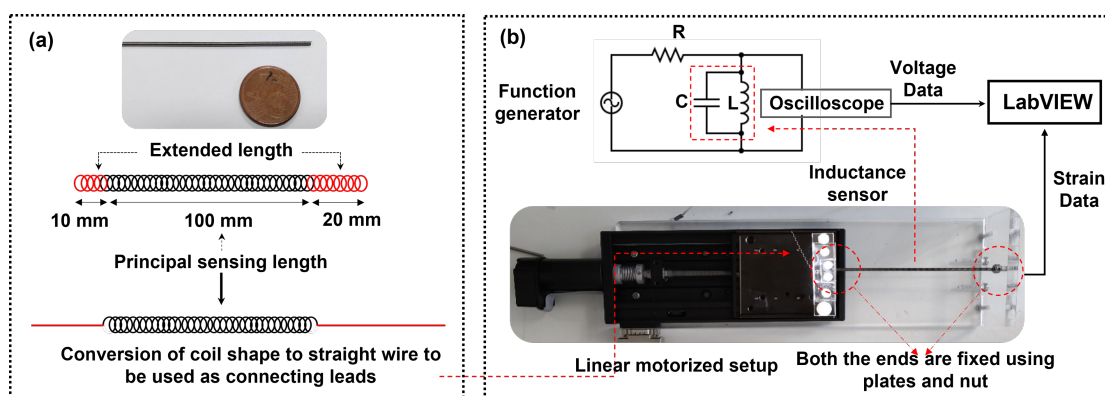
Figure 5.6: Experimental measurement setup for the strain estimation

To check whether the proposed method can be applied with other springs, the procedure is also followed for the second spring listed in Table 5.1 with the same circuit resistance value (220 Ω). The results from calculating the best frequency are as shown in Figure 5.8, highlighting the alignment of the theory with the experiment. For higher
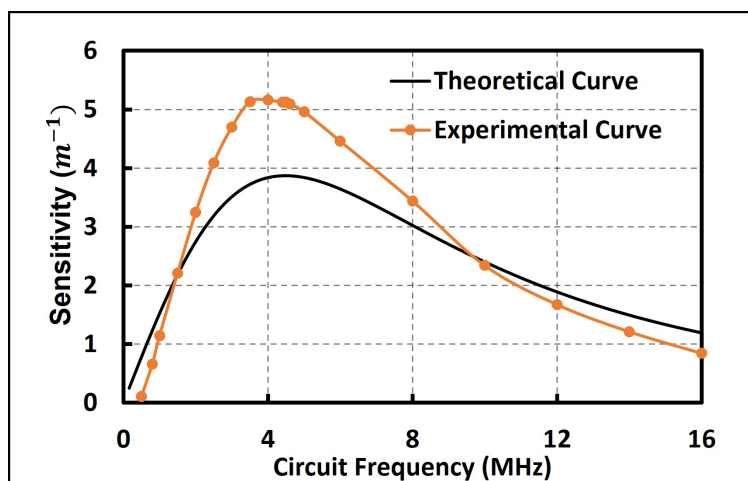
Figure 5.7: Comparison between experimental results with theory for 1.15 mm diameter spring
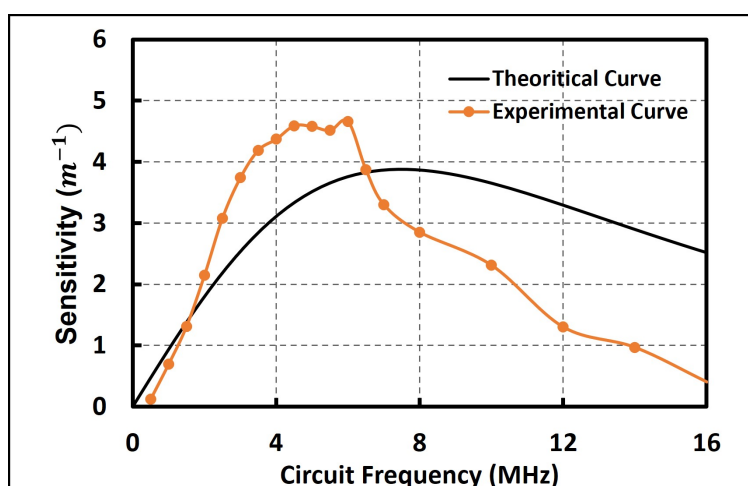
Figure 5.8: Comparison between experimental results with theory for 0.85 mm diameter spring

frequencies, however, the estimated values differ from the experimental results. The variation might be due to the considerations which are made in establishing the sensitivity expression (Equation 4.9), such as neglecting the internal electrical resistance and the variation in the pitch and diameter of the sensor. Regardless, the method seems applicable and helpful in setting the measurement conditions.

5.2.3 Impact of deformation mode on the sensor's characteristics

The derivation of the gain and sensitivity in Section 4.2.1 is performed by considering the spring length variation. This variation can be due to a pure linear elongation with coil

loops remaining parallel or bending, or a combination of these deformation modes (Figure 5.9) when the sensor is placed in a flexible manipulator. Additionally, the stated model uses a basic coil model considering parallel coil loops. In bending cases, this model may be inaccurate since the hypothesis is no longer valid. Having to calibrate the sensor for each type of deformation is time-consuming. It can also be a constraint if the deformation mode changes during the use of the flexible device, especially if external contact occurs.
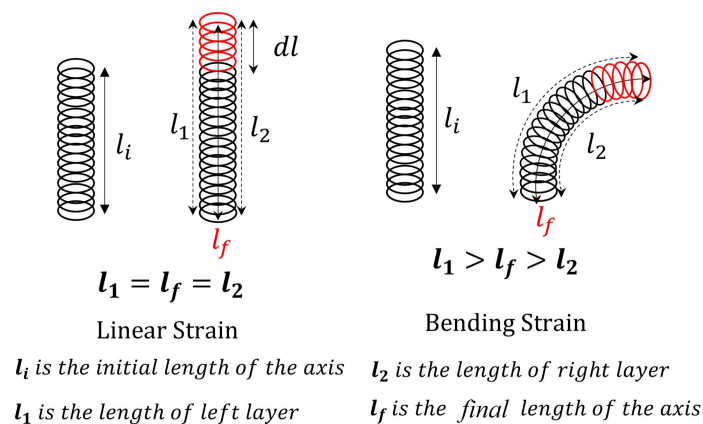
Figure 5.9: Schematic representation of the spring with different applied strains

An experimental investigation is then carried out to verify if the calibration can be performed only once, to accomplish the measurements of the spring's curvilinear length. For this reason, an experimental setup is fabricated using plexiglass. The setup comprises four adjustable semi-circular plates of different radii and the linear stage (Figure 5.10).
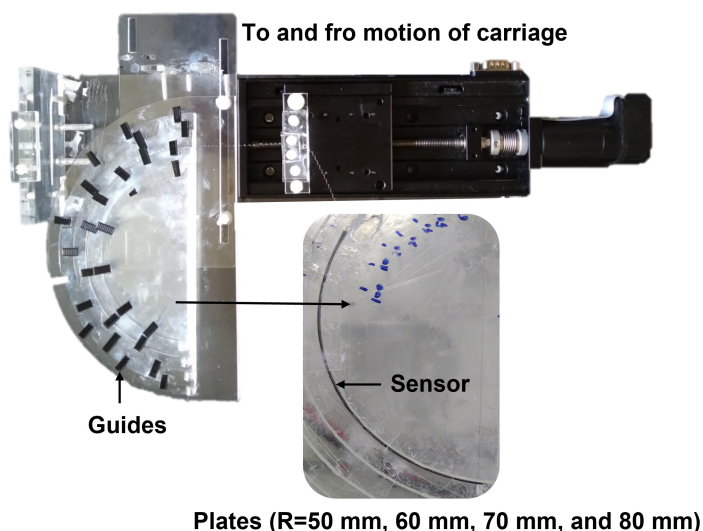
Figure 5.10: Experimental setup for investigating the impact of bending

One end of the sensor (spring 1) is fixed to one end of the semi-circular plate and the other is connected to the stage setup using a stainless-steel thread. Given its intended use in soft and flexible devices for medical applications, a 40% elongation is applied to the sensor by moving the stage setup. The elongation and P-P voltages are acquired from the setup which are further used to find the plot between gain and elongation during bending. The experiment is repeated for four arbitrary radii (50 mm, 60 mm, 70 mm, and 80 mm). Subsequently, the curves generated from this process are compared with the curve produced by the sensor for a linear elongation of the same amplitude using the setup given in Figure 5.6.
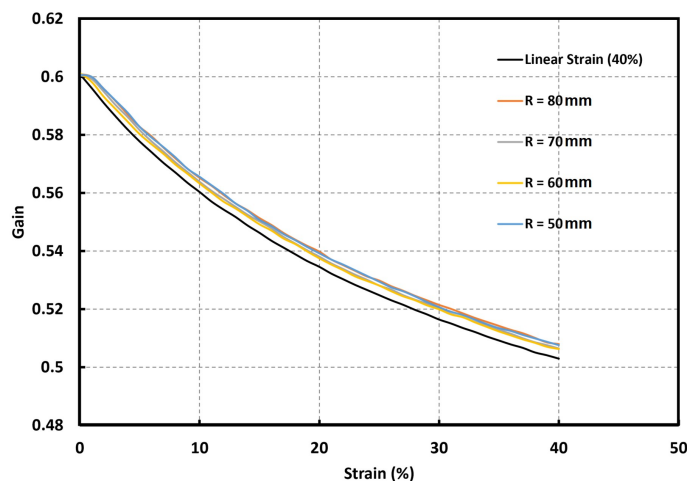
Figure 5.11: Comparison of the gain and strain relationship for the bending and linear strains.

The comparison between the experimental results is displayed in Figure 5.11. It shows that the gain change remains almost constant (0.1% variation among the gain change) despite the change in the radius of curvature. The experiment concludes that the sensing capability is independent of the radius, and exclusively depends on the amount of strain applied. However, the effect of bending on the characteristic curve might not be negligible when compared to the straight line curve. For example, when the length at 0.54 gain for various radii and straight configurations is estimated, it is observed that the variation remains between 1.5 mm and 2.5 mm. Thus, considering this range of error is acceptable, a single calibration can be performed for a given spring before any integration and used for finding the strain, given the system's type (e.g. bending or linear). However, this

error can be reduced by generating a calibration curve taking the average of all data. In the case of the involvement of multiple strain modes, the difference between various strain modes (bending or linear) can be identified and measured using multiple sensors.

5.3   Investigation on the achievable performance

The estimation of hysteresis, stretchability, and accuracy is highly essential before implementing the sensor for the shape reconstruction process. Hence, a detailed characterization process is conducted to understand the achievable performance of this type of sensor. The evolution of gain as well as hysteresis during repetitive loading is elaborated. Moreover, the strain rate effect to consider the impact of elongation speed, precision, and accuracy are considered while investigating the sensing behaviours. Spring 1 is used for the testing and is connected to the setup described in the previous section (Figure 5.6). The input signal frequency and voltage magnitude are set to 4.5 MHz and 5 V, respectively, following the conclusions of section 4.1.

5.3.1   Evolution of gain and the presence of hysteresis during repetitive loading

The sensor is subjected to a repetitive loading by applying an 80% strain using the stage setup shown in Figure 5.6. Next, the P-P values of the output voltage across the sensor are acquired regularly for the forward and backward motions. This is repeated for 100 cycles. The resulting gain and time are plotted to investigate the gain change in each cycle. The gain change of a cycle can be defined as the difference between the gain at 0% and the gain at 80%. Figure 5.12a shows the relationship between the gain for each cycle and time. The difference between the gain change for the first and the last cycle is calculated as 0.03%. This shows that the gain change remains almost the same for each cycle during repetitive loading. The sensor is also tested with progressive loading by applying a deformation starting from 5% for 10 cycles which reaches upto 80% progressively. The relation between gain change and time is given in Figure 5.12b. Similar behavior is observed when subjecting the sensor to progressive loading with repeated cycles at each step.
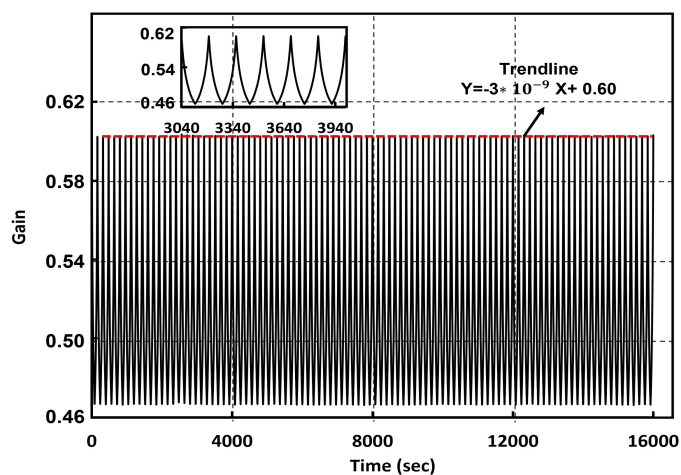
(a) Gain change for repetitive loading
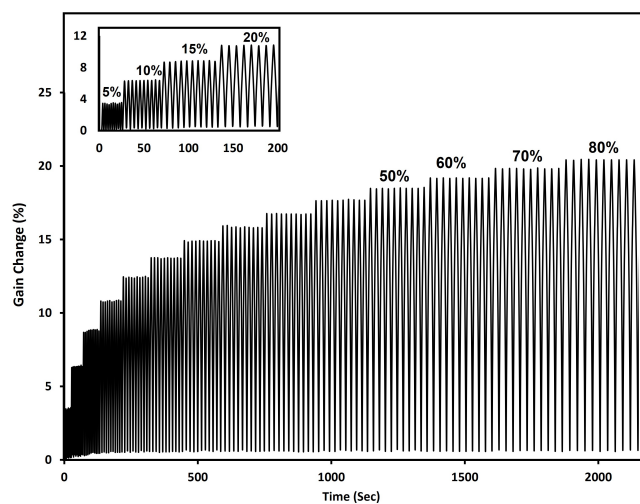
(b) Effect of progressive loading on sensing behaviour
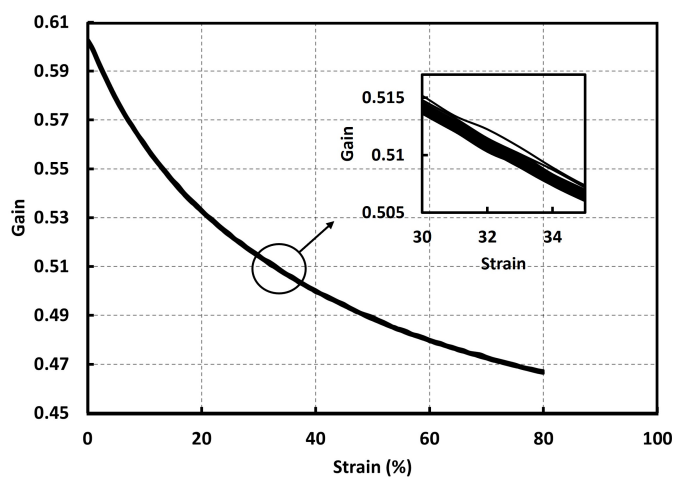
(c) Electrical hysteresis for 100 cycles

Figure 5.12: Effect of repetitive and progressive loading

The hysteresis produced by the sensor is estimated by plotting the acquired gain with respect to the corresponding strain during the repetitive loading. It is computed by determining the area inscribed in the cycle formed from the forward and backward curves. Figure 5.12c shows the electrical hysteresis of the sensor for 100 cycles at 80% strain. When the hysteresis of the sensor is calculated, it produces a mean hysteresis of 0.1% with a standard deviation of 0.023%. This shows that the sensor exhibits low hysteresis as compared to resistive sensors developed in Chapter 3.

5.3.2 Effects of strain rates on the sensing behaviour

The electrical hysteresis of the sensor for 80% elongation is estimated by varying the strain rates from 0.1 mm/s to 10 mm/s. Figure 5.13 shows the corresponding electrical hysteresis curves of the sensor at various strain rates. The curves remain almost similar and produce a mean hysteresis of 0.1% with a standard deviation of 0.09%.
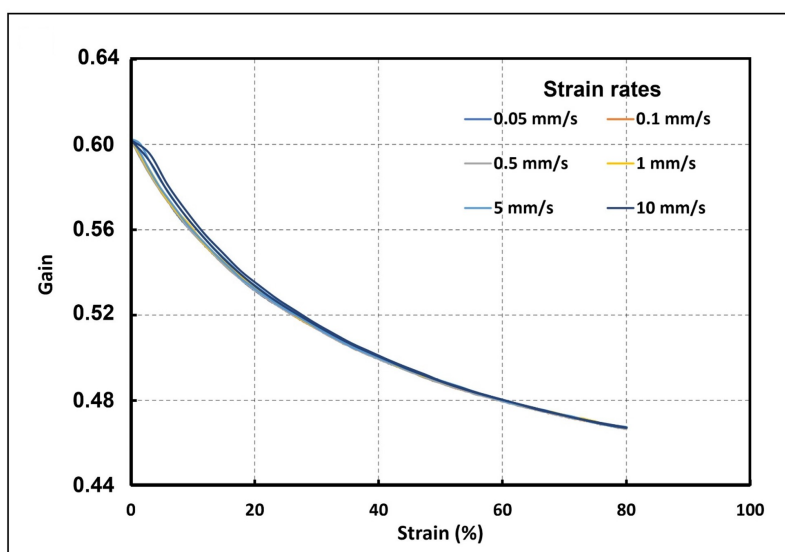
Figure 5.13: Effect of strain rates on electrical hysteresis

From Figure 5.13, it is observed that the hysteresis at different strain rates remains small. As the impact of speed on the hysteresis behaviour of the sensor is limited, it can be an interesting solution for a wide range of applications moving at various speeds ranging from 0.1 mm/s to 10 mm/s.

5.3.3 Sensor calibration and curve fitting

The gain expression developed in Section 4.1 is based on a simple physics-based modeling of the sensor behavior. For calibration, a curve fitting approach was preferred to maximize the accuracy of the measurement.
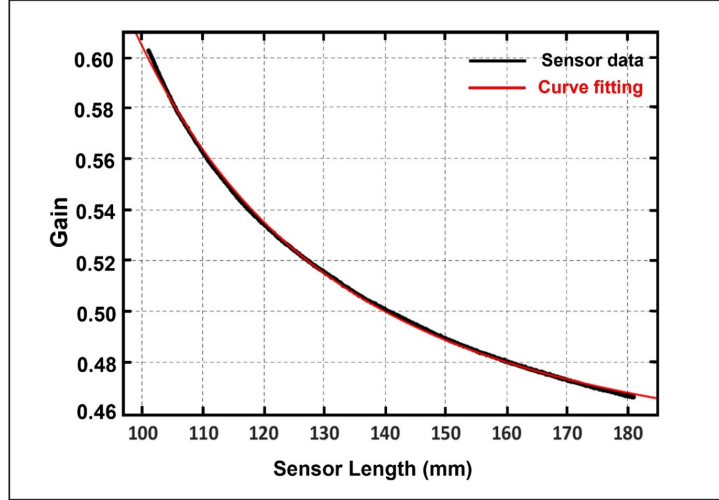
Figure 5.14: Sensor calibration

As the trend of the plot between gain and length data is non-linear, the linear curve fitting method is immediately rejected. Next, other curve-fitting basis functions with increasing complexity (inverse, polynomial, and power) are considered and compared in terms of R-squared values. The best description is obtained with a power curve as shown in equation (4.11) (Figure 5.14), with a goodness of fit of 0.9994 (R-square). This calibration is used for calculating the length in the remaining part of the paper.

$$l = (\frac{1.417 * 10^5}{G - 0.4395})^{0.337} \tag{5.11}$$

5.3.4 Sensor precision and accuracy

For precision assessment, a known elongation is applied to the sensor for 30 times (15 times forward and 15 times backward) using the linear motor stage. During this process, the gain is estimated by acquiring the voltage across the sensor and used in Equation 4.11 to calculate its length. The calculated length data of 30 trials are utilized to find the percentage mean deviation among them. This is repeated for a series of nine different

lengths ranging from 100 mm to 180 mm, as shown in Table 4.2. The maximum deviation observed is equal to 0.14%.

Table 5.2: Evaluation of the sensor's precision

Elongation (mm)	Mean Deviation (%)
101	0.011
110	0.036
120	0.056
130	0.06
140	0.072
150	0.12
160	0.14
170	0.09
180	0.12

The mean value obtained for each predefined spring length is finally compared to the reference value imposed by the setup. Figure 5.15 shows the mean and standard deviation of the length estimation process showing the maximum error at 80% strain. The mean deviation calculated in Table 4.2 shows the indication of repeatability over 30 trials, while Figure 5.15 shows accuracy at each deformation. The average accuracy is 0.73 mm, which represents 0.9% of the applied strain. Compared to capacitive and resistive sensors [175, 176], our proposed inductive sensing method produces adequate precision and accuracy over an 80% deformation range.
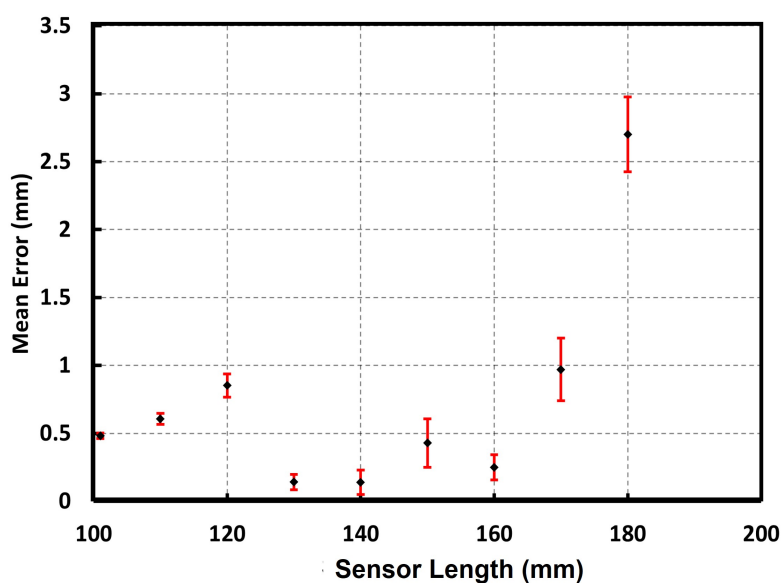
Figure 5.15: Sensor accuracy at various lengths

5.3.5   Sensitivity to EM interference

The proposed inductive sensor can be prone to surrounding electronic equipment generating EM signals. Hence, it is essential to investigate the effect of EM waves on the behaviour of the inductance sensor. Using the setup shown in Figure 5.16, the effect of EM waves on the inductance sensor is carried out. In this case, an EM field generator (Aurora, NDI Digital, UK) is used for the generation of EM waves.
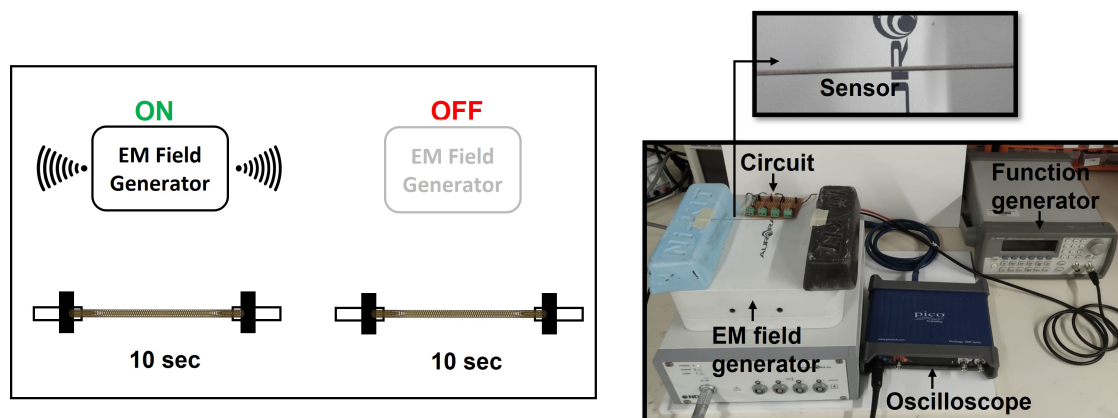
Figure 5.16: Setup for investigation of EM interference on sensing behaviour
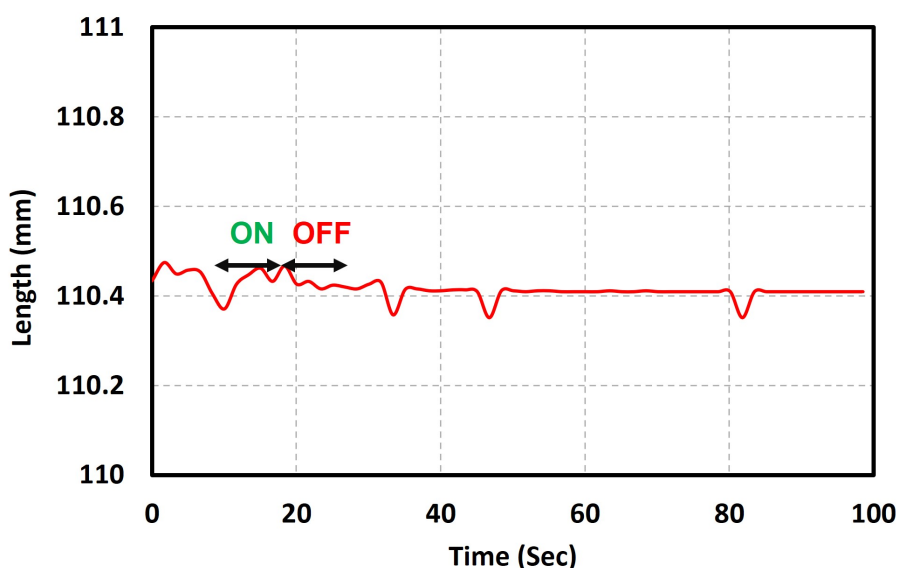
Figure 5.17: Sensor response towards EM waves

During this investigation, the length of the sensor is maintained constant and then the EM generator is switched on for 10 sec and turned off for the next 10 sec. This procedure is followed for 100 sec to see the impact of EM waves on the sensing behaviour.

It is observed from Figure 5.17 that there is no significant error produced due to the EM waves, as the estimated length of the sensor remains almost constant, i.e, 110.4 mm even with the application of the EM field.

5.4 Feasibility of sensor application in different robots

The characterization process shows that the sensor exhibits a low amount of hysteresis compared to previously investigated resistive sensors. The sensor shows adequate precision (mean deviation in the order of 0.14%) and accuracy (mean error of 0.9%) which appears to fulfill our required criteria. Since our aim is to reconstruct the shape of soft and flexible robots used in MIS, the feasibility of the sensor application process in different robots should be verified before the shape reconstruction process. Furthermore, it is crucial to investigate the added value of proprioceptive sensing during the actuation of various robots. In order to investigate these, two robots are considered in which the same inductive sensor is integrated. The first one demonstrates the use of the sensor in a soft robot featuring a large strain in elongation. The second one is a tendon-driven bending manipulator to detect and control the radius of curvature during bending.

5.4.1 Sensor integration in a soft and stretchable robot

As a first robot, the inductance sensor is integrated with a soft robot/actuator prototype that can extend up to a strain of 80%. The design and manufacturing are based on the process presented in [177]. The pneumatic artificial muscle (PAM) or soft robot considered here comprises two solid ends and an artificial muscle in the middle. The artificial muscle is fabricated using an expandable braided sleeve and a stretchable elastomeric cylindrical core made from silicone rubber. Initially, the fabrication of the soft robot started with preparing the extended sleeve. In this case, a braided sleeve is introduced inside a cylindrical rod and compressed to one-fourth of its initial length. Both ends of the sleeve are fixed on the cylindrical rod with the help of zip ties and

heated inside an oven by maintaining a temperature of 150°C. The detailed procedure is given in Figure 5.18. A wavy-like profile is created during this procedure which is then used with an elastomeric core to manufacture the artificial muscle.
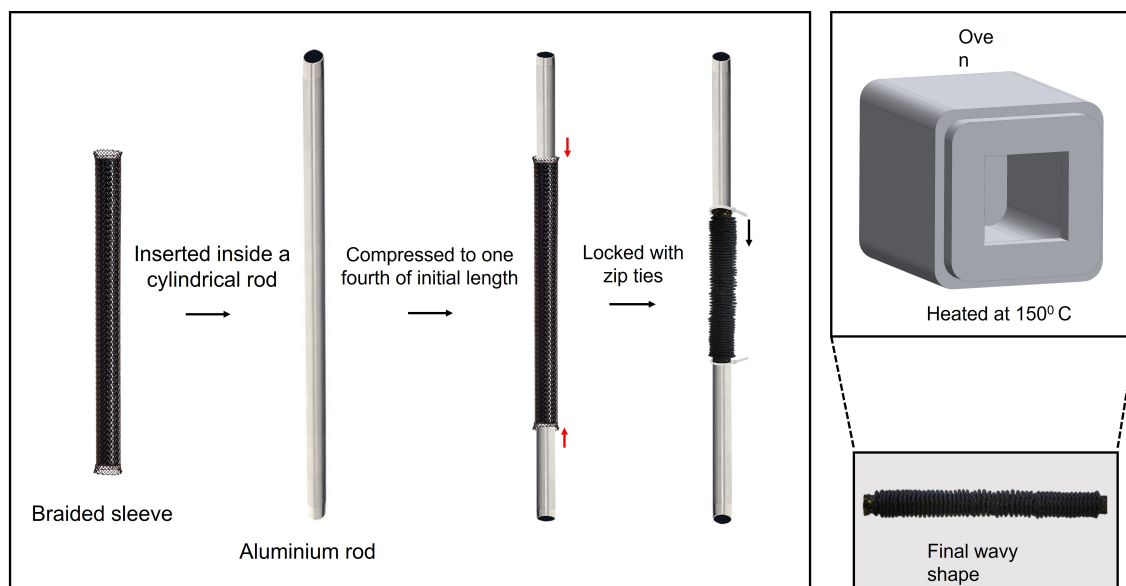
Figure 5.18: Fabrication of wavy-like structure

To make the elastomeric core, a mold is printed in the 3D printer and subsequently the liquid material prepared from Ecoflex-0030 is poured into it. The mold consisting of the liquid material is left for one day for curing. After the curing process, the elastomeric core is removed from the mold and is then connected to the solid ends by introducing the spring along the central axis.
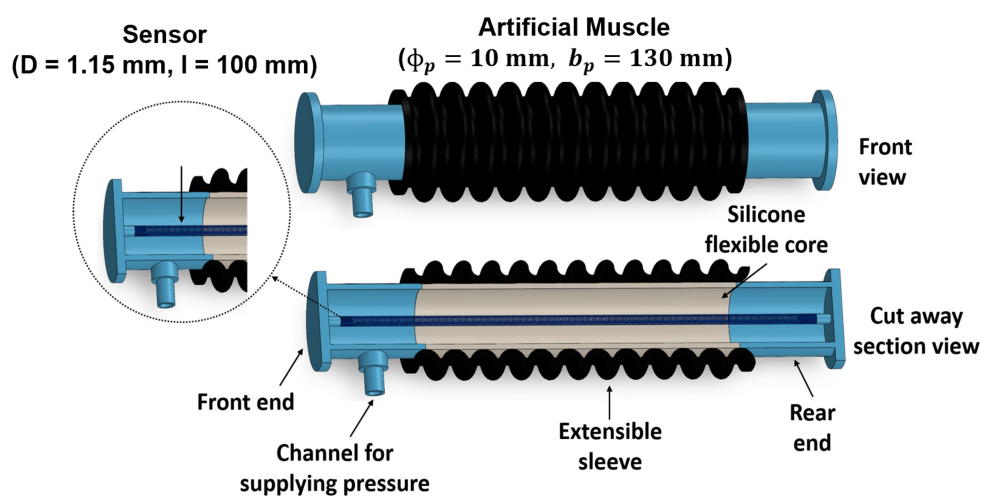
Figure 5.19: Different components of PAM in CAD

Finally, the assembled elastomeric core with solid ends is inserted inside the wavy profile and sealed using silicone glue and belts, thereby creating a pressure chamber. The final assembled PAM has a diameter (ϕ_p) of 10 mm, and a length (b_p) of 130 mm while contracted. When positive pressure is applied to the PAM, this configuration allows extending longitudinally along the central axis. The architecture and different components of the soft module are depicted in Figure 5.19 and 5.20.
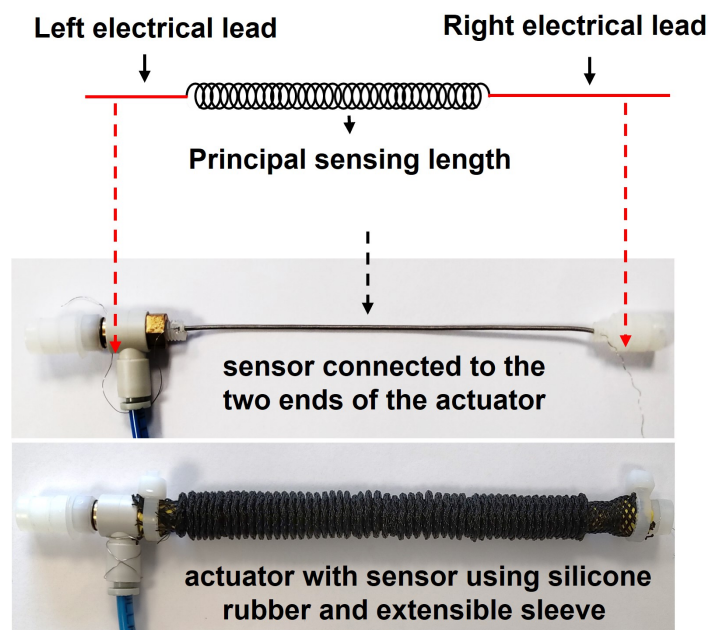
Figure 5.20: Fabricated PAM with sensor

The PAM is inserted in a transparent cylindrical guide ($\phi_g = 12$ mm, $b_g = 270$ mm) to restrict the robot's movement to a single direction. In this setup, the left end of the actuator is fixed at the beginning of the guide and the other end is free to move. The same configuration of the spring presented in Figure 5.6(a) is prepared and implanted along the central axis of the PAM while both ends are firmly connected to the solid ends using thread and superglue (Figure 5.20).

Closed loop position control of the soft robot

The closed-loop control of the PAM is performed in two steps. In the first case, the position of the tip of the robot is controlled in two different environments, i.e., open and foam environments. In the second case, the accuracy of the tip position during closed-loop control is accessed by comparing it with the ground truth.

We design a proportional controller for the closed-loop control of the tip of PAM using the length information from the sensor as feedback. The architecture of the closed-loop control of PAM is shown in Figure 5.21(a). Generally, this type of controller applies a correction called a controlled variable which is proportional to the difference between the required output and measured output. The proportional controller is implemented using LabVIEW where users can input their desired length of PAM (set point: SP). The error signal is calculated using the desired length and the feedback from the inductance sensor. Then, the error signal is processed in the controller and an actuating signal is generated using a data acquisition card (NI-USB 6363). Afterward, the signal is applied to a pump (KNF, Model No.-NMP830.1.2KPDC-B) capable of producing a maximum pressure of 3 bar that generates the pressure according to the actuation signal and is supplied to the PAM to move forward and backward based on the desired length of PAM. Here, the length of the PAM (feedback) is computed using the same procedure described in subsection 4.3.4. Figure 5.21 shows the schematic and real control loop for PAM.
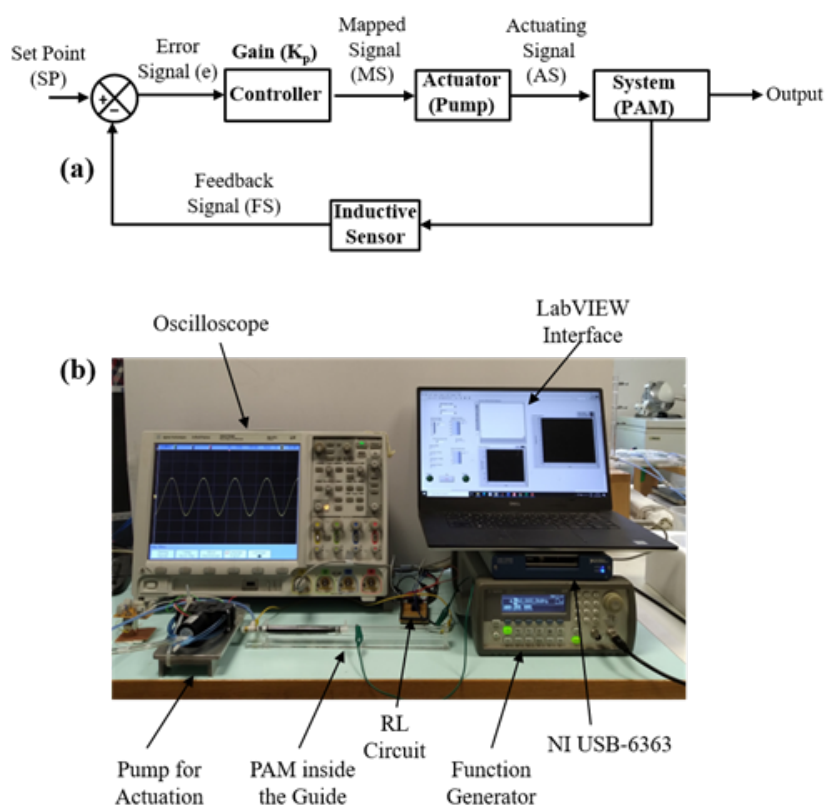
Figure 5.21: (a) Architecture of PAM's tip control; (b) different components of the control loop

To evaluate the performance of this feedback control loop using the proportional controller, we perform two different experiments. In the first experiment, the system is excited with discrete reference deformation and the response of the controller to reach a steady-state position is investigated. We apply 10 mm discrete steps to the system in an increased and decreased manner to observe the system response with respect to the reference.

Position and timing diagram of PAM for controller gain = 0.4
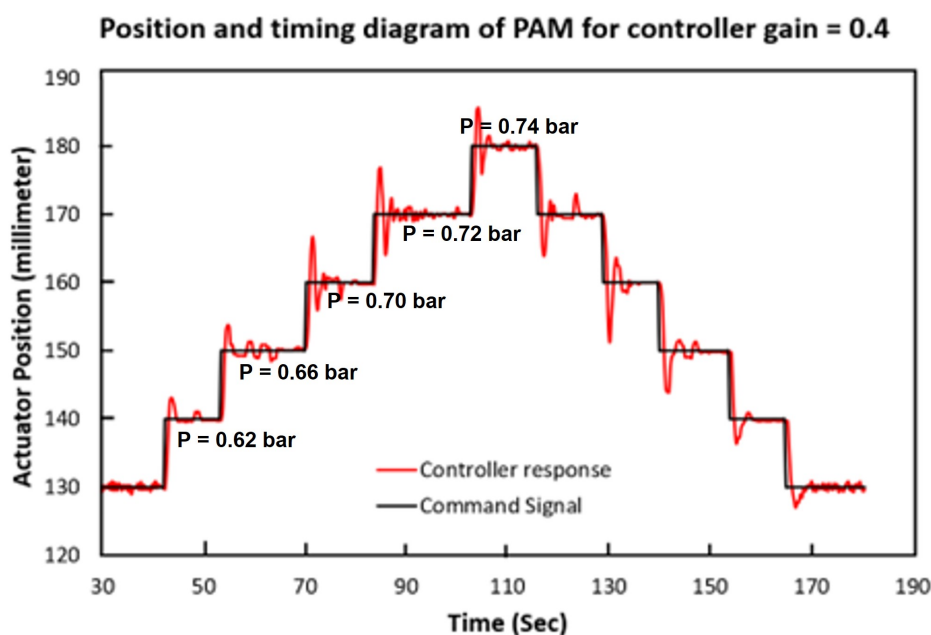
Figure 5.22: Controller response when 10 mm discrete steps are applied

Figure 5.22 shows the command signal and controller response along with the pressure information. It is observed from Figure 5.22 that the system response matches the desired signal with a mean rise time of 1.07 s for 0.4 controller gain. It is also observed that the robot comes to a steady-state position after performing a few oscillations. In the next experiment, the step size is increased to 20 mm to see the response for the bigger step, and the closed-loop control is performed for two different environments. The first environment is called the open environment where the robot's tip is free to move inside the guide. In the second environment which is defined as the foam environment, a piece of foam is inserted inside the cylinder which applies a force at the tip of the robot. Figure 5.23 shows the PAM in both environments.

Figure 5.24 shows that the system comes to a steady-state position even when there
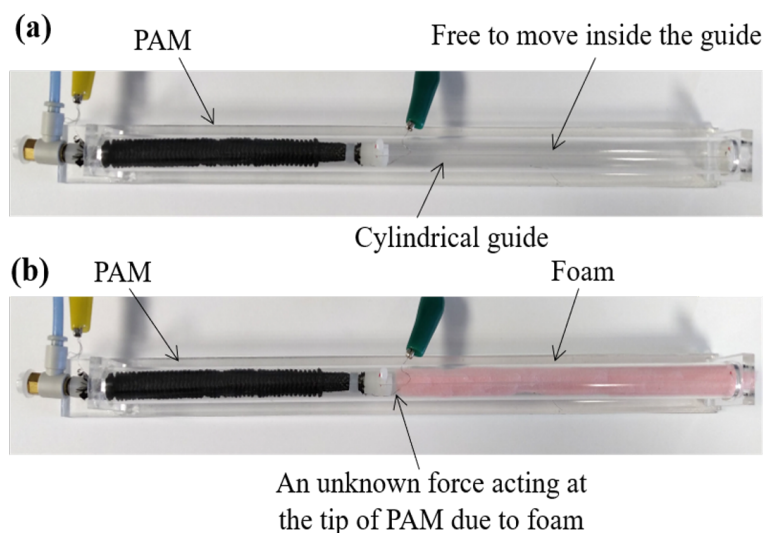
Figure 5.23: (a) PAM in open space; (b) PAM in the foam environment

is an unknown external force acting at the tip. The mean steady-state error is found as 0.55 mm with a standard deviation of 0.37 mm for the open environment and 0.39 mm with a standard deviation of 0.15 mm for the force acting at the tip respectively. The small steady state error produced during the foam environment as compared to the open environment is because of the force exerted by the foam which reduces the oscillations.
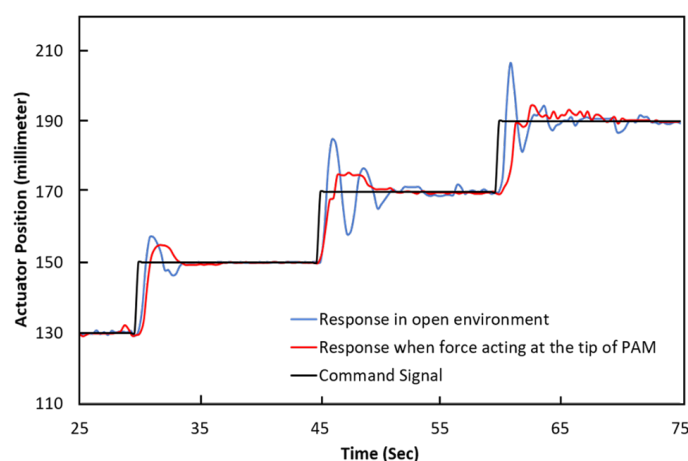
Figure 5.24: Controller response when 20 mm steps are applied in various environments

Accuracy assessment relative to ground truth

To access the error during the tip control, the closed-loop results are compared with an EM system. In this case, one electromagnetic (EM) sensor (Aurora, NDI Digital, Canada) is used at the tip that provides the ground truth length of the soft robot with

respect to the fixed base. During the previous process, we observe oscillations during the closed-loop control which might be due to the involvement of the pneumatic motor. Hence, the P-control setup is improved by using a compressor and P-control valve.
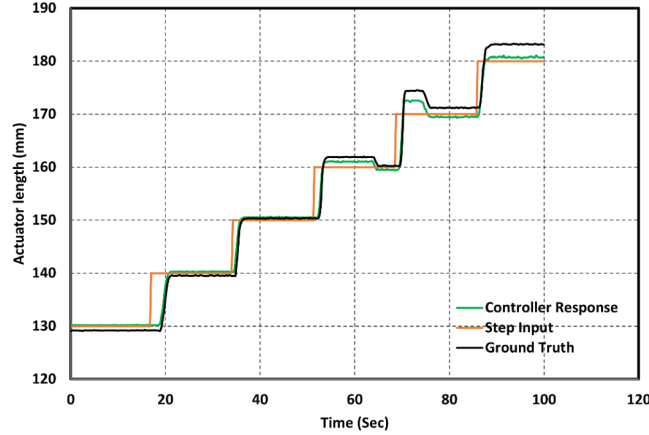
Figure 5.25: Comparison of length estimated from the sensor with ground truth

The behavior of the soft robot is assessed by exciting the system with 10 mm step input at 20 s-intervals from 130 mm (0% strain of the sensor) to 180 mm (50% of the length of the sensor) of the length of the actuator. Finally, the length from the sensor is estimated and compared with the ground truth length produced by the EM sensor. The difference between them is estimated as 1.16 mm $\pm$ 0.75 mm (Figure 5.25).

All in all, the closed-loop control of the PAM shows that the sensor effectively controls the soft actuator in different situations with different step sizes despite the absence of any physical model. Moreover, the low error in the closed-loop control shows that the sensor could be a solution for many soft actuators for precise control while avoiding the issue of stretchability.

5.4.2 Sensor performance evaluation in a tendon-driven robot

Since the ultimate goal of this study is to reconstruct the shape of flexible robots, it is decided to use the inductance sensor for testing into the second robot which is a tendon-driven flexible robot. For these kinds of flexible robots, curvature estimation is a crucial process before shape reconstruction. Thus, in this case, the capability of the sensor during the curvature sensing is investigated and additionally, the ease in sensor integration is

also observed. The robot is fabricated using eleven cylindrical disks made of plexiglass. The disks are 20 mm in diameter and 3 mm in thickness. Moreover, the cylindrical disks have a central hole (h = 0.8 mm) and four channels (D = 1.15 mm) at the periphery (Figure 5.26). A flexible Nitinol wire with 0.8 mm in diameter is used as the central core of the system in which the disks are glued by maintaining a distance of 10.7 mm from each other. Two springs (as described in Table 4.1, second column, initial D = 1.15 mm, and l = 100 mm) are embedded into two channels (opposite to each other) of the robot by prestretching them to 40%. One of the springs is used as a sensor while the other is intended to balance tension forces. One interesting feature of these sensors is their easy integration. Here, the robot's design is only slightly modified to easily mount the springs simply by gluing their ends to the top disk. As shown in Figure 5.26, the extra helical coils of the springs are converted into straight configurations which are further inserted through the other channels present in the robot to connect to the circuit. Thanks to the hollow configuration of the springs, two cables are inserted inside them which are further connected to the motor using a pulley for actuation. The detailed design and fabrication of the robot with the sensor are shown in Figure 5.26.
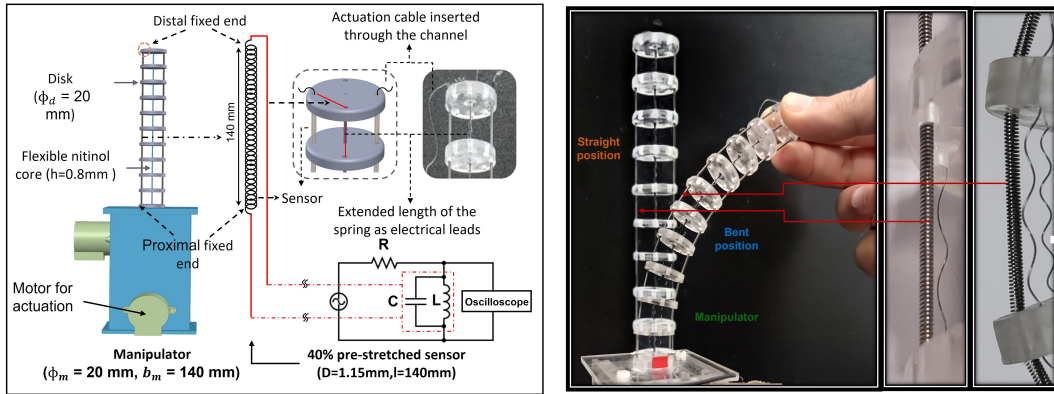
Figure 5.26: Sensor integration in the tendon-driven robot

A PID controller (Figure 5.27) is designed to control the radius of curvature of the flexible manipulator. This radius is estimated using a basic model, with a constant curvature assumption:

$$r = \frac{l_n}{\theta} \tag{5.12}$$

$$\theta = \frac{l_n - l_s}{a} \tag{5.13}$$

where l_n, r, and θ are respectively the length of the neutral axis, radius of curvature, and angle of curvature of the manipulator respectively while l_s is the length of the sensor, and a is the distance from the central axis of the manipulator to the sensor.
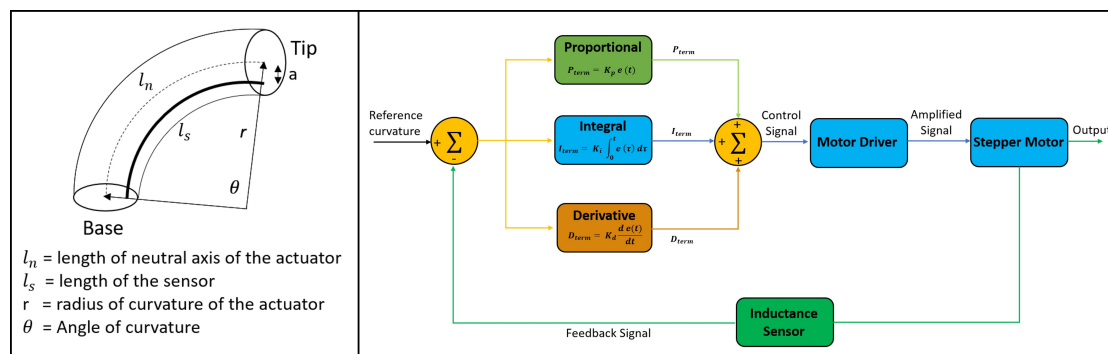
Figure 5.27: A PID controller for controlling the radius of curvature
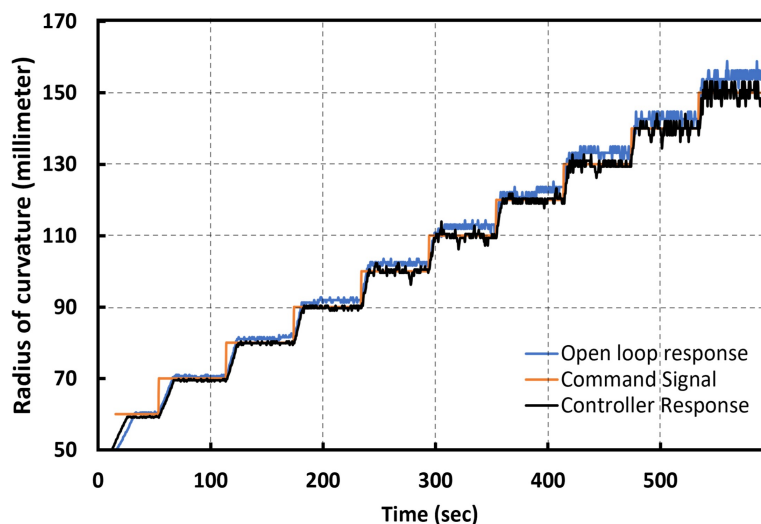
Figure 5.28: Control of the radius of curvature of the robot using sensor information

In the literature, different curvature sensing solutions are presented for various medical robots performing bending radii ranging from 40 mm to 150 mm [178, 100, 108]. In some cases, for instance, a minimum bending radius of 100 mm is needed for approaching the upper gastrointestinal tract to bypass the large organs. Considering these aspects and following the requirement from Chapter 1 to measure the radius of the flexible robot dealing with high deformation, ten desired radius of curvature signals between 60 to 150 mm are selected. Each radius is applied for 60 sec, and the controller response is observed. For comparison, an open-loop control is performed using the cable length, and the results

are compared with control signals (Figure 5.28). The mean steady-state error in the case of the open-loop control is estimated as 5 mm (3.6% of the length of the robot) while for the closed-loop control, this error remains as 2 mm (1.43% of the length of the robot). Therefore, it is possible to reduce the control error by 2.5, thanks to the sensor which is also convenient for integration from a hardware point of view. In addition to this, it is observed that the sensor is capable of detecting a radius of curvature up to 60 mm and may also be used for detecting the tighter radius of the highly flexible robot.

5.5   Discussion

In this chapter, a method is proposed to estimate the strain using a simple voltage measurement instead of performing a direct measurement of inductance. This simplified the required instrumentation and can be implemented to measure the strain with readily available equipment. Meanwhile, it can be seen that the circuit composed of a resistor and a spring as a variable inductor can be adjusted so the sensing properties, namely sensitivity and gain, can be optimized by tuning the circuit parameters. A full characterization process is conducted for the sensor to elaborate on its hysteresis, stretchability, repeatability, strain rate response, precision, and accuracy. From the characterization, it can be concluded that the issue of hysteresis of resistive sensors can be solved using the proposed inductive sensing since it exhibits only 0.1%. In addition to this, it seems to fulfill the required criteria of accuracy. As the sensor can stretch more than 80%, it solves the stretchability issue of FBG. Thus, it can be used in highly flexible robots where implementation of FBG is highly complex and also not cost-effective as the FBG sensors are prone to wreckage. Since it doesn't involve any kind of radiation dosage or chemical injection during the operation, it can be a safe solution for implementing in the shape reconstruction procedure. The sensor's performance in the two devices shows that it can be easily integrated with a high level of compactness which can be an additional benefit during the shape reconstruction process if implemented. From the current chapter, it is observed that the sensor can easily estimate the radius of curvature using the length information in a model assuming

constant curvature assumption and has the capability to detect the tighter radius of the flexible robot. The fulfillment of the required criteria are summarised in Table 5.3

No.	Criteria	Inductive sensor
1	Stretchability to deal with the soft and flexible body	Highly stretchable (> 80 %)
2	Safe in terms of less reduction of radiation and contrast agent	A safe solution since it does not involve any radiation dosage and chemical agent
3	Accuracy should be as maximum as possible	Precision in the order of 0.14 % and 0.9 % mean accuracy
4	Robust to invivo conditions	Robust to invivo conditions since it depends upon the calculation strain rather than processing of images

Table 5.3: Overview of requirement criteria

It can be observed from Table 5.3 that the inductive sensor fulfills the criteria that are initially considered for the soft and flexible robot. Thus, the sensor can be used to reconstruct the shape of soft and flexible robots. In the next chapter, the shape reconstruction of a flexible robot will be investigated which will give a direction to the use of this sensor in general cases.

Chapter 6

Shape Reconstruction of a Tendon-driven Manipulator using Inductive Sensor

6.1   Introduction

The reason for the requirement of a shape reconstruction method in the case of precise and reliable motion control of soft and continuum robots is already discussed in Chapter 1. These robots continuously alter their body shape, moving in a straight, C-curved, or S-curved direction. Hence, the controller can be better comprehend the robots' shape-changing behaviour by using the data acquired from the shape reconstruction process, such as tip and backbone coordinates, which will aid with closed-loop control, path planning, and collision detection. The medical staff will also be able to visualize the robot in real time inside the anatomy using the extracted backbone information in conjunction with appropriate simulation software. This will enable the medical staff to precisely operate the robots while avoiding collision with healthy tissue. The fusion of different modeling methods with various sensing techniques to reconstruct the shape was discussed in Chapter 2. In this chapter, the use of the constant curvature modeling technique with inductive sensors for reconstructing the shape of soft and flexible robots is considered. A tendon-driven robot is employed for the shape reconstruction process since the robot has similar mechanical behaviour, and also encounters similar problems that soft and flexible robots face. Thus, the performance of the inductive sensor in the shape reconstruction process for the

tendon-driven robot is initially discussed which basically gives a direction to use the inductive sensor for reconstructing the shape of other soft and flexible robots used in the MIS context. The choice of using the constant curvature assumption is decided based on its simplicity and wide acceptance in the literature. The shape reconstruction method based on constant curvature follows two procedures. The first one is a mapping from the actuator space containing robots' deformation information to the configuration space parameters that characterize constant-curvature arc. The second one is mapping from the configuration space to the task space that describes position and orientation along the backbone. The study of shape reconstruction started with 2D shape reconstruction since it uses only a single sensor for shape estimation. For instance, this method can be useful for robots that are equipped with a base motor. In this case, the 3D motion can be achieved by combing in-plane bending and rotation of the base. In Chapter 4, the mapping from actuator space to configuration to calculate arc information for planar bending is described. In this chapter, the mapping from configuration space to task space is discussed. After the discussion of the case of the 2D shape reconstruction, the general 3D shape reconstruction process fusing multiple sensors' information with the constant curvature model is investigated. This case is useful in robots without a base motor where the 3D motion of robots can be achieved by combining in-plane and out-plane bending. Ultimately, conclusions are drawn about the usefulness of the inductive sensors in this context.

6.2 Shape reconstruction in 2D workspace

6.2.1 Shape estimation and accuracy assessment

In the case of the 2D reconstruction process, the tendon-driven robot discussed in Section 4.4.2 is considered. The first procedure of mapping from actuator space to configuration space described in Section 4.4.2 is followed here to calculate the radius and angle curvature of the flexible robot using the length information from the integrated sensor. Next, the mapping from configuration space to task space that describes the position and backbone information is performed which is also needed.

For the 2D shape reconstruction process of the system, the bending of the flexible robot is considered in one plane which is perpendicular to the disks. To estimate the shape, multiple discrete curvature points are calculated and further extended to the total length of the system. Since the bending of the system is assumed to be constant curvature, the relationship between radius (r), length (l), and angle of curvature (θ) is given as:

$$l = r\theta \tag{6.1}$$

In a cartesian coordinate system, the coordinates for a series of discrete points can be obtained as follows:

$$x_i = r(1 - cos(i.\Delta\theta)) \tag{6.2}$$

$$y_i = r(sin(i.\Delta\theta)) \tag{6.3}$$

$$\Delta\theta = \theta/n \tag{6.4}$$

where n is the number of discrete points present in the system and i ranges from 0 to n. The shape reconstruction process starts from the base and approaches to the tip of the robot. Figure 6.1 and the Algorithm 1 depict the procedure for the shape reconstruction of the robot in 2D space. In this case, the base of the robot is assumed to be fixed at origin O (0,0) and the center of the arc is considered on the x-axis.
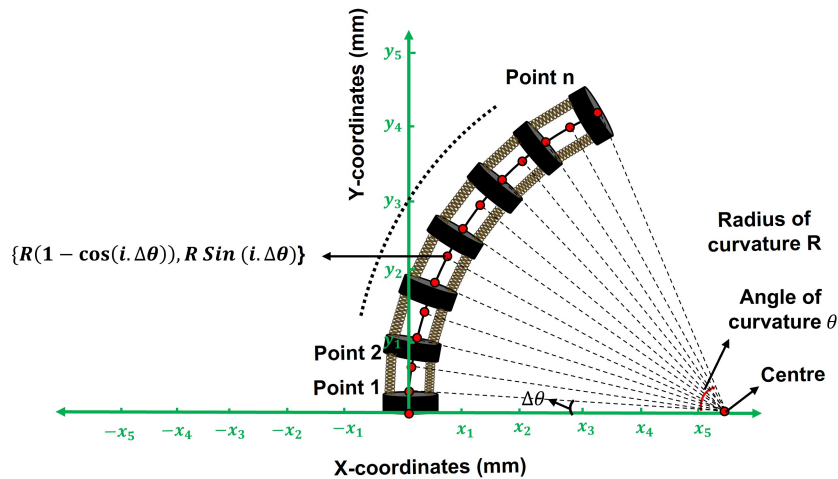
Figure 6.1: Shape reconstruction procedure for the robot in 2D space

Recalling Figure 5.27 and equations from Section 4.4.2, the radius and angle of the curvature are calculated using the length information from the inductive sensor. Using

---

Algorithm 1 Shape reconstruction algorithm

Require: r, θ, n
Ensure: Origin at O[0,0]
Ensure: Rotation angle $\alpha_0 = 0$
  while $KEY \neq STOP$ **do**
     Evaluate r
     Evaluate θ
     $\Delta\theta = \theta/n$
     if θ is negative **then**
        $\alpha_i = 0 - \pi$
     else if θ is positive **then**
        $\alpha_i = 0$
     while $i > -1 \& i < n$ **do**
        $A[j,1] = r - rCos(i\Delta\theta)$
        $A[j,2] = rSin(i\Delta\theta)$
     $ROT = [Cos(\alpha_i) - Sin(\alpha_i); Sin(\alpha_i)Cos(\alpha_i)]$
     $A = A \times ROT$
     $Plot(A)$

---

these arc parameters in Algorithm 1, the points of the robot's centerline are extracted. When the points are connected using linear interpolation, it represents the robot's centerline.
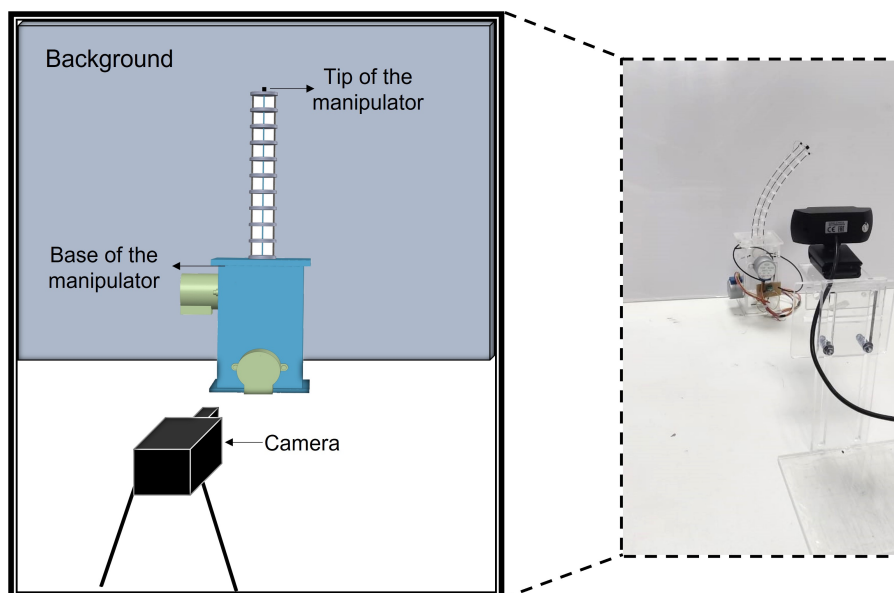
Figure 6.2: Setup for acquiring the real images

The shape reconstruction algorithm is performed in LabVIEW. The robot is actuated to different positions and the shape data are acquired in real-time. To find the accuracy in the shape estimation process, the reconstructed shapes are compared with the real

images. A setup consisting of a camera (Canyon, CNS-CWC5) is placed in front of the robot to capture the real images. During this process, the image plane is kept parallel to the bending plane by adjusting the movable plate of the setup where the camera is mounted. The setup for capturing the images is shown in Figure 6.2.

An image processing technique is carried out using ImageJ to find out the backbone coordinates of the robot from real images. In this case, a rectangular shape (5 mm $\times$ 8 mm) is attached to the base of the robot which is used to calibrate the images from pixel coordinates to Cartesian coordinates. After calibration to Cartesian coordinates, the feature points are selected along the neutral axis of the robot using the multipoint tool in ImageJ to extract their coordinates. Finally, the points are connected which represents the center line of the robot. Figure 6.3 shows the overall procedure for generating ground truth shapes of the robot from real images.
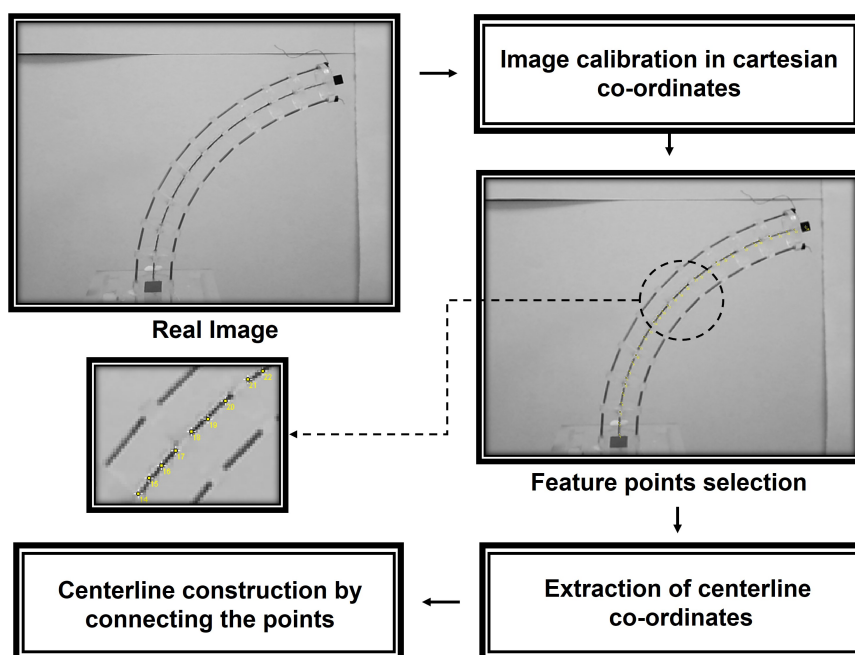
Figure 6.3: Procedure for producing the ground truth

Figure 6.4(a) shows the actual robot performing various shapes in the two-dimensional workspace while Figure 6.4(b) shows the comparison between the reconstructed shapes with the ground truth shapes generated from image processing. Hausdorff distance [179] is adopted to calculate how close the reconstructed shapes from the actual shapes extracted from images. Hausdorff distance can be defined as the largest distance of all the distances
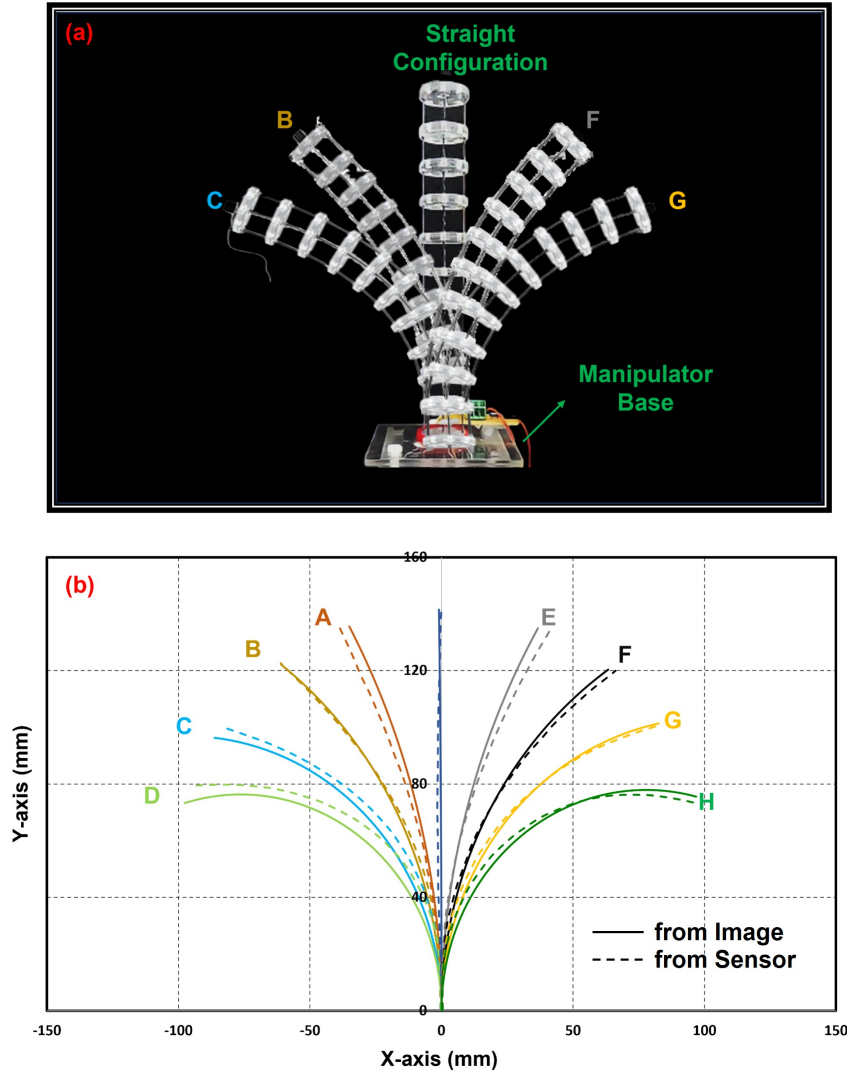
Figure 6.4: (a) Actual shapes of the robot; (b) comparison between the reconstructed shapes with ground truth shapes generated from real images

estimated from a point in one set to the closest point in other sets. Let's consider the reconstructed points belong to a set R and the points from the actual shape belong to a set A. Then the Hausdorff distance can be denoted as $D_H(R, A)$ which is given as follows:

$$D_H(R, A) = max(\max_{p \in R} \min_{q \in A} ||p - q||, \max_{q \in R} \min_{p \in A} ||p - q||) \tag{6.5}$$

The term $\max_{p \in R} \min_{q \in A} ||p - q||$ is called as directed Hausdorff distance from R to A. $D_H(R, A)$ finally results the maximum deviation that the reconstructed shape deviates from the actual shape of the robot. This process to calculate the Hausdorff distance is performed in MATLAB. Table 5.1 shows the error in the shape reconstruction process for various positions of the robot estimated using the Hausdorff method.

Table 6.1: Shape reconstruction error calculated based on Hausdorff distance

Points	error (mm)
A	4.9
B	3.4
C	4.8
D	6.7
E	5.2
F	4.1
G	4.3
H	5.4

From Table 5.1, it is observed that the shape reconstruction error for various positions remains between 3 to 7 mm. The highest reconstruction error is observed as 6.7 mm while the mean error is observed as 4.8 mm which represents 3.43 % of the robot. Since the error is calculated using Hausdorff concept, the error can be anywhere along the backbone. Compared to imaging, FBG, and EM shape reconstruction methods presented in the literature, the shape reconstruction error using the inductive sensor remains relatively high. However, this proposed method of shape reconstruction using the inductive sensor is a good compromise between accuracy, safety, and high stretchability. Additionally, this method might be still useful in instances such as controlling the endoscope during the screening of gastrointestinal tract [180] and aortic valve replacement [31] procedures where the 4-5 mm positional error might be acceptable.

6.2.2 Minimum error and uncertainty in 2D shape reconstruction

Minimum error

In the previous section, the inductive sensing technique is fused with a constant curvature model to calculate the shape estimation error. Realistically, tendon-driven robots exhibit non-constant curvature due to various phenomena (friction being the main factor [181, 182]). To determine the contribution of these phenomena, we compare the results of the reconstruction method to the best fit of a constant curvature model, which represents the minimum error of this kind of model.

To get the best fit data of the constant curvature model, a curve fitting method using

nonlinear least square fit is adopted. The curve fitting method fits a circle passing at (0,0) and tangent to the y-axis to the data points acquired from images. The equations for curve fitting are given as follows:

$$F = (x + R)^2 + y^2 - (R)^2;$$ (6.6)

$$Fit = lsqnonlin(F, R_0)$$ (6.7)

Where F is the basis function, x and y are the x-coordinate and y-coordinate, and R is the radius of curvature to optimize. All these above steps are performed in MATLAB. The function *lsqnonlin* is the nonlinear least-square function that is used to optimize the radius of the curvature of the basis function by taking the initial radius of curvature R_0. After successful iteration, it returns the optimized radius of curvature that best fits with the collected data of robot centerline coordinates from image processing. Considering the optimized radius of the curvature and the angle of the curvature, the best fit data is estimated and compared with the reconstructed data. Figure 6.5 shows the curve fitting method performed in MATLAB.
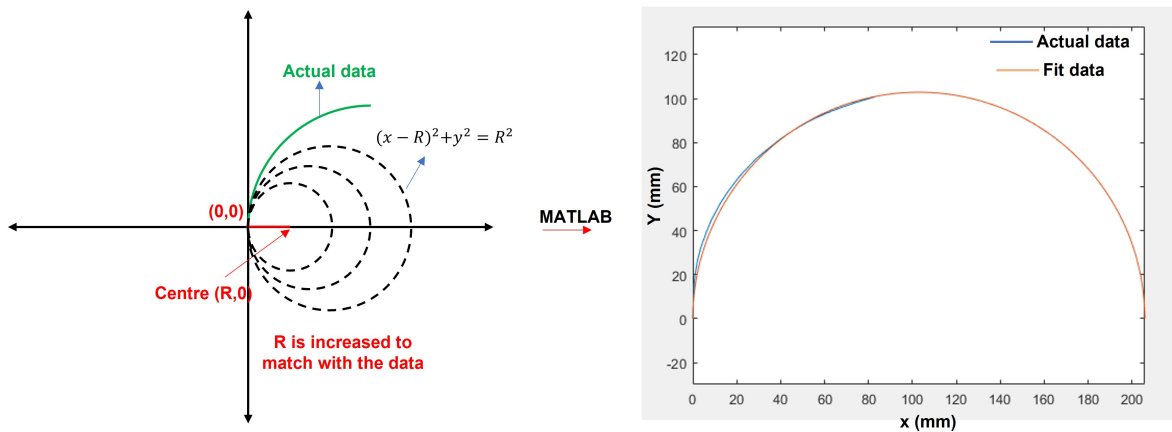
Figure 6.5: Method to find the best fit from the real data

Figure 6.6 shows the real, fitted, and reconstructed coordinates of the centerline of the robot. The minimum error can be estimated by finding the error between fitted data from the curve fitting process and the reconstructed data from the inductive sensor. The Hausdorff distance is used to calculate the shape reconstruction error and is reported in Table 5.2. Although we are aware that the robot is not constant curvature, we decided
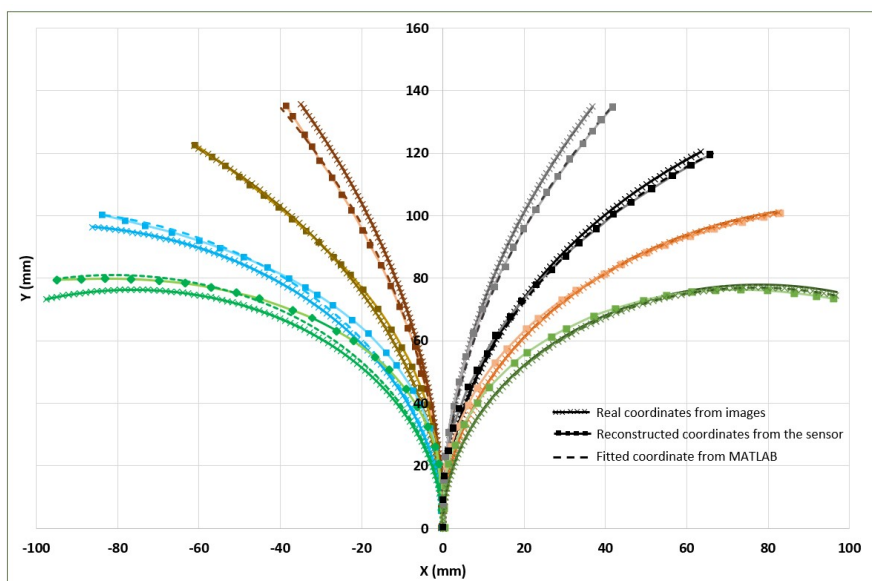
Figure 6.6: Comparison between fitted curve with real and reconstructed coordinates of the centerline of the robot

Table 6.2: Minimum error estimated based on Hausdorff distance

Points	Actual Error = error between reconstructed shapes by the sensor and shape extracted from image	Minimum Error = error between reconstructed shapes by the sensor and constant curvature shapes fitted to image shapes
A	4.9	4.9
B	3.4	0.7
C	4.8	4.3
D	6.7	5.7
E	5.2	5.1
F	4.1	2.9
G	4.3	0.7
H	5.4	1.0

to use a constant curvature model for the sake of simplicity and proof of concept. With this model, we can't get better estimates than a 3.2 mm error on average, and our results should be taken with this in mind.

Uncertainty

During the estimation of the shape reconstruction error, we have considered that the real images are always parallel to the image plane by assuming the robot bending plane and image plane in parallel. However, in practice, the planes might be distorted due to many effects such as rotation of the base, rotation of the camera, or small out-plane bending

of the robot. Thus, it is crucial to understand the uncertainty involved due to these phenomena. In order to estimate the uncertainty, the plane of the robot is considered to be rotated by an angle γ which can be seen in Figure 6.7. In this figure, the X and Y-axis
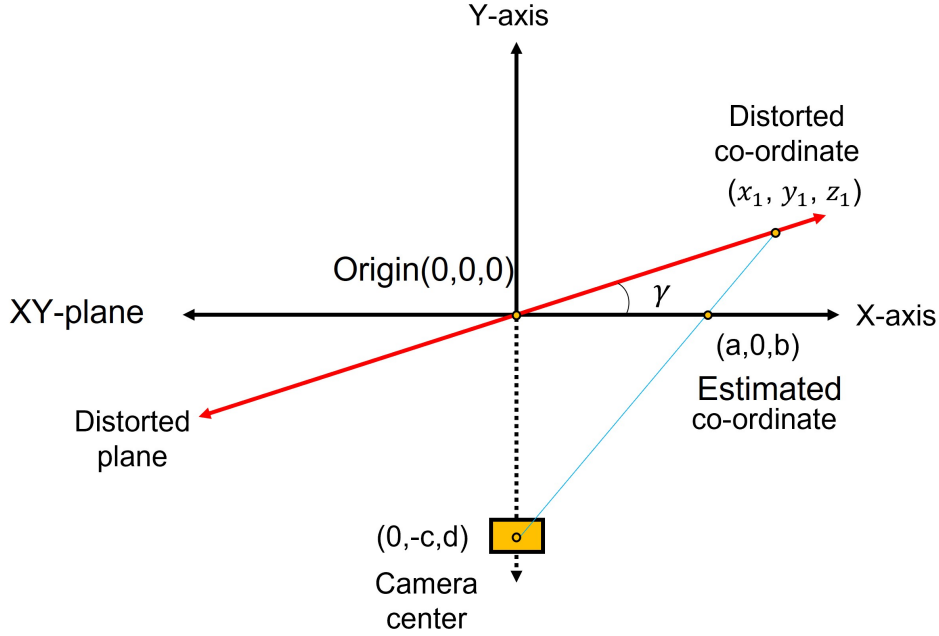
Figure 6.7: Uncertainty due to the involvement of distortion

are in the plane while Z-axis is considered as out of the plane of the paper. The camera is considered to be situated at a distance C from the origin on the Y-axis. When the actual XZ-plane is distorted, the estimated coordinate (a,0,b) will become the distorted coordinate (x_1, y_1, z_1) which can be calculated by finding the intersection between the distorted plane and the line intersecting the camera center and estimated co-ordinate. Since the distorted plane passes through the origin and Z-axis, the general equation of the plane is given as follows:

$$mx + ny = 0;$$

(6.8)

where m and n are non-zero constants. Substituting the distorted coordinate in equation 5.8 and solving the equation leads to the generation of the distorted plane equation which is given as follows:

$$x(tan(\gamma)) - y = 0;$$

(6.9)

The parametric equation of the line joining the camera center and estimated co-ordinate can be given as follows:

$$\frac{x - 0}{a - 0} = \frac{y + c}{0 + c} = \frac{z - d}{b - d} = t \tag{6.10}$$

Solving equations 5.9 and 5.10 results the value of distorted coordinates (x_1, y_1, z_1) which can be given as follows:

$$(\frac{ac}{c - a(tan(\gamma))}, \frac{ac(tan(\gamma))}{c - a(tan(\gamma))}, \frac{bc - ad(tan(\gamma))}{c - a(tan(\gamma))}) \tag{6.11}$$

Rotating the distorted coordinate by γ about the Z-axis results:

$$(\frac{ac(cos(\gamma) + tan(\gamma).sin(\gamma))}{c - a(tan(\gamma))}, 0, \frac{bc - ad(tan(\gamma))}{c - a(tan(\gamma))}) \tag{6.12}$$

The uncertainty in X can be computed by subtracting the X-coordinate from equation 5.12 from the X-coordinate of the estimated one, which is given as follows:

$$X_{uncertainty} = \pm|a - \frac{ac(cos(\gamma) + tan(\gamma)sin(\gamma))}{c - a(tan(\gamma))}| \tag{6.13}$$

Similarly, the uncertainty in Y is given as:

$$Y_{uncertainty} = \pm|b - \frac{bc - ad(tan(\gamma))}{c - a(tan(\gamma))}| \tag{6.14}$$

Therefore, there will be uncertainty in X and Y-coordinates if the planes are not in parallel and can be calculated using Equations 5.12, 5.13, and 5.14. Considering an ideal situation where the robot is behaving with constant curvature and no misalignment, the reconstructed coordinates can be considered as perfect ground truth, i.e, estimated coordinates. Now to illustrate the uncertainty, the distortion is considered between 1-5°, and the distorted coordinates are calculated by substituting estimated and camera coordinates in equation 5.12. After estimating the distorted coordinate, the effect of distortion is observed by estimating the distance between the reconstructed and distorted coordinates. Figure 6.8 shows the overall distance error of all positions (from A to H) of the robot for various distortion angles. It shows that the mean error and maximum error (observed at the tip of the robot) reach 1.5 and 7.2 mm, respectively. The figure also shows that the error increases with the increase in misalignment. Realistically it is very hard to avoid a misalignment of 3-4 degrees due to many reasons (parallax error being

the one while setting the base of the camera). Hence, this uncertainty due to 3-4 degrees might also affect our estimated shape reconstruction error.
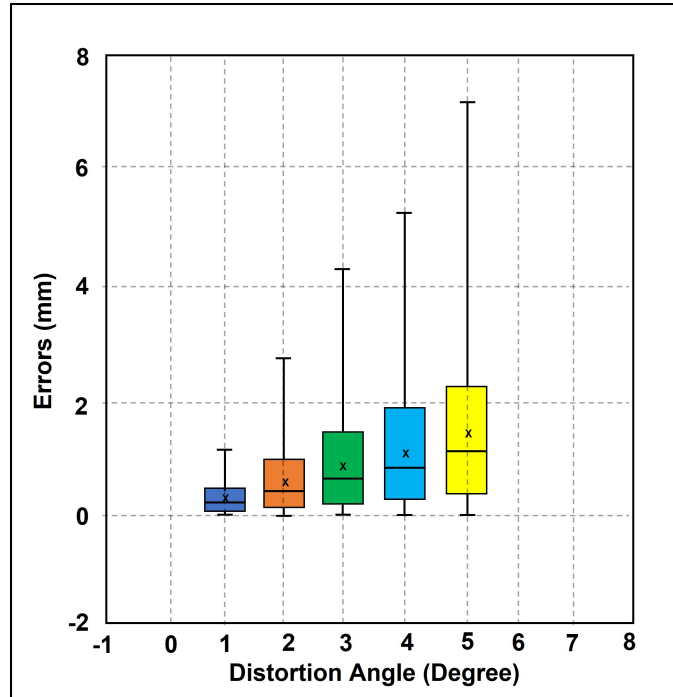
Figure 6.8: Effect of distortion in the ground truth

6.2.3 Tip tracking in 2D workspace

Shape reconstruction inaccuracy may be found at the tip or at the base or it can be anywhere along the center line. However, in some instances, the tip position is observed so that the robot can reach to target location [31]. In addition to this, since the tip is an actuating part of the robot, it may exert excessive force which might damage the tissue or anatomy. Hence, the tip positional information is needed to provide feedback to the controller to perform accurate manoeuvering [134] as well as to avoid collision with the tissue.

To track the tip, an imaging processing method based on pattern matching is adopted. This method comprises two stages which are learning and matching. The algorithm uses the template image to extract information about edge gradients and/or gray values of a specific region of interest during the learning phase. The information is stored and organized by the algorithm in a way that speeds up searching in the inspection image. The knowledge gained during this phase is saved as a part of the template image.

The pattern-matching algorithm extracts edge gradient and/or gray value information from the inspection image during the matching stage (corresponding to the information learned from the template). The algorithm then locates the areas in the inspection image with the highest cross-correlation to find matches. Since the matching points are in pixel coordinates, they have been converted to cartesian coordinates by calibrating the image. The same setup given in Figure 6.2 is used for tip tracking. In this case, a rectangular shape (3 mm × 3 mm) is placed at the top of the robot which is assumed as the tip. The image processing method is implemented in LabVIEW where the algorithm processes the captured image to track the tip of the robot. Figure 6.9 shows the image processing technique for tracking the tip.
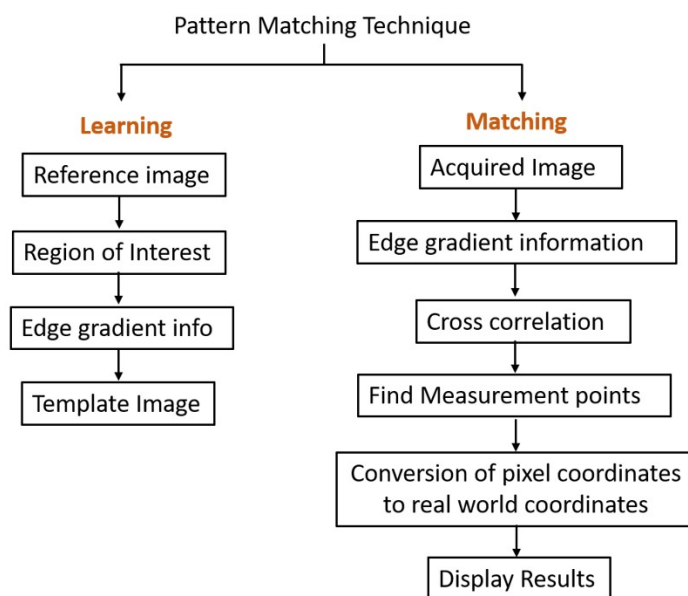
Figure 6.9: Tip tracking algorithm based on pattern matching technique

The acquired tip coordinates are compared with the reconstructed tip coordinates which are shown in Figure 6.10. Finally, the error between them is estimated by finding the distance between the actual and reconstructed tip which shows a mean error of 2.2 mm with a standard deviation of 1.3 mm. From tip tracking, the minimum and maximum tip tracking errors can be found as 0.2 mm and 6.9 mm, respectively. In this case, if uncertainty exists, it can be computed by following subsection 5.2.2.

It is observed that the highest shape reconstruction and tip tracking error is at the farthest left of the robot. Recalling Figure 5.14, it can be observed from the calibration
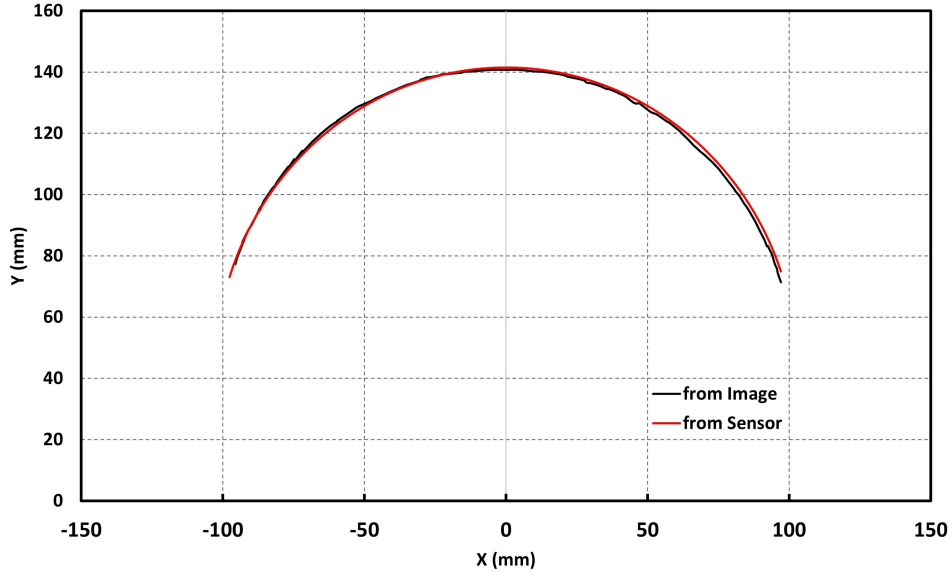
Figure 6.10: Comparison of tracking errors between tip coordinates collected from image and sensor

curve that the sensor shows good sensitivity from 0 to 40 % deformation, i.e., the gain change remains 71 % of total gain change for 40% strain. The sensitivity of the sensor reduces thereafter from 40% to 80%, i.e., 29 % for the next 40% deformation. Hence, the highest reconstruction error might be due to the use of the right sensor which deforms more than 40 % and reduces the effectiveness of the strain sensing due to the decrease in sensitivity when the robot actuates to left. Another possibility of the highest reconstruction error might be due to the possible deviation from constant curvature for a tighter radius. As the robot consists of two springs, a mechatronics approach can be identified that can combine the information from both left and right sensors in the shape reconstruction process to reduce the error.

All in all, the shape reconstruction method using a single inductive sensor for planar motion shows that the method is capable of estimating the shape of the flexible robot due to the high stretchability property of the sensor. Compared to FBG-based shape reconstruction methods [178, 108] that are capable of estimating the shape up to a radius of curvature of 80 mm, the inductive-based shape reconstruction process can estimate the shape up to a tighter radius of 70 mm (Curvature $= 14.3$ m^{-1}) without involving high complexity in sensor integration and calibration process. This method of estimating the shape for planar bending might be useful in some robotic systems where the actuation to

reach a target in 3D space is performed by combining in-plane bending and rotation of the base of the robot. An example of this kind is given by Donno et al. [183]. The use of a single sensor can help to determine the position of the robot in 3D space. However, a 3D shape reconstruction using multiple sensors is needed for more complicated robots which actuate in 3D space by combining in-plane and out-plane bending.

6.3 Shape reconstruction of the robot in 3D space

Unlike 2D shape reconstruction where one sensor is enough to estimate the shape, the 3D reconstruction of the flexible robot requires three or four sensors in a triangular or quadrangular configuration. Thus, the previous flexible robot is modified using four sensors. In this case, four sensors with quadrangular configuration has been chosen to help the robot to bend in a constant curvature manner. In terms of the mechatronics design viewpoint, the sensor integration and tendon routing processes become easier for this kind of configuration as the tendons pass through the sensors. Additionally, two motors are enough to actuate the robot in 3D space. In this case, a soft backbone with a bigger diameter is used instead of nitinol wire to increase the stiffness. A 12 mm in diameter soft cylindrical core is manufactured by using a silicone material (Dragon Skin 30, Smooth-ON, USA). A similar concept explained in section 3.4.1 of Chapter 3 is adopted to fabricate the soft backbone. After the curing process, the soft backbone is removed and ten ring-type disks of 12 mm inner diameter and 20 mm outer diameter are glued equidistantly. The disks have eight 1.2 mm holes (four holes for four sensors and others for sensor cables). Four tendons of diameter 0.4 mm are introduced in the springs and connected to two motors using two pulleys as discussed in section 4.4.2 of chapter 4. Due to the bigger diameter, the soft core provides better stiffness which maintains an almost constant curvature behaviour of the robot. The actuation of the robot in 3D space is performed by combining the rotation of both motors. Figure 6.11 shows the robot actuating to different points in 3D space.

The shape of the robot in 3D space is reconstructed assuming constant curvature which is also given in [24]. Similar to the 2D reconstruction process, the 3D reconstruction
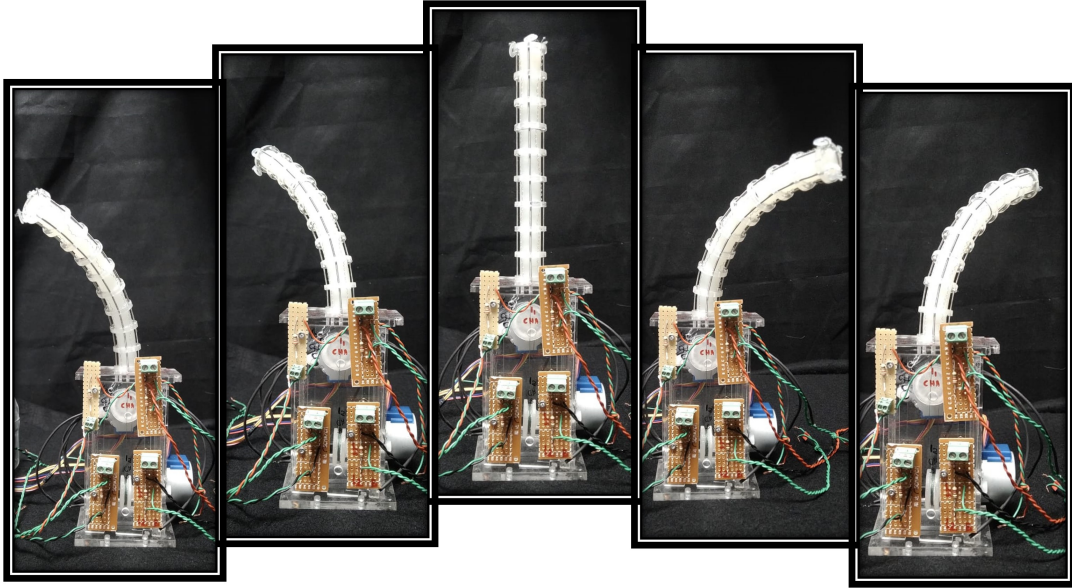
Figure 6.11: The robot actuating to different points in 3D space

process is also divided into two parts which are shown in Figure 6.12.
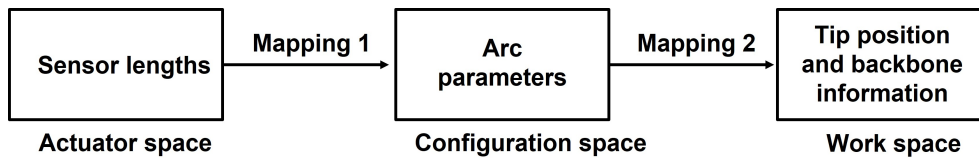
Figure 6.12: Mapping between different spaces of the robot

The first one is from actuator space consisting of the length of the sensors to configuration space consisting of the arc parameters, such as curvature, arc length, and angle containing the arc. The second one is from configuration space to workspace which provides the position information of the tip and backbone. All the arc parameters and their relationship are shown in Figure 6.13. Mapping 1, i.e, from actuator space to configuration space is robot specific as it depends upon the robot and sensor configuration, while mapping from configuration to workspace, i.e., Mapping 2 is independent since it can be applied to all systems which are assumed as constant curvature.

The arc parameters (ϕ, r, l, κ, and θ) of the robot can be derived based on Webster et al. [24] and given as follows:

$$l = \frac{l_1 + l_2 + l_3 + l_4}{4} \tag{6.15}$$

$\emptyset$ = Angle containing arc

θ = angle of curvature

l = arc length

K = curvature

r = radius of curvature
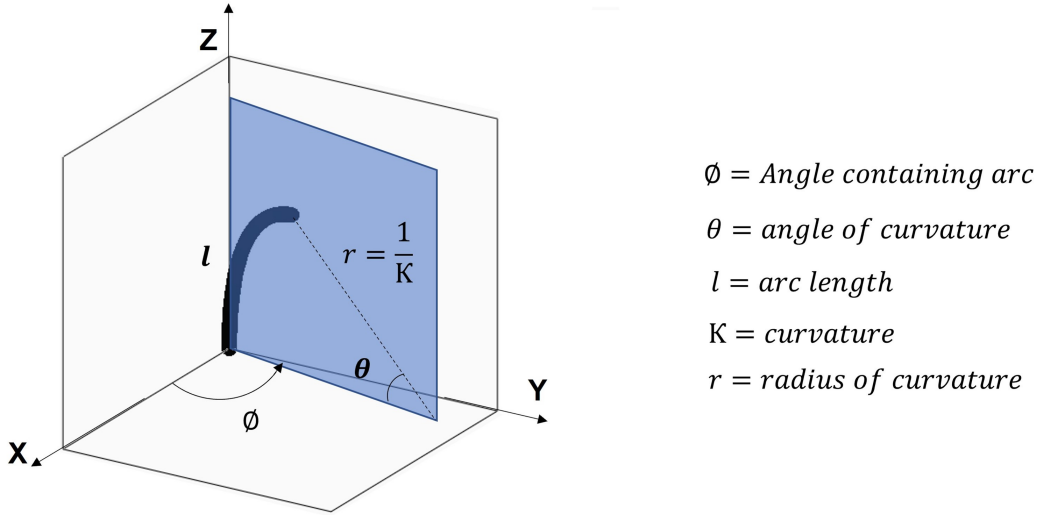
Figure 6.13: Different parameters of the robot and their relationship

$$\kappa = \frac{(l_1 + l_2 + l_3 + l_4)\sqrt{(l_4 - l_2)^2 + (l_3 - l_2)^2}}{d(l_1 + l_2 + l_3 + l_4)(l_4 - l_2)} \tag{6.16}$$

$$\phi = \arctan(\frac{l_4 - l_2}{l_3 - l_1}) \tag{6.17}$$

Where l_1, l_2, l_3, and l_4 are lengths of the four sensors placed in the quadrangular configuration. The mapping from the configuration space to the workspace can be performed by considering rotation and in-plane transformation. From Figure 6.13, considering $\phi = 0$, the coordinates of a point on the circular arc of radius r in the x–z plane are [r(1-cos(θ), 0, rsin(θ)]. When the arc is rotated by ϕ, the homogeneous transformation from arc to tip can be given as follows:

$$T = \begin{bmatrix} R_z(\phi) & 0 \\ 0 & 1 \end{bmatrix} \begin{bmatrix} R_y(\theta) & 0 \\ 0 & 1 \end{bmatrix} \tag{6.18}$$

Four similar circuits to the one described in section 4.2 of Chapter 4 are prepared and connected to the function generator and an oscilloscope (Picoscope, Pico Technology, UK). At the input site, all of these four sensors are connected to the function generator in parallel while four channels of the oscilloscope are used to acquire the voltage data at the output site. Figures 5.13 shows the configuration for connecting four sensors.
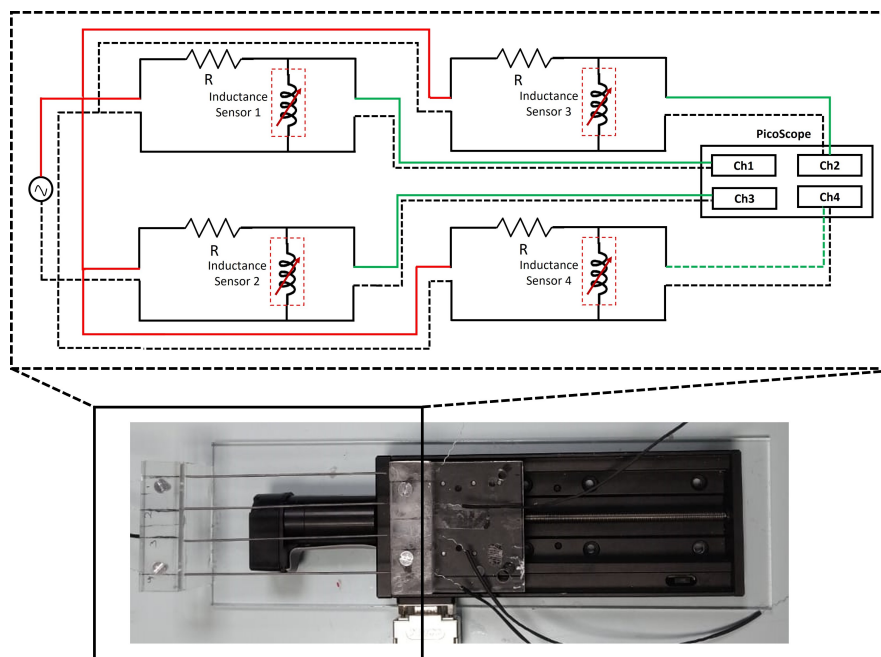
Figure 6.14: Electrical circuit and stage setup for multi-sensors connection

Using the setup, the P-P voltages across the four sensors are acquired and the gains are estimated. Since all the sensors are connected to the input supply in parallel, ideally the gains across the sensors should remain the same as the gain across a single sensor circuit connected alone to the function generator. However, we observed that the gains are reduced when using the multi-sensor configuration compared to the single-sensor configuration in reality. This might be due to the load produced by the sensors on the AC voltage source while handling multiple sensors. Certainly, this issue can be addressed by connecting four sensors to four separate circuits, each with a dedicated function generator and signal acquisition card. We rather chose to re-calibrate the sensors in the multi-sensors configuration since the method is cost-effective and time-saving from a practical point of view. It should be worth noting that the sensors are not calibrated directly inside the robot instead the same procedure discussed in Section 4.3 is followed but with multiple sensors connection. To perform the calibration process, all the sensors are connected to the stage setup and the circuit as given in Figure 6.14.

An 80 % strain is applied to the sensors and P-P voltages across the sensors are acquired. The relationship between gain and strain generated from this process is shown in Figure 6.15. Four calibration curves are generated by implementing the same
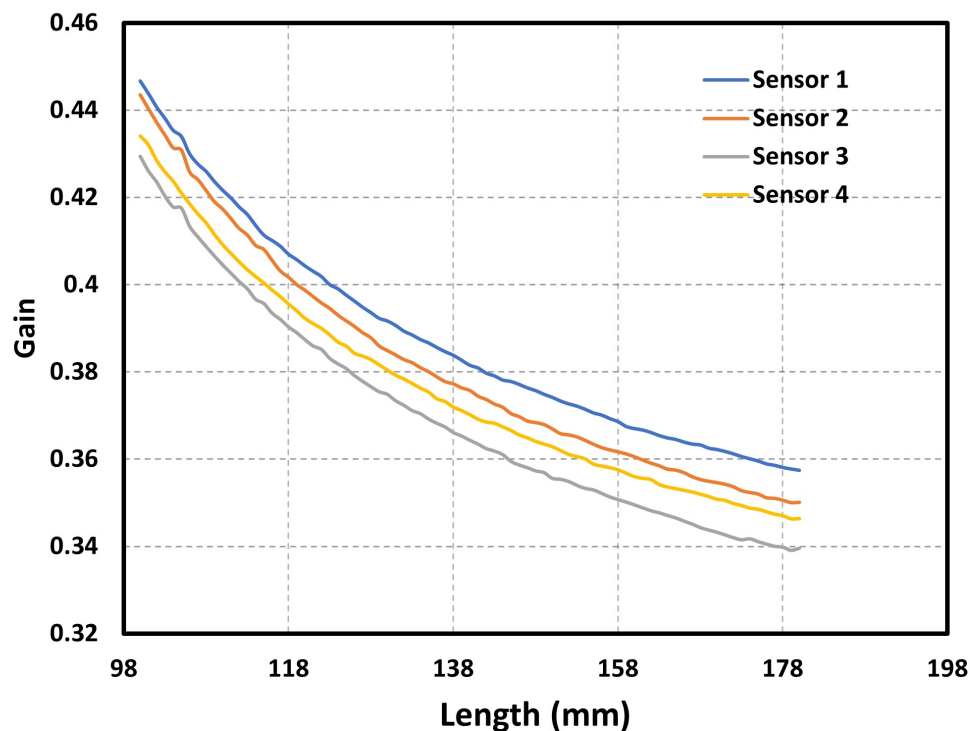
Figure 6.15: Calibration curves of four sensors generated from the curve fitting process

curve fitting approach discussed in Section 4.3.3. The four equations resulted from the calibration procedure are used to estimate the length of the sensors. To calculate the arc parameters of the tendon-driven robot, the length information is substituted in Equations 5.15, 5.16, and 5.17. The transformation matrix T is next used to reconstruct the shape of the robot. The robot performing different shapes is shown in Figure 6.16.

The accuracy in the shape reconstruction process for the 3D workspace is estimated by comparing the reconstructed tip coordinates of the robot with ground truth tip coordinates. In the case of ground truth, an EM sensor is placed at the tip which provides the real tip coordinates of the robot. Since the robot comprises two motors for actuation, the electromagnetic field generator of the EM sensing unit is placed at the top to reduce the EM interference. The effect of rotation and inclination of the robot is also considered while measuring the ground truth. Initially, the base plane where the robot is placed has been made parallel to the EM generator by checking the inclination using a liquid level indicator. This is done to check the inclination error due to the table where the robot is placed. After this initial check, the rotation angle about the
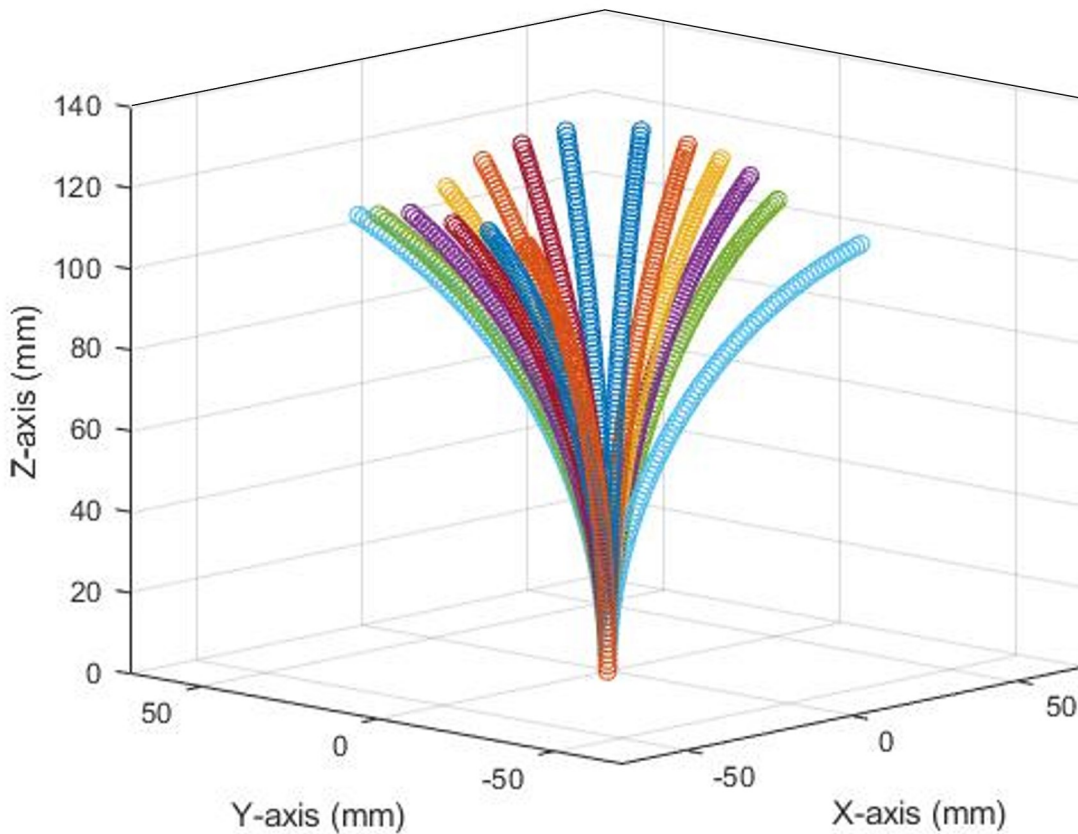
Figure 6.16: The reconstructed shapes of the robot for different points in 3D workspace

Z-axis and inclination angles along the x and y-axis are also measured using the EM sensing system. To measure the rotation about Z-axis, a fixed frame is installed. Using the EM system, the coordinates of two corner points of the fixed frame (coordinate 3 and 4 of Figure 6.17) and two corner points of the robot's base (coordinates 1 and 2 of Figure 6.17) are measured. Finally, the angle of rotation is calculated by finding the angle between the line joining coordinates 3 and 4, and the line joining coordinates 1 and 2. To calculate the inclination along Y-axis (I_y), two points are selected (coordinates 5 and 6) along Y-axis on base 2. Then, the distance of these points from base 1 (l_1 and l_2) and the fixed distance between them (f_1) are calculated by measuring the coordinates using the EM system. Finally, the inclination angle can be estimated using the following equation:

$$I_y = tan^{-1}\frac{l_2 - l_1}{f_1} \tag{6.19}$$
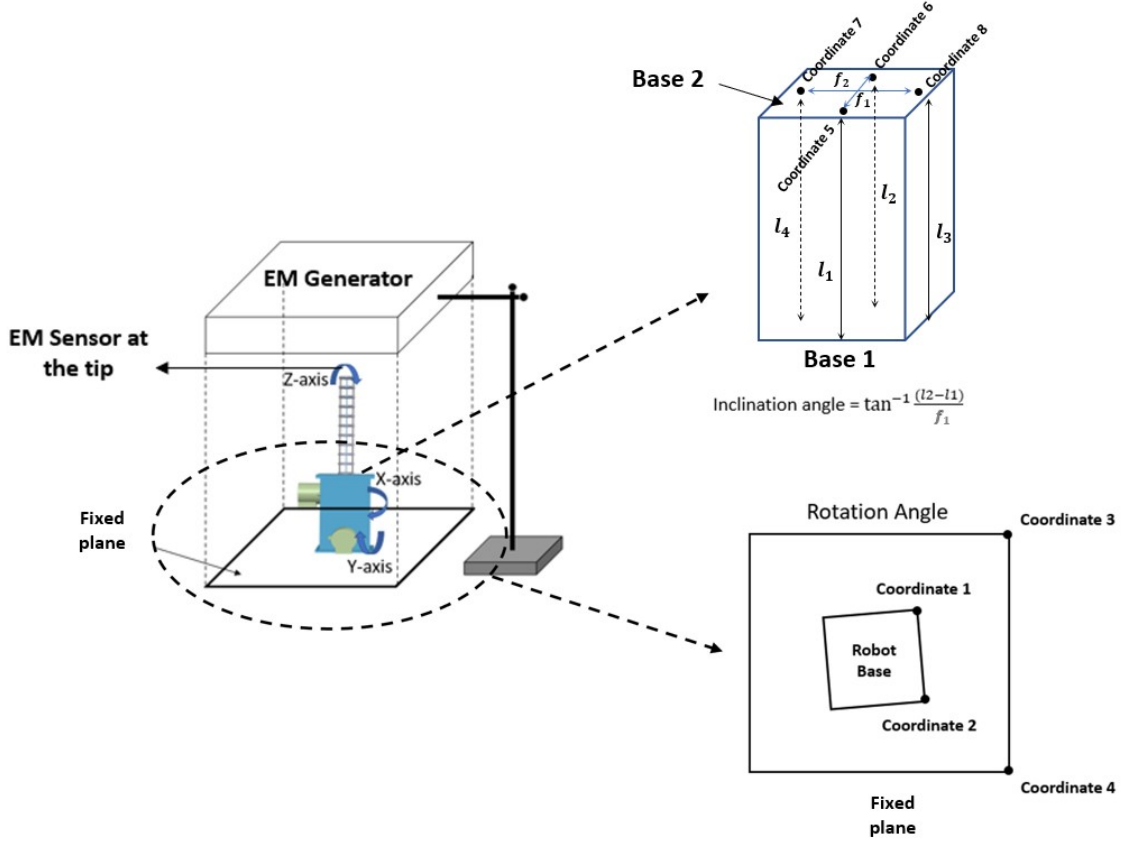
Figure 6.17: The EM sensing setup for tracking the robot's tip and ground truth generation

The same procedure is also followed to calculate the inclination along the x-axis. The procedure for calculating all these angles is shown in Figure 6.17. The rotation angle of the base is calculated as 0.5 degrees while the inclination angle of the x and y-axis is estimated as 0.3 and 0.4 degrees, respectively. These angles are used with a rotation matrix to find out the final tip coordinate which is given as follows:

$$
\begin{bmatrix} X_{Final} \\ Y_{Final} \\ Z_{Final} \end{bmatrix} = [Rotation_X] \cdot [Rotation_Y] \cdot [Rotation_Z] \begin{bmatrix} X_{EM} \\ Y_{EM} \\ Z_{EM} \end{bmatrix}
\tag{6.20}
$$

$$
\begin{bmatrix} X_{Final} \\ Y_{Final} \\ Z_{Final} \end{bmatrix} = \begin{bmatrix} 1 & 0 & 0 \\ 0 & -cos(I_y) & sin(I_x) \\ 0 & sin(I_x) & cos(I_y) \end{bmatrix} \begin{bmatrix} cos(I_y) & 0 & sin(I_y) \\ 0 & 1 & 0) \\ -sin(I_y) & 0 & cos(I_y) \end{bmatrix} \begin{bmatrix} cos(I_y) & -sin(I_x) & 0 \\ sin(I_x) & cos(I_y) & 0 \\ 0 & 0 & 1 \end{bmatrix}
$$

$$\tag{6.21}$$

The accuracy in the 3D shape reconstruction process is calculated by finding the distance between the reconstructed coordinates and acquired coordinates from the EM system. A mean distance error of 24.6 mm is estimated from this procedure. Since the angles are very small (Rotation = 0.5, inclination along x = 0.3, and inclination along y = 0.4 degrees), the effect on the error is very small. The shape sensing error without correction remains 24.7 mm while with correction is 24.6 mm. It can be noticed that the error in the 3D reconstruction is significantly more than the error in the 2D reconstruction process. The reason might be the issue related to the use of multiple sensors. One possible reason could be due to the effect of mutual inductance between the sensors which is not considered during the 3D reconstruction process. Another possible reason might be the use of constant curvature modeling. Since the modeling uses the strain information from 4 sensors, a small error in the strain estimation process of any sensor will greatly affect the 3D shape reconstruction process.

6.4 Conclusion

In this chapter, the use of the inductive sensor with a constant curvature model in the shape reconstruction process is discussed. Though the goal of this study is to provide a shape reconstruction method for soft and flexible robots, a tendon-driven flexible robot is considered here for the shape reconstruction validation since the robot poses similar mechanical properties and encounters the same problems as soft and flexible robots. In the beginning, the 2D shape reconstruction of the robot is performed and the accuracy is verified by comparing the shape with the visual-based shape estimation. This process is easy to implement and only requires a single sensor for estimating the planner shapes. To reconstruct the shape of the robot in a 3D workspace, four inductive sensors are used in a quadrangular manner. The length information from these four sensors is used to find the arc parameter of the robot that is further used to reconstruct the shape in 3D space. The accuracy in the 3D shape reconstruction process is estimated by comparing the coordinates of the tip from the reconstruction with an electromagnetic tracker placed at the tip of the robot. Both cases of shape reconstruction are important

based on the requirement. There are robots developed in the MIS context which are capable of approaching a target by combining in-plane bending and rotation of the base. Hence, the 2D shape reconstruction might be useful in this scenario. However, for complicated robots that don't involve base motors, the second method is useful. From the accuracy assessment, it is observed that the accuracy in the 2D shape reconstruction process remains adequate while a high reconstruction error is observed for the 3D shape reconstruction process. This is due to the use of multiple sensors. The reasons might be due to mutual inductance or the use of constant curvature modeling. All things considered, the inductive sensor has the capability to reconstruct the shape of soft and flexible robots employed in MIS. However, further study is required that will focus on the issue of the use of multiple sensors and the issue of the constant curvature model in order to increase the accuracy.

Chapter 7

Conclusion and Future Work

7.1 Overview

This thesis is about soft and flexible robots being used safely and accurately inside anatomy for MIS. Research is still ongoing on many aspects to develop such robots. A great effort has been put into making robots more flexible by altering the design and actuation strategies. In addition to this, the study of modeling and control of soft robots has been pursued for many years. A variety of control and modeling strategies ranging from kinematics to machine learning have been proposed. Still, controlling these soft and flexible robots safely inside the anatomy is an open problem. Their continuum structure gives them a high degree of flexibility and enables them to go to remote areas in the anatomy. However, they take on a variety of shapes or postures to get into the position. Consequently, sensing various properties of these robots is an active area of research. In particular, shape reconstruction is getting attention to deal with unexpected interaction and control more effectively their shape.

Various sensing techniques have been proposed to reconstruct the shape of the robots. The development of a general shape reconstruction method still remains an open challenge given that MIS deals with various soft and flexible robots as well as different medical circumstances. Apart from this, the flexibility of these robots limits the implementation of many shape reconstruction methods. These observations inspired us to investigate the shape reconstruction techniques already in use and to develop a technique for reconstructing the shape while addressing the issues of soft and flexible robots used in MIS.

7.2 Contribution

The study presented in this thesis has yielded important findings that help to answer the primary research problems posed by soft and flexible robots in the field of shape reconstruction. The state of the art revealed that the use of stretchable sensors in shape estimation is gaining attention due to the fulfillment of required criteria such as safety and large deformation encountered by the soft and flexible robots. However, these methods are still in the introductory phase and show high reconstruction error due to the involvement of high hysteresis. With the aim to reduce the hysteresis and non-linearities problems, the resistive sensors were studied in Chapter 3 starting from base material selection to the investigation of two manually and one industrially fabricated sensor. We could observe the sensitivity of these sensors towards the material's mechanical and electrical properties. Their adequacy was then examined and focus was made on the option of inductive sensing. Inductive-based stretchable sensors have low hysteresis, millimeter accuracy, and high stretchability as reported in the literature. For this purpose, a simple voltage measurement process across the conventional spring was presented. The feasibility and added value of proprioception were also verified for soft and flexible robots by performing the closed-loop control. Finally, the shape reconstruction process was performed in two steps with an increase in complexity. Here, a tendon-driven robot was considered for validating the shape reconstruction process since it has similar mechanical properties and encounters similar modeling behaviour such as non-constant curvature that soft and flexible robots face. In the first step, 2D shape reconstruction was performed in the tendon-driven robot which can also be applied to a class of robots that reach a target by combining in-plane bending and rotation of the base. A second study was performed for 3D shape estimation using multiple sensors which can be adapted in general.

The study in this thesis has led to understand the achievable performance of the inductive sensing method in various conditions. The characterization process showed that the sensor produces low hysteresis (mean hysteresis = 0.1%), high stretchability (more than 80% deformation), and high precision (mean deviation in the order of 0.14%) and

accuracy (mean error = 0.9%). The closed-loop control of the soft robot showed that the sensor is capable of controlling the robot with adequate accuracy while deforming more than 50% strains. When the sensor was used in the shape reconstruction process, the mean shape reconstruction error in the 2D process was 4.8 mm while the tip tracking error in the 3D workspace remained 24.6 mm. From this, it was observed that the accuracy during the characterization, control of the soft robot, and 2D shape reconstruction of the flexible robot remains adequate while the 3D reconstruction process shows a high reconstruction error. Unlike the other process where a single sensor was used, multiple sensors were used during the 3D shape reconstruction of the robot. Hence, the reason might be due to the effect of mutual inductance or the use of constant curvature modeling while using multiple sensors.

All in all, inductive sensor is a promising type of sensor for of shape reconstruction of soft and flexible robots considered in MIS due to their high stretchability and safety properties. Additionally, the proposed inductive sensor can be a suitable solution for other soft and flexible robots for measuring linear and bending strain. Despite many advantages, the study and application of proposed inductive sensors in various contexts show a few limitations. In terms of the use of multiple sensors, it shows difficulties in instrumentation and sensor calibration process that leads to an increase in shape reconstruction error. The integration of inductive sensors into more complex robots such as robots with multisegment or a robot with bending, elongation, and twisting elements might encounter difficulties due to the involvement of dozens of sensor cables. With regard to the use of a single sensor, the sensing and optimization methodology might not work if the coil loop condition is not maintained and a method to handle the evolution of geometry would need to be identified. In addition to this, the sensitivity of the sensor decreases drastically after 40% deformation which might reduce the effectiveness of the strain estimation after this deformation. This can be depicted from Figure 7.1

In this study, two sensors of different diameters (D=0.8 and 1.15 mm) with the same length have been verified experimentally. However, further reduction in the diameter and length of the sensor might lead to a decrease in gain and sensitivity thereby reducing
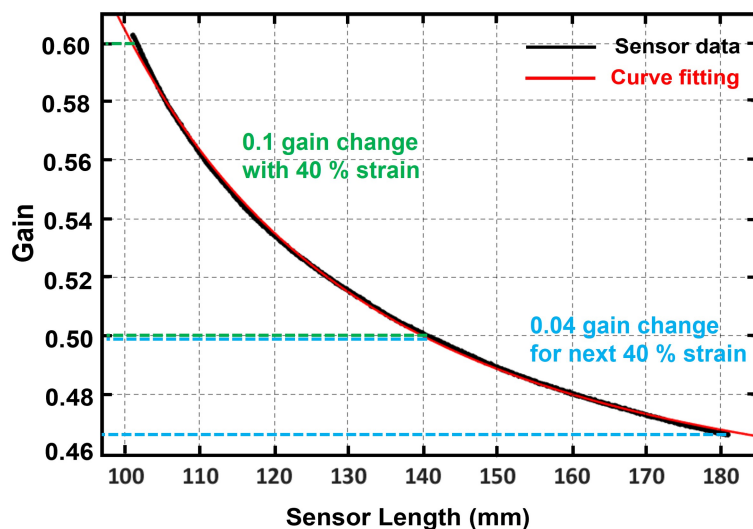
Figure 7.1: Reduction of sensitivity after 40 % deformation

the effectiveness of strain measurement and optimization process. Furthermore, it is very hard to differentiate between modes of deformation such as elongation, bending, or twisting with a single sensor when the system type is unknown.

7.3 Outlook for future works

The investigation of the inductive sensor in the current work has a wide range of potential extensions. However, we have listed a few things based on priority. Since we have seen that the use of multiple sensors shows high shape reconstruction error, the first level of priority of future work could be the continuation of the characterization process for multiple sensors configuration and the selection of a proper kinematic model of the robot. The characterization should focus on addressing the load issue of the inductive sensor on the equipment and the effect of mutual inductance on the sensing behavior. Since the effect of mutual inductance depends upon many factors, such as the geometry, total number, and the distance between the springs, an investigation to calculate the precise value of this phenomenon will be done. While selecting the kinematic model, it should focus on the problem of friction by using machine learning or other suitable methods.

The next level of priority could be the extension of the shape reconstruction method for multisegment robots. This work should concentrate on addressing the issue of handling multiple sensor cables. Since some of the multisegment robots reach targets by combining

bending, elongation, and twisting of their body parts, this work should also focus on the design of sets of inductive sensors for shape reconstruction considering the aforementioned modes of deformation.

The design of a mechatronics approach for the selection of the geometry such as diameter and length while addressing the issue of instrumentation and optimization during the miniaturization could be the next level of priority. The approach should also focus on the identification of a correction factor when the coil loop condition is not maintained. In this case, the coil loop condition is not maintained refers to the conversion of the helical coil to a straight wire.

The idea of hybrid shape reconstruction methods is an emerging research field nowadays to combine the advantages of each solution. Hence, the development of a hybrid method by fusing the inductive sensing technique with pose-optimized fluoroscopy or ultrasound imaging methods could be the next level of priority. This method can be a good compromise between safety and accuracy, and may be implemented in a broader environment where only the fluoroscopy system might not be feasible due to safety issues.

Since some flexible robots operate with a prestress, in addition to these priorities, future work may also focus on the exploitation of spring tension as a useful prestress during the design of such flexible robots. Springs can also be used as actuators in flexible robots. Therefore, the use of the same spring as a sensor and an actuator at the same time can be explored.

Last but not least on our priority list, future work should focus on tackling the issues related to the integration of inductive sensors into sterilizable medical devices, electrical safety, and robustness in various medical environments.

Bibliography

[1] TN Robinson and GV Stiegmann. "Minimally invasive surgery". In: *Endoscopy* 36.01 (2004), pp. 48–51.

[2] Valentina Vitiello et al. "Emerging Robotic Platforms for Minimally Invasive Surgery". In: *IEEE Reviews in Biomedical Engineering* 6 (2013), pp. 111–126. DOI: 10.1109/RBME.2012.2236311.

[3] Canberk Sozer et al. "Pressure-driven manipulator with variable stiffness structure". In: *2020 IEEE International Conference on Robotics and Automation (ICRA)*. IEEE. 2020, pp. 696–702.

[4] Izadyar Tamadon et al. "Novel robotic approach for minimally invasive aortic heart valve surgery". In: *2018 40th Annual International Conference of the IEEE Engineering in Medicine and Biology Society (EMBC)*. IEEE. 2018, pp. 3656–3659.

[5] Joshua B Gafford et al. "A concentric tube robot system for rigid bronchoscopy: a feasibility study on central airway obstruction removal". In: *Annals of biomedical engineering* 48.1 (2020), pp. 181–191.

[6] Cédric Girerd et al. "Towards optical biopsy of olfactory cells using concentric tube robots with follow-the-leader deployment". In: *2017 IEEE/RSJ International Conference on Intelligent Robots and Systems (IROS)*. IEEE. 2017, pp. 5661–5887.

[7] Michael DM Kutzer et al. "Design of a new cable-driven manipulator with a large open lumen: Preliminary applications in the minimally-invasive removal of osteolysis". In: *2011 IEEE International Conference on Robotics and Automation*. IEEE. 2011, pp. 2913–2920.

[8] Matteo Cianchetti et al. "Soft robotics technologies to address shortcomings in today's minimally invasive surgery: the STIFF-FLOP approach". In: *Soft robotics* 1.2 (2014), pp. 122–131.

[9] Iris De Falco, Matteo Cianchetti, and Arianna Menciassi. "A soft multi-module manipulator with variable stiffness for minimally invasive surgery". In: *Bioinspiration & biomimetics* 12.5 (2017), p. 056008.

[10] Tommaso Ranzani et al. "A bioinspired soft manipulator for minimally invasive surgery". In: *Bioinspiration & biomimetics* 10.3 (2015), p. 035008.

[11] Zhen Yun Shi, Da Liu, and Tian Miao Wang. "A shape memory alloy-actuated surgical instrument with compact volume". In: *The International Journal of Medical Robotics and Computer Assisted Surgery* 10.4 (2014), pp. 474–481.

[12] Alexander T Tung et al. "Laser-machined shape memory alloy actuators for active catheters". In: *IEEE/ASME transactions on mechatronics* 12.4 (2007), pp. 439–446.

[13] Muhammad Raihan Abdul Kadir et al. "A multi-segmented shape memory alloy-based actuator system for endoscopic applications". In: *Sensors and Actuators A: Physical* 296 (2019), pp. 92–100.

[14] M Taha Chikhaoui and Jessica Burgner-Kahrs. "Control of continuum robots for medical applications: State of the art". In: *ACTUATOR 2018; 16th International Conference on New Actuators*. VDE. 2018, pp. 1–11.

[15] Tamás Haidegger. "Autonomy for surgical robots: Concepts and paradigms". In: *IEEE Transactions on Medical Robotics and Bionics* 1.2 (2019), pp. 65–76.

[16] Chaoyang Shi et al. "Shape Sensing Techniques for Continuum Robots in Minimally Invasive Surgery: A Survey". In: *IEEE Transactions on Biomedical Engineering* 64.8 (2017), pp. 1665–1678. DOI: 10.1109/TBME.2016.2622361.

[17] Tomas da Veiga et al. "Challenges of continuum robots in clinical context: a review". In: *Progress in Biomedical Engineering* 2.3 (2020), p. 032003.

[18] Roy J Roesthuis, Momen Abayazid, and Sarthak Misra. "Mechanics-based model for predicting in-plane needle deflection with multiple bends". In: *2012 4th IEEE RAS & EMBS International Conference on Biomedical Robotics and Biomechatronics (BioRob)*. IEEE. 2012, pp. 69–74.

[19] Kai Xu and Nabil Simaan. "Analytic formulation for kinematics, statics, and shape restoration of multibackbone continuum robots via elliptic integrals". In: (2010).

[20] D Caleb Rucker et al. "Equilibrium conformations of concentric-tube continuum robots". In: *The International journal of robotics research* 29.10 (2010), pp. 1263–1280.

[21] D Caleb Rucker and Robert J Webster III. "Statics and dynamics of continuum robots with general tendon routing and external loading". In: *IEEE Transactions on Robotics* 27.6 (2011), pp. 1033–1044.

[22] Zheng Li et al. "Statics modeling of an underactuated wire-driven flexible robotic arm". In: *5th IEEE RAS/EMBS International Conference on Biomedical Robotics and Biomechatronics*. IEEE. 2014, pp. 326–331.

[23] Yan Bailly and Yacine Amirat. "Modeling and control of a hybrid continuum active catheter for aortic aneurysm treatment". In: *Proceedings of the 2005 IEEE International Conference on Robotics and Automation*. IEEE. 2005, pp. 924–929.

[24] Robert J Webster III and Bryan A Jones. "Design and kinematic modeling of constant curvature continuum robots: A review". In: *The International Journal of Robotics Research* 29.13 (2010), pp. 1661–1683.

[25] Bryan A Jones, Ricky L Gray, and Krishna Turlapati. "Three dimensional statics for continuum robotics". In: *2009 IEEE/RSJ International Conference on Intelligent Robots and Systems*. IEEE. 2009, pp. 2659–2664.

[26] Deepak Trivedi, Amir Lotfi, and Christopher D Rahn. "Geometrically exact models for soft robotic manipulators". In: *IEEE Transactions on Robotics* 24.4 (2008), pp. 773–780.

[27] Ryan J Murphy et al. "Design and kinematic characterization of a surgical manipulator with a focus on treating osteolysis". In: *Robotica* 32.6 (2014), pp. 835–850.

[28] Thien-Dang Nguyen and Jessica Burgner-Kahrs. "A tendon-driven continuum robot with extensible sections". In: *2015 IEEE/RSJ International Conference on Intelligent Robots and Systems (IROS)*. IEEE. 2015, pp. 2130–2135.

[29] Michael Waine et al. "3D shape visualization of curved needles in tissue from 2D ultrasound images using RANSAC". In: *2015 IEEE International Conference on Robotics and Automation (ICRA)*. 2015, pp. 4723–4728. DOI: `10.1109/ICRA.2015.7139855`.

[30] Hongliang Ren, Nikolay V. Vasilyev, and Pierre E. Dupont. "Detection of curved robots using 3D ultrasound". In: *2011 IEEE/RSJ International Conference on Intelligent Robots and Systems*. 2011, pp. 2083–2089. DOI: `10.1109/IROS.2011.6094915`.

[31] Izadyar Tamadon et al. "ValveTech: A Novel Robotic Approach for Minimally Invasive Aortic Valve Replacement". In: *IEEE Transactions on Biomedical Engineering* 68.4 (2021), pp. 1238–1249. DOI: `10.1109/TBME.2020.3024184`.

[32] Gastone Ciuti et al. "Frontiers of robotic colonoscopy: a comprehensive review of robotic colonoscopes and technologies". In: *Journal of clinical medicine* 9.6 (2020), p. 1648.

[33] Joonhwan Kim et al. "Advancement of Flexible Robot Technologies for Endoluminal Surgeries". In: *Proceedings of the IEEE* 110.7 (2022), pp. 909–931. DOI: `10.1109/JPROC.2022.3170109`.

[34] Hongliang Ren and Pierre E Dupont. "Tubular enhanced geodesic active contours for continuum robot detection using 3d ultrasound". In: *2012 IEEE International Conference on Robotics and Automation*. IEEE. 2012, pp. 2907–2912.

[35] Matthias Hoffmann et al. "Semi-automatic catheter reconstruction from two views". In: *International Conference on Medical Image Computing and Computer-Assisted Intervention*. Springer. 2012, pp. 584–591.

[36] Shirley AM Baert et al. "Three-dimensional guide-wire reconstruction from biplane image sequences for integrated display in 3-D vasculature". In: *IEEE transactions on medical imaging* 22.10 (2003), pp. 1252–1258.

[37] Marcel Schenderlein et al. "Catheter tracking in asynchronous biplane fluoroscopy images by 3D B-snakes". In: *Medical Imaging 2010: Visualization, Image-Guided Procedures, and Modeling*. Vol. 7625. SPIE. 2010, pp. 578–586.

[38] Sylvie Menet. "B-snakes: Implementation and application to stereo". In: *Proceedings of Third International Conference on Computer Vision, 1990*. 1990.

[39] Matthias Hoffmann et al. "Reconstruction method for curvilinear structures from two views". In: *Medical Imaging 2013: Image-Guided Procedures, Robotic Interventions, and Modeling*. Vol. 8671. SPIE. 2013, pp. 630–637.

[40] Matthias Hoffmann et al. "Electrophysiology catheter detection and reconstruction from two views in fluoroscopic images". In: *IEEE transactions on medical imaging* 35.2 (2015), pp. 567–579.

[41] Alessandro Vandini et al. "Unified tracking and shape estimation for concentric tube robots". In: *IEEE Transactions on Robotics* 33.4 (2017), pp. 901–915.

[42] Chrysi Papalazarou, Peter MJ Rongen, et al. "3D catheter reconstruction using non-rigid structure-from-motion and robotics modeling". In: *Medical Imaging 2012: Image-Guided Procedures, Robotic Interventions, and Modeling*. Vol. 8316. SPIE. 2012, pp. 622–629.

[43] Yoshito Otake et al. "Piecewise-rigid 2D-3D registration for pose estimation of snake-like manipulator using an intraoperative x-ray projection". In: *Medical Imaging 2014: Image-Guided Procedures, Robotic Interventions, and Modeling*. Vol. 9036. International Society for Optics and Photonics. 2014, 90360Q.

[44] Alessandro Vandini et al. "Vision-based intraoperative shape sensing of concentric tube robots". In: *2015 IEEE/RSJ International Conference on Intelligent Robots and Systems (IROS)*. IEEE. 2015, pp. 2603–2610.

[45] David J Brenner and J Eric. "Hall." Computed tomography—an increasing source of radiation exposure."". In: *New England Journal of Medicine* 357.22 (2007), pp. 2277–2284.

[46] Edgar J Lobaton et al. "Continuous shape estimation of continuum robots using X-ray images". In: *2013 IEEE international conference on robotics and automation*. IEEE. 2013, pp. 725–732.

[47] Raffaella Trivisonne, Erwan Kerrien, and Stéphane Cotin. "Constrained stochastic state estimation of deformable 1D objects: Application to single-view 3D reconstruction of catheters with radio-opaque markers". In: *Computerized Medical Imaging and Graphics* 81 (2020), p. 101702.

[48] Stephanie Cheung and Robert Rohling. "Enhancement of needle visibility in ultrasound-guided percutaneous procedures". In: *Ultrasound in medicine & biology* 30.5 (2004), pp. 617–624.

[49] Paul M Novotny et al. "GPU based real-time instrument tracking with three-dimensional ultrasound". In: *Medical image analysis* 11.5 (2007), pp. 458–464.

[50] Paul M Novotny et al. "Gpu based real-time instrument tracking with three dimensional ultrasound". In: *International Conference on Medical Image Computing and Computer-Assisted Intervention*. Springer. 2006, pp. 58–65.

[51] Marián Uherčík et al. "Model fitting using RANSAC for surgical tool localization in 3-D ultrasound images". In: *IEEE Transactions on Biomedical Engineering* 57.8 (2010), pp. 1907–1916.

[52] Zhouping Wei et al. "Oblique needle segmentation for 3D TRUS-guided robot-aided transperineal prostate brachytherapy". In: *2004 2nd IEEE International Symposium on Biomedical Imaging: Nano to Macro (IEEE Cat No. 04EX821)*. IEEE. 2004, pp. 960–963.

[53] Yue Zhao, Hervé Liebgott, and Christian Cachard. "Tracking micro tool in a dynamic 3D ultrasound situation using Kalman filter and RANSAC algorithm". In: *2012 9th IEEE International Symposium on Biomedical Imaging (ISBI)*. IEEE. 2012, pp. 1076–1079.

[54] Joseph D Greer et al. "Real-time 3D curved needle segmentation using combined B-mode and power Doppler ultrasound". In: *International Conference on Medical Image Computing and Computer-Assisted Intervention*. Springer. 2014, pp. 381–388.

[55]   Jay Carriere et al. "Real-time needle shape prediction in soft-tissue based on image segmentation and particle filtering". In: *2016 IEEE International Conference on Advanced Intelligent Mechatronics (AIM)*. IEEE. 2016, pp. 1204–1209.

[56]   Michael Waine et al. "3d shape visualization of curved needles in tissue from 2d ultrasound images using ransac". In: *2015 IEEE International Conference on Robotics and Automation (ICRA)*. IEEE. 2015, pp. 4723–4728.

[57]   Hamid Reza Sadeghi Neshat and Rajni V Patel. "Real-time parametric curved needle segmentation in 3D ultrasound images". In: *2008 2nd IEEE RAS & EMBS International Conference on Biomedical Robotics and Biomechatronics*. IEEE. 2008, pp. 670–675.

[58]   Hongliang Ren and Pierre E Dupont. "Tubular structure enhancement for surgical instrument detection in 3D ultrasound". In: *2011 Annual international conference of the ieee engineering in medicine and biology society*. IEEE. 2011, pp. 7203–7206.

[59]   Luca Sestini et al. "A Kinematic Bottleneck Approach For Pose Regression of Flexible Surgical Instruments directly from Images". In: *IEEE Robotics and Automation Letters* 6.2 (2021), pp. 2938–2945.

[60]   Rob Reilink, Stefano Stramigioli, and Sarthak Misra. "Three-dimensional pose reconstruction of flexible instruments from endoscopic images". In: *2011 IEEE/RSJ International Conference on Intelligent Robots and Systems*. IEEE. 2011, pp. 2076–2082.

[61]   Rob Reilink, Stefano Stramigioli, and Sarthak Misra. "Pose reconstruction of flexible instruments from endoscopic images using markers". In: *2012 IEEE International Conference on Robotics and Automation*. IEEE. 2012, pp. 2938–2943.

[62]   Paolo Cabras et al. "Comparison of methods for estimating the position of actuated instruments in flexible endoscopic surgery". In: *2014 IEEE/RSJ International Conference on Intelligent Robots and Systems*. IEEE. 2014, pp. 3522–3528.

[63]   Kemal Fidanboylu and HS Efendioglu. "Fiber optic sensors and their applications". In: *5th International Advanced Technologies Symposium (IATS'09)*. Vol. 6. 2009, pp. 2–3.

[64]   David A Krohn, Trevor MacDougall, and Alexis Mendez. *Fiber optic sensors: fundamentals and applications*. Spie Press Bellingham, WA, 2014.

[65]   Eric Udd. "An overview of fiber-optic sensors". In: *review of scientific instruments* 66.8 (1995), pp. 4015–4030.

[66]   José Luıs Santos and Faramarz Farahi. *Handbook of optical sensors*. Crc Press, 2014.

[67]   Mohd Anwar Zawawi, Sinead O'Keffe, and Elfed Lewis. "Intensity-modulated fiber optic sensor for health monitoring applications: a comparative review". In: *Sensor Review* (2013).

[68]   Huichan Zhao et al. "A Helping Hand". In: *IEEE ROBOTICS & AUTOMATION MAGAZINE* (2016).

[69]   Thomas C Searle et al. "An optical curvature sensor for flexible manipulators". In: *2013 IEEE International Conference on Robotics and Automation.* IEEE. 2013, pp. 4415–4420.

[70]   Sina Sareh et al. "Macrobend optical sensing for pose measurement in soft robot arms". In: *Smart Materials and Structures* 24.12 (2015), p. 125024.

[71]   Celeste To, Tess Lee Hellebrekers, and Yong-Lae Park. "Highly stretchable optical sensors for pressure, strain, and curvature measurement". In: *2015 IEEE/RSJ international conference on intelligent robots and systems (IROS).* IEEE. 2015, pp. 5898–5903.

[72]   Byeong Ha Lee et al. "Interferometric fiber optic sensors". In: *sensors* 12.3 (2012), pp. 2467–2486.

[73]   Paulo Roriz et al. "Fiber optic intensity-modulated sensors: A review in biomechanics". In: *Photonic Sensors* 2.4 (2012), pp. 315–330.

[74]   Xue Zhou et al. "A vectorial analysis of the curvature sensor based on a dual-core photonic crystal fiber". In: *IEEE Transactions on Instrumentation and Measurement* 69.9 (2020), pp. 6564–6570.

[75]   Raffaella Di Sante. "Fibre optic sensors for structural health monitoring of aircraft composite structures: Recent advances and applications". In: *Sensors* 15.8 (2015), pp. 18666–18713.

[76]   Yi Bao et al. "Review of fiber optic sensors for structural fire engineering". In: *Sensors* 19.4 (2019), p. 877.

[77]   Kevin C Galloway et al. "Fiber optic shape sensing for soft robotics". In: *Soft robotics* 6.5 (2019), pp. 671–684.

[78]   Frantisek Urban et al. "Design of a pressure sensor based on optical fiber Bragg grating lateral deformation". In: *Sensors* 10.12 (2010), pp. 11212–11225.

[79]   Kenneth O Hill et al. "Photosensitivity in optical fiber waveguides: Application to reflection filter fabrication". In: *Applied physics letters* 32.10 (1978), pp. 647–649.

[80]   Gerald Meltz, William W Morey, and William H Glenn. "Formation of Bragg gratings in optical fibers by a transverse holographic method". In: *Optics letters* 14.15 (1989), pp. 823–825.

[81]   Kenneth O Hill et al. "Bragg gratings fabricated in monomode photosensitive optical fiber by UV exposure through a phase mask". In: *Applied Physics Letters* 62.10 (1993), pp. 1035–1037.

[82]   Ams Martinez et al. "Direct writing of fibre Bragg gratings by femtosecond laser". In: *Electronics letters* 40.19 (2004), pp. 1170–1172.

[83]   Xue-Feng Huang et al. "Design and characteristics of refractive index sensor based on thinned and microstructure fiber Bragg grating". In: *Applied Optics* 47.4 (2008), pp. 504–511.

[84]   Ricardo Oliveira, Lúcia Bilro, and Rogério Nogueira. "Strain Sensitivity Control of an In-Series Silica and Polymer FBG". In: *Sensors* 18.6 (2018), p. 1884.

[85]   HJ Patrick et al. "Hybrid fiber Bragg grating/long period fiber grating sensor for strain/temperature discrimination". In: *IEEE Photonics Technology Letters* 8.9 (1996), pp. 1223–1225.

[86]   Y Mizutani and RM Groves. "Multi-functional measurement using a single FBG sensor". In: *Experimental mechanics* 51.9 (2011), pp. 1489–1498.

[87]   Yuheng Pan et al. "Simultaneous measurement of temperature and strain using spheroidal-cavity-overlapped FBG". In: *IEEE Photonics Journal* 7.6 (2015), pp. 1–6.

[88]   Hirotaka Igawa et al. "Distributed measurements with a long gauge FBG sensor using optical frequency domain reflectometry (1st report, system investigation using optical simulation model)". In: *Journal of Solid Mechanics and Materials Engineering* 2.9 (2008), pp. 1242–1252.

[89]   George T Kanellos et al. "Two dimensional polymer-embedded quasi-distributed FBG pressure sensor for biomedical applications". In: *Optics express* 18.1 (2010), pp. 179–186.

[90]   Marcelo M Werneck et al. "A guide to fiber Bragg grating sensors". In: *Current trends in short-and long-period fiber gratings* (2013), pp. 1–24.

[91]   Ian D Walker. "Continuous backbone "continuum" robot manipulators". In: *International Scholarly Research Notices* 2013 (2013).

[92]   Sonja Jäckle et al. "Fiber optical shape sensing of flexible instruments for endovascular navigation". In: *International journal of computer assisted radiology and surgery* 14.12 (2019), pp. 2137–2145.

[93]   Junbo Wei et al. "Novel integrated helical design of single optic fiber for shape sensing of flexible robot". In: *IEEE Sensors Journal* 17.20 (2017), pp. 6627–6636.

[94]   Roy J Roesthuis, Sander Janssen, and Sarthak Misra. "On using an array of fiber Bragg grating sensors for closed-loop control of flexible minimally invasive surgical instruments". In: *2013 IEEE/Rsj International Conference on Intelligent Robots and Systems*. IEEE. 2013, pp. 2545–2551.

[95]   Hao Liu et al. "Large deflection shape sensing of a continuum manipulator for minimally-invasive surgery". In: *2015 IEEE International Conference on Robotics and Automation (ICRA)*. IEEE. 2015, pp. 201–206.

[96]   Hao Liu et al. "Shape tracking of a dexterous continuum manipulator utilizing two large deflection shape sensors". In: *IEEE sensors journal* 15.10 (2015), pp. 5494–5503.

[97]   Shahriar Sefati et al. "FBG-based position estimation of highly deformable continuum manipulators: Model-dependent vs. data-driven approaches". In: *2019 International Symposium on Medical Robotics (ISMR)*. IEEE. 2019, pp. 1–6.

[98]   Ran Xu, Aaron Yurkewich, and Rajni V Patel. "Curvature, torsion, and force sensing in continuum robots using helically wrapped FBG sensors". In: *IEEE Robotics and Automation Letters* 1.2 (2016), pp. 1052–1059.

[99]   Hesheng Wang et al. "Shape detection algorithm for soft manipulator based on fiber bragg gratings". In: *IEEE/ASME Transactions on Mechatronics* 21.6 (2016), pp. 2977–2982.

[100]   Yanlin He et al. "Design, measurement and shape reconstruction of soft surgical actuator based on fiber Bragg gratings". In: *Applied Sciences* 8.10 (2018), p. 1773.

[101]   Yanlin He et al. "Optical Fiber Sensor Performance Evaluation in Soft Polyimide Film with Different Thickness Ratios". In: *Sensors* 19.4 (2019), p. 790.

[102] Massimo Leonardo Filograno et al. "Real-time monitoring of railway traffic using fiber Bragg grating sensors". In: *IEEE Sensors Journal* 12.1 (2011), pp. 85–92.

[103] Xiaomei Wang et al. "Eye-in-hand visual servoing enhanced with sparse strain measurement for soft continuum robots". In: *IEEE Robotics and Automation Letters* 5.2 (2020), pp. 2161–2168.

[104] Fouzia Khan et al. "Multi-core optical fibers with Bragg gratings as shape sensor for flexible medical instruments". In: *IEEE sensors journal* 19.14 (2019), pp. 5878–5884.

[105] Chaoyang Shi et al. "Simultaneous catheter and environment modeling for transcatheter aortic valve implantation". In: *2014 IEEE/RSJ International Conference on Intelligent Robots and Systems*. IEEE. 2014, pp. 2024–2029.

[106] Yong-Lae Park et al. "Real-time estimation of 3-D needle shape and deflection for MRI-guided interventions". In: *IEEE/ASME Transactions On Mechatronics* 15.6 (2010), pp. 906–915.

[107] Roy J Roesthuis et al. "Three-dimensional needle shape reconstruction using an array of fiber bragg grating sensors". In: *IEEE/ASME transactions on mechatronics* 19.4 (2013), pp. 1115–1126.

[108] Xinhua Yi et al. "An innovative 3D colonoscope shape sensing sensor based on FBG sensor array". In: *2007 International Conference on Information Acquisition*. IEEE. 2007, pp. 227–232.

[109] Shahriar Sefati et al. "A highly sensitive fiber Bragg Grating shape sensor for continuum manipulators with large deflections". In: *2017 IEEE SENSORS*. IEEE. 2017, pp. 1–3.

[110] Shahriar Sefati et al. "FBG-based large deflection shape sensing of a continuum manipulator: Manufacturing optimization". In: *2016 IEEE SENSORS*. IEEE. 2016, pp. 1–3.

[111] Shahriar Sefati et al. "FBG-based control of a continuum manipulator interacting with obstacles". In: *2018 IEEE/RSJ International Conference on Intelligent Robots and Systems (IROS)*. IEEE. 2018, pp. 6477–6483.

[112] Shahriar Sefati et al. "Data-driven shape sensing of a surgical continuum manipulator using an uncalibrated fiber bragg grating sensor". In: *IEEE Sensors Journal* 21.3 (2020), pp. 3066–3076.

[113] Roy J Roesthuis and Sarthak Misra. "Steering of multisegment continuum manipulators using rigid-link modeling and FBG-based shape sensing". In: *IEEE transactions on robotics* 32.2 (2016), pp. 372–382.

[114] Qiulin Hou, Changhou Lu, and Xueyong Li. "A novel pose sensing model for soft manipulator based on helical FBG". In: *Sensors and Actuators A: Physical* 321 (2021), p. 112586.

[115] Xiang-Yan Chen et al. "Fabrication and shape detection of a catheter using fiber Bragg grating". In: *Advances in Manufacturing* 8.1 (2020), pp. 107–118.

[116] Fei Qi et al. "Shape sensing and feedback control of the catheter robot for interventional surgery". In: *Industrial Robot: the international journal of robotics research and application* (2020).

[117] Omar Al-Ahmad et al. "Improved fbg-based shape sensing methods for vascular catheterization treatment". In: *IEEE Robotics and Automation Letters* 5.3 (2020), pp. 4687–4694.

[118] Jin Seob Kim et al. "Shape determination during needle insertion with curvature measurements". In: *2017 IEEE/RSJ International Conference on Intelligent Robots and Systems (IROS)*. IEEE. 2017, pp. 201–208.

[119] Jin Seob Kim et al. "Fiber Bragg Grating based needle shape sensing for needle steering system: Evaluation in inhomogeneous tissue". In: *2017 IEEE SENSORS*. IEEE. 2017, pp. 1–3.

[120] Seok Chang Ryu and Pierre E Dupont. "FBG-based shape sensing tubes for continuum robots". In: *2014 IEEE International Conference on Robotics and Automation (ICRA)*. IEEE. 2014, pp. 3531–3537.

[121] Zhang Lunwei et al. "FBG sensor devices for spatial shape detection of intelligent colonoscope". In: *IEEE International Conference on Robotics and Automation, 2004. Proceedings. ICRA'04. 2004*. Vol. 1. IEEE. 2004, pp. 834–840.

[122] Alfred M Franz et al. "Electromagnetic tracking in medicine—a review of technology, validation, and applications". In: *IEEE transactions on medical imaging* 33.8 (2014), pp. 1702–1725.

[123] Guofang Xiao et al. "Electromagnetic tracking in image-guided laparoscopic surgery: Comparison with optical tracking and feasibility study of a combined laparoscope and laparoscopic ultrasound system". In: *Medical physics* 45.11 (2018), pp. 5094–5104.

[124] Kevin Cleary et al. "Electromagnetic tracking for image-guided abdominal procedures: Overall system and technical issues". In: *2005 IEEE Engineering in Medicine and Biology 27th Annual Conference*. IEEE. 2006, pp. 6748–6753.

[125] Cristian A Linte et al. "Accuracy considerations in image-guided cardiac interventions: experience and lessons learned". In: *International journal of computer assisted radiology and surgery* 7.1 (2012), pp. 13–25.

[126] Christoph Alexander Aufdenblatten and Stefan Altermatt. "Intraventricular catheter placement by electromagnetic navigation safely applied in a paediatric major head injury patient". In: *Child's Nervous System* 24.9 (2008), pp. 1047–1050.

[127] Steven Leong et al. "Electromagnetic navigation bronchoscopy: A descriptive analysis". In: *Journal of thoracic disease* 4.2 (2012), p. 173.

[128] Marvin P Fried et al. "Image-guided endoscopic surgery: results of accuracy and performance in a multicenter clinical study using an electromagnetic tracking system". In: *The Laryngoscope* 107.5 (1997), pp. 594–601.

[129] David R Lionberger et al. "How does electromagnetic navigation stack up against infrared navigation in minimally invasive total knee arthroplasties?" In: *The Journal of arthroplasty* 23.4 (2008), pp. 573–580.

[130] Stephen Tully et al. "Shape estimation for image-guided surgery with a highly articulated snake robot". In: *2011 IEEE/RSJ International Conference on Intelligent Robots and Systems*. IEEE. 2011, pp. 1353–1358.

[131] Stephen Tully and Howie Choset. "A filtering approach for image-guided surgery with a highly articulated surgical snake robot". In: *IEEE Transactions on Biomedical Engineering* 63.2 (2015), pp. 392–402.

[132] Alessio Dore et al. "Catheter navigation based on probabilistic fusion of electromagnetic tracking and physically-based simulation". In: *2012 IEEE/RSJ International Conference on Intelligent Robots and Systems*. IEEE. 2012, pp. 3806–3811.

[133] Hwan-Taek Ryu et al. "Shape and contact force estimation of inserted flexible medical device". In: *International Journal of Control, Automation and Systems* 18.1 (2020), pp. 163–174.

[134] Shuang Song et al. "Electromagnetic positioning for tip tracking and shape sensing of flexible robots". In: *IEEE Sensors Journal* 15.8 (2015), pp. 4565–4575.

[135] Shuang Song et al. "Real-time shape estimation for wire-driven flexible robots with multiple bending sections based on quadratic Bézier curves". In: *IEEE Sensors Journal* 15.11 (2015), pp. 6326–6334.

[136] Liao Wu et al. "Development of a compact continuum tubular robotic system for nasopharyngeal biopsy". In: *Medical & biological engineering & computing* 55.3 (2017), pp. 403–417.

[137] Xin Ma, Philip Wai-Yan Chiu, and Zheng Li. "Real-time deformation sensing for flexible manipulators with bending and twisting". In: *IEEE Sensors Journal* 18.15 (2018), pp. 6412–6422.

[138] Mahdi Azizian and Rajni Patel. "Data fusion for catheter tracking using Kalman filtering: applications in robot-assisted catheter insertion". In: *Medical Imaging 2011: Visualization, Image-Guided Procedures, and Modeling*. Vol. 7964. SPIE. 2011, pp. 327–337.

[139] Phuong Toan Tran et al. "3D catheter shape reconstruction using electromagnetic and image sensors". In: *Journal of Medical Robotics Research* 2.03 (2017), p. 1740009.

[140] Phuong Toan Tran et al. "Towards 3D catheter shape reconstruction using electromagnetic and image sensors". In: *Proceedings of the 5th Joint Workshop on New Technologies for Computer/Robot Assisted Surgery*. 2015, pp. 62–65.

[141] Jie Wang et al. "Pilot study on shape sensing for continuum tubular robot with multi-magnet tracking algorithm". In: *2017 IEEE International Conference on Robotics and Biomimetics (ROBIO)*. IEEE. 2017, pp. 1165–1170.

[142] Hao Guo et al. "Continuum robot shape estimation using permanent magnets and magnetic sensors". In: *Sensors and Actuators A: Physical* 285 (2019), pp. 519–530.

[143] Changchun Zhang et al. "Shape tracking and navigation for continuum surgical robot based on magnetic tracking". In: *2017 IEEE International Conference on Information and Automation (ICIA)*. IEEE. 2017, pp. 1143–1149.

[144] Tobias Reichl, José Gardiazabal, and Nassir Navab. "Electromagnetic servoing—A new tracking paradigm". In: *IEEE transactions on medical imaging* 32.8 (2013), pp. 1526–1535.

[145] Jinho So et al. "Shape estimation of soft manipulator using stretchable sensor". In: *Cyborg and Bionic Systems* 2021 (2021).

[146] Matteo Cianchetti et al. "Sensorization of continuum soft robots for reconstructing their spatial configuration". In: *2012 4th IEEE RAS & EMBS International Conference on Biomedical Robotics and Biomechatronics (BioRob)*. IEEE. 2012, pp. 634–639.

[147] Federico Renda and Cecilia Laschi. "A general mechanical model for tendon-driven continuum manipulators". In: *2012 IEEE International Conference on Robotics and Automation*. IEEE. 2012, pp. 3813–3818.

[148] Helge A Wurdemann et al. "Embedded electro-conductive yarn for shape sensing of soft robotic manipulators". In: *2015 37th Annual International Conference of the IEEE Engineering in Medicine and Biology Society (EMBC)*. IEEE. 2015, pp. 8026–8029.

[149] Ali Abbas and Jianguo Zhao. "Twisted and coiled sensor for shape estimation of soft robots". In: *2017 IEEE/RSJ International Conference on Intelligent Robots and Systems (IROS)*. IEEE. 2017, pp. 482–487.

[150] Xiaoyong Wei et al. "Development of a variable-stiffness and shape-detection manipulator based on low-melting-point-alloy for minimally invasive surgery". In: *2020 42nd Annual International Conference of the IEEE Engineering in Medicine & Biology Society (EMBC)*. IEEE. 2020, pp. 4895–4898.

[151] R Adam Bilodeau et al. "Design for control of a soft bidirectional bending actuator". In: *2018 IEEE/RSJ International Conference on Intelligent Robots and Systems (IROS)*. IEEE. 2018, pp. 1–8.

[152] Jiyun Jeon and Chunwoo Kim. "Shape Sensor Using Magnetic Induction with Frequency Sweeping for Medical Catheters". In: *2021 IEEE International Conference on Robotics and Automation (ICRA)*. 2021, pp. 7137–7143. DOI: `10.1109/ICRA48506.2021.9561072`.

[153] Tae Kyung Kim, Jeong Koo Kim, and Ok Chan Jeong. "Measurement of nonlinear mechanical properties of PDMS elastomer". In: *Microelectronic Engineering* 88.8 (2011). Proceedings of the 36th International Conference on Micro- and Nano-Engineering (MNE), pp. 1982–1985. ISSN: 0167-9317. DOI: `https://doi.org/10.1016/j.mee.2010.12.108`. URL: `https://www.sciencedirect.com/science/article/pii/S0167931710005964`.

[154] Jorgen S Bergström and MC1056 Boyce. "Constitutive modeling of the large strain time-dependent behavior of elastomers". In: *Journal of the Mechanics and Physics of Solids* 46.5 (1998), pp. 931–954.

[155] Zisheng Liao, Mokarram Hossain, and Xiaohu Yao. "Ecoflex polymer of different Shore hardnesses: Experimental investigations and constitutive modelling". In: *Mechanics of Materials* 144 (2020), p. 103366. ISSN: 0167-6636. DOI: `https://doi.org/10.1016/j.mechmat.2020.103366`. URL: `https://www.sciencedirect.com/science/article/pii/S016766362030020X`.

[156] Prakash Karipoth et al. "Graphite-Based Bioinspired Piezoresistive Soft Strain Sensors with Performance Optimized for Low Strain Values". In: *ACS Applied Materials & Interfaces* 13.51 (2021). PMID: 34910475, pp. 61610–61619. DOI: `10.1021/acsami.1c14228`. eprint: `https://doi.org/10.1021/acsami.1c14228`. URL: `https://doi.org/10.1021/acsami.1c14228`.

[157] Anindya Nag et al. "Strain induced graphite/PDMS sensors for biomedical applications". In: *Sensors and Actuators A: Physical* 271 (2018), pp. 257–269.

[158] Saloumeh Moshfegh and Nadereh Golshan Ebrahimi. "Strain sensors based on graphite fillers". In: *Iranian Polymer Journal* 13.2 (2004), pp. 113–119.

[159] Yi Sun, Yun Seong Song, and Jamie Paik. "Characterization of silicone rubber based soft pneumatic actuators". In: *2013 IEEE/RSJ International Conference on Intelligent Robots and Systems*. 2013, pp. 4446–4453. DOI: `10.1109/IROS.2013.6696995`.

[160] Sattar Din et al. "A Stretchable Multimodal Sensor for Soft Robotic Applications". In: *IEEE Sensors Journal* 17.17 (2017), pp. 5678–5686. DOI: `10.1109/JSEN.2017.2726099`.

[161] Eric Luis et al. "Silicone 3D Printing: Process Optimization, Product Biocompatibility, and Reliability of Silicone Meniscus Implants". In: *3D Printing and Additive Manufacturing* 6.6 (2019), pp. 319–332. DOI: `10.1089/3dp.2018.0226`. eprint: `https://doi.org/10.1089/3dp.2018.0226`. URL: `https://doi.org/10.1089/3dp.2018.0226`.

[162] Le Cai et al. "Super-stretchable, transparent carbon nanotube-based capacitive strain sensors for human motion detection". In: *Scientific reports* 3.1 (2013), pp. 1–9.

[163] Shangjie Zhang et al. "Highly stretchable, sensitive, and flexible strain sensors based on silver nanoparticles/carbon nanotubes composites". In: *Journal of Alloys and compounds* 652 (2015), pp. 48–54.

[164] Shota Hamaguchi et al. "Soft Inductive Tactile Sensor Using Flow-Channel Enclosing Liquid Metal". In: *IEEE Robotics and Automation Letters* 5.3 (2020), pp. 4028–4034. DOI: `10.1109/LRA.2020.2985573`.

[165] Aby Raj P.M., Thileepan Stalin, and Pablo Valdivia y Alvarado. "Flexible Fiber Inductive Coils for Soft Robots and Wearable Devices". In: *IEEE Robotics and Automation Letters* 7.2 (2022), pp. 5711–5718. DOI: `10.1109/LRA.2022.3159864`.

[166] A Fassler and C Majidi. "Soft-matter capacitors and inductors for hyperelastic strain sensing and stretchable electronics". In: *Smart Materials and Structures* 22.5 (2013), p. 055023.

[167] Wyatt Felt, Khai Yi Chin, and C. David Remy. "Contraction Sensing With Smart Braid McKibben Muscles". In: *IEEE/ASME Transactions on Mechatronics* 21.3 (2016), pp. 1201–1209. DOI: `10.1109/TMECH.2015.2493782`.

[168] Wyatt Felt et al. "An inductance-based sensing system for bellows-driven continuum joints in soft robots". In: *Autonomous robots* 43.2 (2019), pp. 435–448.

[169] Zhiguang Xing et al. "Inductive Strain Sensor With High Repeatability and Ultra-Low Hysteresis Based on Mechanical Spring". In: *IEEE Sensors Journal* 20.24 (2020), pp. 14670–14675. DOI: `10.1109/JSEN.2020.3010345`.

[170] Osamu Azami et al. "Development of the extension type pneumatic soft actuator with built-in displacement sensor". In: *Sensors and Actuators A: Physical* 300 (2019), p. 111623.

[171] A. V. Prituja, Hritwick Banerjee, and Hongliang Ren. "Electromagnetically Enhanced Soft and Flexible Bend Sensor: A Quantitative Analysis With Different Cores". In: *IEEE Sensors Journal* 18.9 (2018), pp. 3580–3589. DOI: 10.1109/JSEN.2018.2817211.

[172] Kyungjun Choi et al. "Soft Inductive Coil Spring Strain Sensor Integrated with SMA Spring Bundle Actuator". In: *Sensors* 21.7 (2021), p. 2304.

[173] Q. Yu and T.W. Holmes. "Stray capacitance modeling of inductors by using the finite element method". In: *1999 IEEE International Symposium on Electromagnetic Compatability. Symposium Record (Cat. No.99CH36261)*. Vol. 1. 1999, 305–310 vol.1. DOI: 10.1109/ISEMC.1999.812918.

[174] A. Massarini and M.K. Kazimierczuk. "Self-capacitance of inductors". In: *IEEE Transactions on Power Electronics* 12.4 (1997), pp. 671–676. DOI: 10.1109/63.602562.

[175] Xintian Tang et al. "Coiled Conductive Polymer Fiber Used in Soft Manipulator as Sensor". In: *IEEE Sensors Journal* 18.15 (2018), pp. 6123–6129. DOI: 10.1109/JSEN.2018.2846553.

[176] M. Cianchetti et al. "Sensorization of continuum soft robots for reconstructing their spatial configuration". In: *2012 4th IEEE RAS EMBS International Conference on Biomedical Robotics and Biomechatronics (BioRob)*. 2012, pp. 634–639. DOI: 10.1109/BioRob.2012.6290788.

[177] Taigo Yukisawa et al. "Modeling of extensible pneumatic actuator with bellows (EPAB) for continuum arm". In: *2017 IEEE International Conference on Robotics and Biomimetics (ROBIO)*. 2017, pp. 2303–2308. DOI: 10.1109/ROBIO.2017.8324762.

[178] Junbo Wei et al. "Novel Integrated Helical Design of Single Optic Fiber for Shape Sensing of Flexible Robot". In: *IEEE Sensors Journal* 17.20 (2017), pp. 6627–6636. DOI: 10.1109/JSEN.2017.2748162.

[179] Yan-Bing Bai et al. "Polyline approach for approximating Hausdorff distance between planar free-form curves". In: *Computer-Aided Design* 43.6 (2011), pp. 687–698.

[180] Qi Zhang et al. "Enabling Autonomous Colonoscopy Intervention Using a Robotic Endoscope Platform". In: *IEEE Transactions on Biomedical Engineering* 68.6 (2021), pp. 1957–1968. DOI: 10.1109/TBME.2020.3043388.

[181] Guru Subramani and Michael R. Zinn. "Tackling friction - an analytical modeling approach to understanding friction in single tendon driven continuum manipulators". In: *2015 IEEE International Conference on Robotics and Automation (ICRA)*. 2015, pp. 610–617. DOI: 10.1109/ICRA.2015.7139242.

[182] Jinwoo Jung et al. "A modeling approach for continuum robotic manipulators: Effects of nonlinear internal device friction". In: *2011 IEEE/RSJ International Conference on Intelligent Robots and Systems*. 2011, pp. 5139–5146. DOI: 10.1109/IROS.2011.6094941.

[183] Antonio De Donno et al. "Introducing STRAS: A new flexible robotic system for minimally invasive surgery". In: *2013 IEEE International Conference on Robotics and Automation*. 2013, pp. 1213–1220. DOI: 10.1109/ICRA.2013.6630726.

Sujit Kumar SAHU

Capteurs inductifs et reconstruction de forme pour les robots médicaux souples et flexibles

École doctorale

Mathématiques, sciences de l'information et de l'**ingénieur** | ED 269

Université de Strasbourg

Université de Strasbourg

Résumé

Insérer votre résumé en français suivi des mots-clés

Les robots souples et flexibles transforment les interventions médicales, grâce à leur flexibilité, leur miniaturisation et leurs capacités de mouvement multidirectionnel. Cependant, les méthodes de reconstruction de forme existantes n'ont pas suffisamment pris en compte les défis posés par les robots souples et flexibles dans les environnements non structurés et dynamiques. Dans cette thèse, un capteur extensible basé sur le principe inductif électrique est proposé comme solution à ce problème. Le capteur peut détecter de grandes déformations avec une grande précision et une grande précision et est intégré dans un robot souple et flexible pour un contrôle en boucle fermée. La thèse se concentre sur la reconstruction de la forme du robot dans des scénarios de chirurgie mini-invasive dans les espaces de travail 2D et 3D. Enfin, la thèse conclut en présentant le potentiel du capteur inductif pour la reconstruction de la forme de robots souples et flexibles et les travaux futurs pour surmonter les limitations.

Mots clés :
Capteur de forme flexible, capteur inductif, détection en mode mini-invasif Chirurgie, reconstruction de forme

Résumé en anglais

Insérer votre résumé en anglais suivi des mots-clés

Soft and flexible robots are transforming medical interventions, thanks to their flexibility, miniaturization, and multidirectional movement abilities. However, existing shape reconstruction methods have not adequately addressed the challenges posed by these robots in unstructured and dynamic environments. In this thesis, a stretchable sensor based on the electrical inductive principle is proposed as a solution to this problem. The thesis presents a simple voltage measurement method for strain estimation, which optimizes the measuring equipment and simplifies the measurement conditions. The sensor's feasibility and accuracy are demonstrated in an experimental investigation that shows the sensor can detect large deformations with high precision and accuracy. The sensor is then integrated into a soft and flexible robot for closed-loop control, and the thesis focuses on reconstructing the robot's shape in minimally invasive surgery scenarios in both 2D and 3D workspaces. Finally, the thesis concludes with an overview of the inductive sensor's potential for shape reconstruction of soft and flexible robots and future work to address the limitations.

Keywords :

Flexible shape sensor, Inductive sensor, Sensing in Minimally Invasive Surgery, Shape reconstruction